Weber, M., Abu-Ayyash, K., Abueladas, A., Agnon, A., Alasonati Tasárová, Z., Al-Zubi, H., Babeyko, A., Bartov, Y., Bauer, K., Becken, M., Bedrosia, P. A., Ben-Avraham, Z., Bock, G., Bohnhoff, M., Bribach, J., Dulski, P., Ebbing, J., El-Kelani, R., Förster, A., Förster, H.-J., Frieslander, U., Garfunkel, Z., Goetze, H. J., Haak, V., Haberland, C., Hassouneh, M., Helwig, S., Hofstetter, A., Hoffmann-Rothe, A., Jäckel, K. H., Janssen, C., Jaser, D., Kesten, D., Khatib, M., Kind, R., Koch, O., Koulakov, I., Laske, G., Maercklin, N., Masarweh, R., Masri, A., Matar, A., Mechie, J., Meqbel, N., Plessen, B., Möller, P., Mohsen, A., Oberhänsli, R., Oreshin, S., Petrunin, A., Qabbani, I., Rabba, I., Ritter, O., Romer, R. L., Rümpker, G., Rybakov, M., Ryberg, T., Saul, J., Scherbaum, F., Schmidt, S., Schulze, A., Sobolev, S. V., Stiller, M., Stromeyer, D., Tarawneh, K., Trela, C., Weckmann, U., Wetzel, U., Wylegalla, K. (2009): Anatomy of the Dead Sea transform from lithospheric to microscopic scale. - Reviews of Geophysics, 47, RG2002, 10.1029/2008RG000264.

ANATOMY OF THE DEAD SEA TRANSFORM FROM LITHOSPHERIC TO MICROSCOPIC SCALE

M. Weber,[1,2] K. Abu-Ayyash,[3] A. Abueladas,[3] A. Agnon,[4] Z. Alasonati-Tašárová,[5] H. Al-Zubi,[3] A. Babeyko,[1] Y. Bartov,[6] K. Bauer,[1] M. Becken,[1] P. A. Bedrosian,[7] Z. Ben-Avraham,[8] G. Bock,[1] M. Bohnhoff,[1] J. Bribach,[1] P. Dulski,[1] J. Ebbing,[9] R. El-Kelani,[10] A. Förster,[1] H.-J. Förster,[2] U. Frieslander,[11] Z. Garfunkel,[4] H. J. Goetze,[5] V. Haak,[1] C. Haberland,[1] M. Hassouneh,[12] S. Helwig,[13] A. Hofstetter,[11] A. Hoffmann-Rothe,[14] K. H. Jäckel,[1] C. Janssen,[1] D. Jaser,[3] D. Kesten,[15] M. Khatib,[16] R. Kind,[1] O. Koch,[13] I. Koulakov,[1,17] G. Laske,[18] N. Maercklin,[19] R. Masarweh,[3] A. Masri,[3] A. Matar,[16] J. Mechie,[1] N. Meqbel,[1] B. Plessen,[1] P. Möller,[1] A. Mohsen,[1] R. Oberhänsli,[2] S. Oreshin,[20] A. Petrunin,[1] I. Qabbani,[3] I. Rabba,[3] O. Ritter,[1] R. L. Romer,[1] G. Rümpker,[21] M. Rybakov,[11] T. Ryberg,[1] J. Saul,[1] F. Scherbaum,[2] S. Schmidt,[5] A. Schulze,[1] S. V. Sobolev,[1,20] M. Stiller,[1] D. Stromeyer,[1] K. Tarawneh,[22] C. Trela,[23] U. Weckmann,[1] U. Wetzel,[1] and K. Wylegalla[1]

Received 12 February 2008; revised 12 August 2008; accepted 24 October 2008; published XX Month 2009.

[1] Fault zones are the locations where motion of tectonic plates, often associated with earthquakes, is accommodated. Despite a rapid increase in the understanding of faults in the last decades, our knowledge of their geometry, petrophysical properties, and controlling processes remains incomplete. The central questions addressed here in our study of the Dead Sea Transform (DST) in the Middle East are as follows: (1) What are the structure and kinematics of a large fault zone? (2) What controls its structure and kinematics? (3) How does the DST compare to other plate boundary fault zones? The DST has accommodated a total of 105 km of left-lateral transform motion between the African and Arabian plates since early Miocene (~20 Ma). The DST segment between the Dead Sea and the Red Sea, called the Arava/Araba Fault (AF), is studied here using a multidisciplinary and multiscale approach from the μm to the plate tectonic scale. We observe that under the DST a narrow, subvertical zone cuts through crust and lithosphere. First, from west to east the crustal thickness increases smoothly from 26 to 39 km, and a subhorizontal lower crustal reflector is detected east of the AF. Second, several faults exist in the upper crust in a 40 km wide zone centered on the AF, but none have kilometer-size zones of decreased seismic velocities or zones of high electrical conductivities in the upper crust expected for large damage zones. Third, the AF is the main branch of the DST system, even though it has accommodated only a part (up to 60 km) of the overall 105 km of sinistral plate motion. Fourth, the AF acts as a barrier to fluids to a depth of 4 km, and the lithology changes abruptly across it. Fifth, in the top few hundred meters of the AF a locally transpressional regime is observed in a 100–300 m wide zone of deformed and displaced material, bordered by subparallel faults forming a positive flower structure. Other segments of the AF have a

[1]GeoForschungsZentrum, Potsdam, Germany.
[2]Department of Geosciences, University of Potsdam, Potsdam, Germany.
[3]Natural Resources Authority, Amman, Jordan.
[4]Institute of Earth Sciences, Hebrew University, Jerusalem, Israel.
[5]Institute for Geosciences, University of Kiel, Kiel, Germany.
[6]National Ministry of Infrastructure, Jerusalem, Israel.
[7]U.S. Geological Survey, Denver, Colorado, USA.
[8]Department of Geophysics and Planetary Sciences, Tel Aviv University, Tel Aviv, Israel.
[9]Geological Survey of Norway, Trondheim, Norway.
[10]Earth Sciences and Seismic Engineering Center, An-Najah National University, Nablus, Palestine.
[11]Geophysical Institute of Israel, Lod, Israel.
[12]Ministry of Presidential Affairs, Abu Dhabi, United Arab Emirates.
[13]Institute of Geophysics and Meteorology, University of Cologne, Cologne, Germany.
[14]Bundesanstalt für Geowissenschaften und Rohstoffe, Geozentrum Hannover, Hannover, Germany.
[15]Landesamt für Geologie, Rohstoffe und Bergbau, Freiburg, Germany.
[16]Geology Department, University of Aleppo, Aleppo, Syria.
[17]Institute of Geology, SB, RAS, Novosibirsk, Russia.
[18]Scripps Institution of Oceanography, University of California, San Diego, La Jolla, California, USA.
[19]Istituto Nazionale di Geofisica e Vulcanologia, Catania, Italy.
[20]Institute of Earth Physics, Moscow, Russia.
[21]Institute of Geoscience, Goethe-Universität, Frankfurt, Germany.
[22]Faculty of Mining and Environment Engineering, Al-Hussein Bin Talal University, Amman, Jordan.
[23]Bundesanstalt für Materialforschung und -prüfung, Berlin, Germany.

8755-1209/09/2008RG000264$15.00
Paper number 2008RG000264
XXXXXX

transtensional character with small pull-aparts along them. The damage zones of the individual faults are only 5–20 m wide at this depth range. Sixth, two areas on the AF show mesoscale to microscale faulting and veining in limestone sequences with faulting depths between 2 and 5 km. Seventh, fluids in the AF are carried downward into the fault zone. Only a minor fraction of fluids is derived from ascending hydrothermal fluids. However, we found that on the kilometer scale the AF does not act as an important fluid conduit. Most of these findings are corroborated using thermomechanical modeling where shear deformation in the upper crust is localized in one or two major faults; at larger depth, shear deformation occurs in a 20–40 km wide zone with a mechanically weak decoupling zone extending subvertically through the entire lithosphere.

Citation: Weber, M., et al. (2009), Anatomy of the Dead Sea Transform from lithospheric to microscopic scale, *Rev. Geophys.*, *47*, XXXXXX, doi:10.1029/2008RG000264.

1. INTRODUCTION

[2] Large faults are the most prominent surface expressions of crustal and lithospheric processes driven by motions within the interior of the Earth. Key sites to study large strike-slip faults include the San Andreas Fault (SAF) in California, USA; the Alpine Fault in New Zealand; the North Anatolian Fault (NAF) in Turkey; and the Dead Sea Transform (DST) in the Middle East (Figure 1). These and other fault zones constitute some of the most visible expressions of plate tectonics and can be traced at the surface for hundreds of kilometers. Active faults are also the locations of large earthquakes responsible for the risk associated with seismic hazard. In recent years it became widely accepted that transform faults represent pathways for the movement of fluids, especially water/brines, and sites of enrichments in minerals. Despite their social and economic relevance and much progress in their understanding in the last decades, one of the most challenging problems and still one of the key questions of plate tectonics remains: to understand in more detail the initiation and the spatial and temporal evolution of active large fault zones.

[3] Recently, several authors have addressed this question summarizing the present state of knowledge. One focus has been the internal structure of crustal fault zones and the mechanism of faulting at different depth ranges [*Chester et al.*, 1993; *Holdsworth et al.*, 2001; *Ben-Zion and Sammis*, 2003; *Faulkner et al.*, 2003]. Other studies have used geophysical methods [e.g., *Ritter et al.*, 2005a] to show similarities and differences between geophysical images of fault zones. The most recent and comprehensive review, including an exhaustive list of recent references, is given by *Handy et al.* [2007] and, from a geophysical perspective, by *Mooney et al.* [2007]. One of their key recommendations and challenges for the future is to study fault zones in a multidisciplinary approach focused on natural laboratories and looking at interacting processes within faults. Because of the wide range of parameters and forces controlling the shape and kinematics of faults the comparison of the results derived at several natural laboratories is an absolute necessity to gain a better insight into these processes. In that context, *Mooney et al.* [2007] list several outstanding key questions concerning faults, for example, (1) How far down into the crust do fault damage zones extend? (2) Does crustal deformation become narrower or wider in the lower crust? (3) Is there a physical relationship between pronounced seismic low-velocity zones and high-conductivity zones?

[4] Here we address some of the key questions and give an overview of our multidisciplinary investigation (Figure 2) that aimed to quantify the physical processes responsible for forming the Arava/Araba Fault (AF) segment of the DST. This is done by combining findings from seismology, electromagnetics, gravity, geothermics, petrology, geochemistry, field mapping based mainly on surface geology as well as satellite image interpretation and remote sensing, and thermomechanical numerical simulations. The spatial scales analyzed range from 10 + 5 to 10 − 5 m with the goal of understanding the evolution of the DST through time. These findings are compared to results known from the most intensively studied fault worldwide, the SAF. For details, see *Li et al.* [1990], *Brocher et al.* [1994], *Holbrook et al.* [1996], *Henstock et al.* [1997], *Unsworth et al.* [1997, 2000], *Ryberg and Fuis* [1998], *Fuis et al.* [2001], *Hole et al.* [2001], and *Becken et al.* [2008]. The most recent overviews are given by *Mooney et al.* [2007], *Wilson et al.* [2005], and *Fuis et al.* [2008], who compared the transpressional plate boundaries of the SAF and the Alpine Fault in New Zealand, and by *Jiracek et al.* [2008], who studied the SAF, the Alpine Fault, and the Yarlung-Tsangpo Suture in southern Tibet.

[5] In section 2 we summarize the results of our multidisciplinary geophysical approach to imaging and mapping the AF, from lithospheric to crustal scale, then from the kilometer to meter scale, and finally down to the μm scale. These results, summarized in Figure 3, are then compared to petrological and geochemical studies together with findings from surface geology and thermomechanical modeling. In section 3 we compare our results for the AF with those from specific locations of the SAF, finding some similarities but also significant differences. Section 4 contains the discussion and conclusions and an outlook on future challenges.

2. DEAD SEA TRANSFORM

[6] The DST is a ~1000 km long left-lateral fault zone that extends from the Red Sea spreading center to the Zagros zone of plate convergence (Figure 1). It cuts through a continental area whose crust was shaped by the end-Proterozoic Pan-African Orogeny. Later, from Cambrian to Paleogene times, it behaved as a stable platform and was covered by extensive sediment cover. The platformal history was interrupted by a period of faulting and magmatism

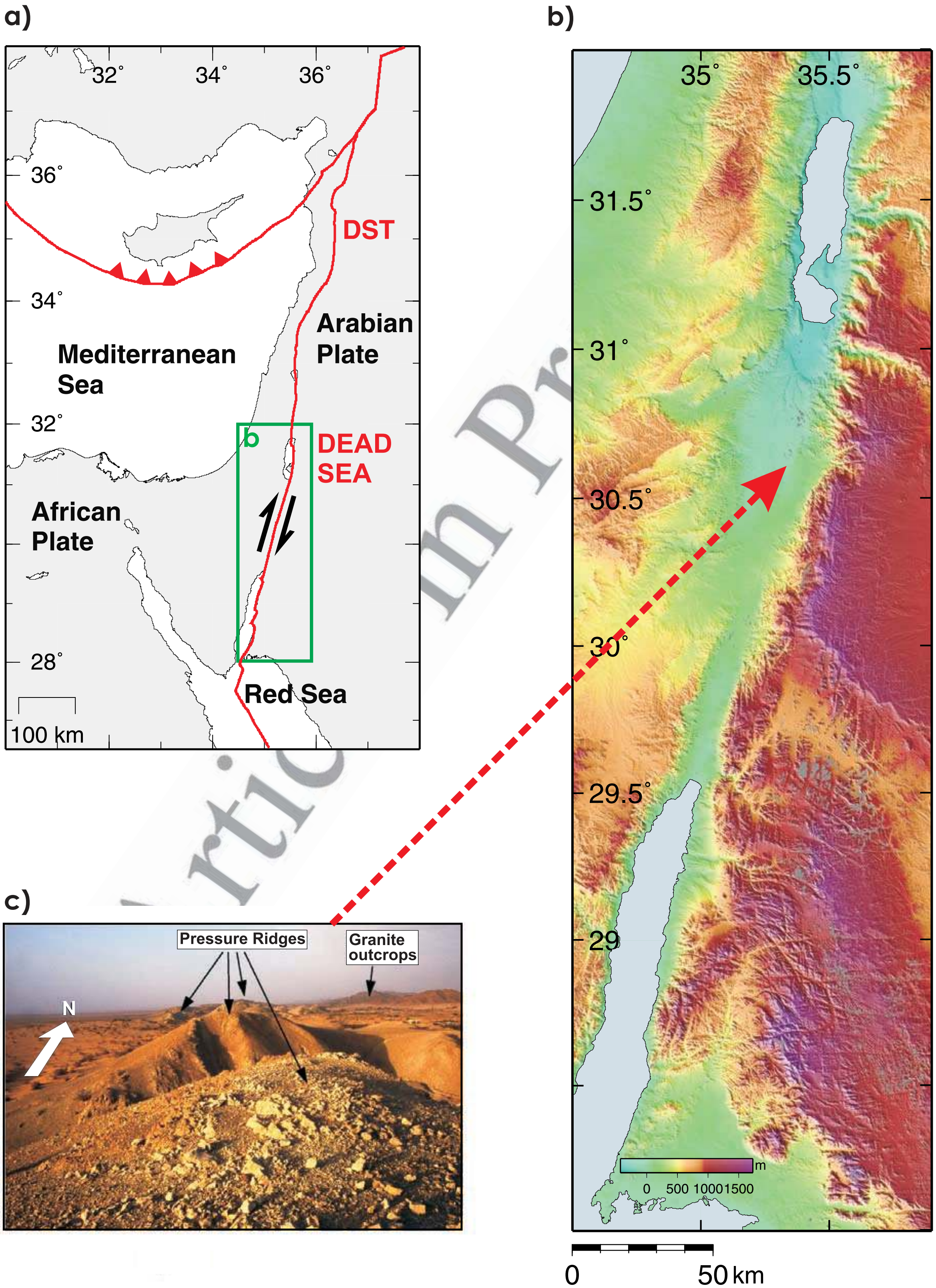

Figure 1. (a) Tectonic setting of the Levant. DST, Dead Sea Transform. (b) Relief map of the region between the Dead Sea and the Red Sea (green box in Figure 1a). (c) Pressure ridges in the Arava/Araba Valley between lines P9 and P10 in Figure 2f and at line 5 in Figure 2g.

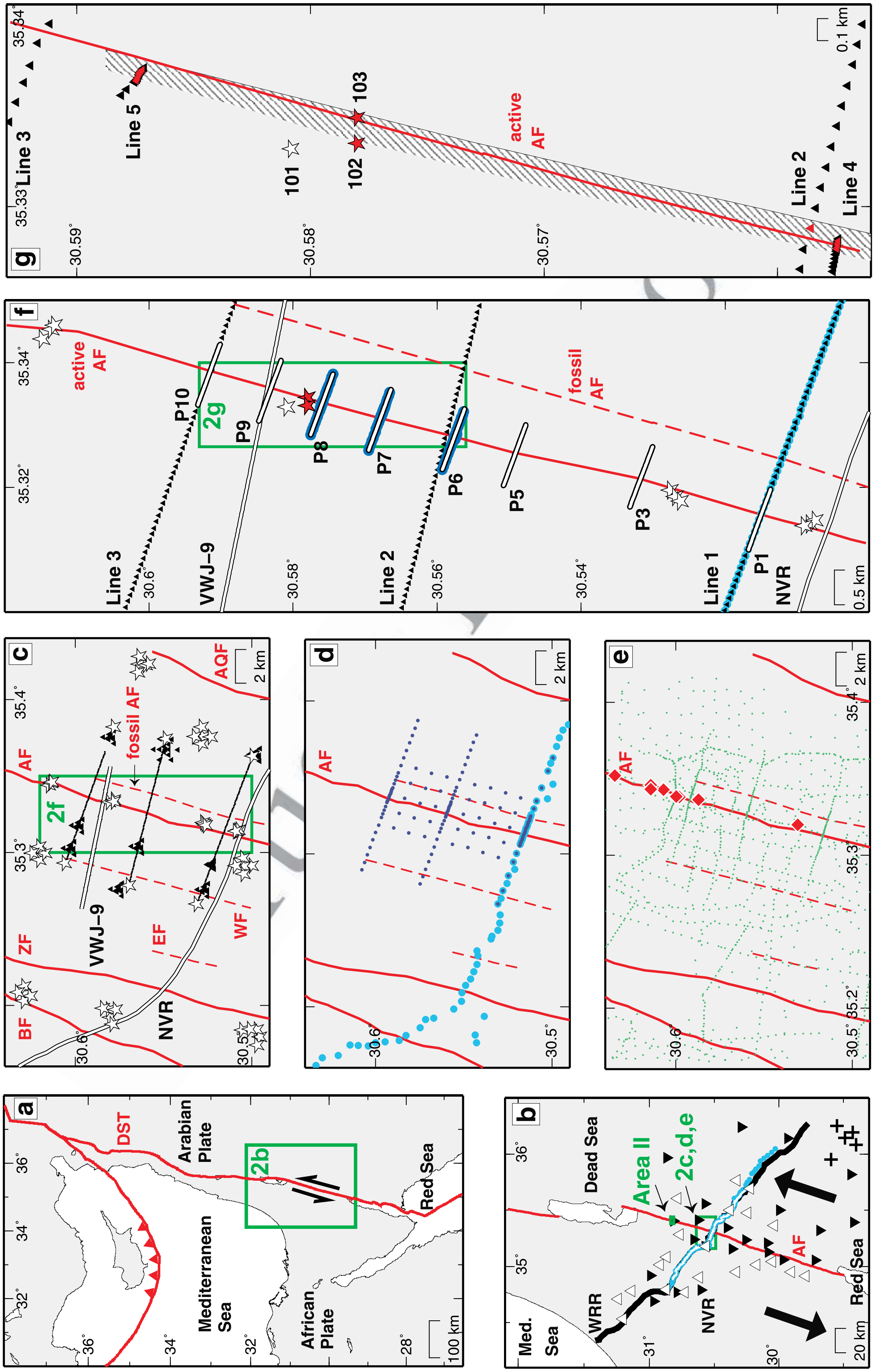
a
DST
Arabian Plate
2b
Mediterranean Sea
African Plate
Red Sea
100 km
b
Dead Sea
Area II
2c,d,e
Med. Sea
WRR
NVR
AF
Red Sea
20 km
c
AF
fossil AF
2f
ZF
BF
VWJ–9
EF
WF
NVR
AQF
2 km
d
AF
2 km
e
AF
2 km
f
active AF
fossil AF
2g
Line 3
VWJ–9
Line 2
Line 1
NVR
P1
P3
P5
P6
P7
P8
P9
P10
0.5 km
g
Line 3
Line 5
101
102
103
active AF
Line 2
Line 4
0.1 km

Figure 2

related to shaping the Levant continental margin in the early Mesozoic, by intraplate magmatism in the Early Cretaceous, and by mild folding and shearing in Late Cretaceous to Miocene times [*Garfunkel*, 1988, and references therein]. The DST is one of the new plate boundaries that formed when this continental area broke up in mid-Cenozoic times [*Freund*, 1965; *Gass*, 1970; *Garfunkel*, 1981; *Bosworth et al.*, 2005, and references therein].

[7] The ∼600 km long part of the DST south of Lebanon has a broad arcuate shape in map view and is mostly marked by a conspicuous valley, while its more northern part is less regular. Our study deals with the southern segment, focusing on an area that was little affected by previous Phanerozoic deformation. Matching of the rock bodies and structures across the transform along this segment indicates a left lateral offset of ∼105 km (uncertainty is a couple of kilometers) and that the motion postdated ∼20 Ma old dikes [*Quennell*, 1958; *Freund et al.*, 1970; *Bartov*, 1974; *Bandel and Khouri*, 1981; *Eyal et al.*, 1981]. Regional plate kinematics give an independent similar estimate of the offset, ∼100 km (uncertainty < 20 km), and also show that much of the offset occurred already in Miocene times [*Joffe and Garfunkel*, 1987; *Garfunkel and Beyth*, 2006]. The structure along the southern half of the DST [*Garfunkel*, 1981; *Garfunkel and Ben-Avraham*, 2001; *Ben-Avraham et al.*, 2008] is dominated by longitudinal strike-slip faults arranged en echelon that produce a series of deep pull-apart basins (also called rhomb grabens) alternating with much shallower fault-controlled structural saddles. These structures are embedded in a 3–20 km wide depressed zone that forms a valley delimited on both sides by normal faults so that the southern segment of DST superficially resembles extensional rifts. These faults displace very young sediments and have a direct physiographic expression, indicating their continuing activity [*Garfunkel et al.*, 1981]. The strike slip faults trend at a small angle to the overall elongation of this part of the DST, which indicates a small component of transtension that is augmented by the longitudinal normal faults. In addition, near our transect and farther south a part of the lateral motion took place on several faults crossing the margins of the topographic valley [*Eyal et al.*, 1981; *Sneh et al.*, 1998], but farther north it was concentrated in the topographic valley. The development of the DST was accompanied by uplifting of the flanking regions. Also, igneous activity took place in a wide region, mainly east of it and along its northern half, but it was very limited near our transect [*Garfunkel*, 1989; *Sneh et al.*, 1998].

[8] Since the advent of plate tectonics the DST has been considered a prime site to examine large shear zones [*Quennell*, 1958; *Wilson*, 1965; *Freund et al.*, 1970]. Large historical earthquakes on the DST with magnitudes up to 7 [*Garfunkel et al.*, 1981; *Ambraseys et al.*, 1994; *Amiran et al.*, 1994; *Klinger et al.*, 2000b; *Ken-Tor et al.*, 2001; *Migowski et al.*, 2004; *Agnon et al.*, 2006] and the recent 1995 Nueiba *M*7.2 event [*Hofstetter et al.*, 2003] as well as

Figure 2. Setting of the DST and location of experiments within the Dead Sea Rift Transect (DESERT) project. Known faults are indicated in red. The area of subsequent blow-ups is indicated by a labeled green box. Note different scales. (a) Main faults of the Levant [see, e.g., *Garfunkel*, 1981; *Ben-Avraham*, 1985]. The left lateral displacement of 105 km at the DST is indicated by black arrows. The area of Figure 2b is given by the labeled green box. (b) The red lines indicate the main branches of the DST. Seismic/seismological experiments (transect) in black and white: black line, 260 km long wide-angle reflection/refraction (WRR) profile (13 shots and 99 receivers); white line, 100 km long near-vertical reflection (NVR) profile (roll along vibroseis source spacing 50 m, receiver spacing 100 m, and 90-fold coverage), coinciding with the inner part of the WRR. Passive long-term deployment (1.5 years) of seismological stations (21 short-period (open triangles) and 27 broadband stations (full triangles)). Electromagnetic/magnetotelluric (MT) experiments in blue: MT-long, light blue dots, 140 km long, coinciding mostly with NVR. Sites of thermal borehole measurements and surface heat flow determination are given by black crosses. The area of Figures 2c–2e is given by the labeled green box. Area II of the microstructural analysis (Figure 22, top right) is also indicated in green. (c) Central Arava/Araba Valley in Israel/Jordan. The red lines indicate the dominant active faults in the area (BF, Barak Fault; ZF, Zofar Fault; AF, Arava/Araba Fault; AQF, Al Quwayra Fault). The dashed red lines indicate the surface traces of three buried, now inactive faults (Eastern Fault (EF), Western Fault (WF), and fossil AF). Seismic experiments (for details, see section 2): NVR and VWJ-9, white lines; controlled source arrays (CSA) I, thin black lines, 3 × 10 km long; and CSA I miniarrays, black triangles, 9 station arrays (10 seismometers each). White stars indicate CSA I shot locations (7 × 5 shots, 4 × 3 shots on/near the AF, and 3 × 2 shots at end of the three CSA I lines). (d) As Figure 2c but for MT. MT regional profile, large, light blue dots; MT-pilot, dark blue dots, 10 km profile in the vicinity of the AF in the center of the MT regional profile; MT 3-D experiment, small, blue dots, 2 × 10 km and 7 × 4 km profiles. (e) As Figure 2c but for the local gravity survey. Green dots indicate the gravity sites. Locations of mesostructural and microstructural analysis on the AF (area I, Figure 22 (top left)) are given as red diamonds. (f) The red line shows the active AF, and the dashed red line indicates the surface trace of the buried fossil AF. Seismic experiments in black and white: NVR and VWJ-9, white lines; CSA I, black triangles, part of 3 × 10 km long lines (lines 1–3, station spacing 100 m). White stars indicate CSA I shot locations on/near the AF. Red stars indicate shots that produced fault zone guided waves (FZGW). CSA II, short white profiles, 8 × 1 km (P1–P10; station spacing 5 m on each line and shot spacing of 20 m). Electromagnetic experiments in blue: Long Offset Transient Electromagnetics, blue line, 8 km long along line 1 of CSA I (only partially shown); Short Offset Transient Electromagnetics, blue lines, 3 × 1 km long and coinciding with profiles P6, P7, and P8 from CSA II. (g) FZGW experiment on the active AF. Black triangles are stations of CSA I (lines 2 and 3, spacing 100 m (see Figure 2c); lines 4 and 5, spacing 10 m, with 20 stations per line). Stars indicate shot locations (shots 101–103). Red stars and triangles indicate shots and stations that produced or recorded FZGW, respectively. The shallow low-velocity segment of the active AF identified by FZGW is given by the shaded area.

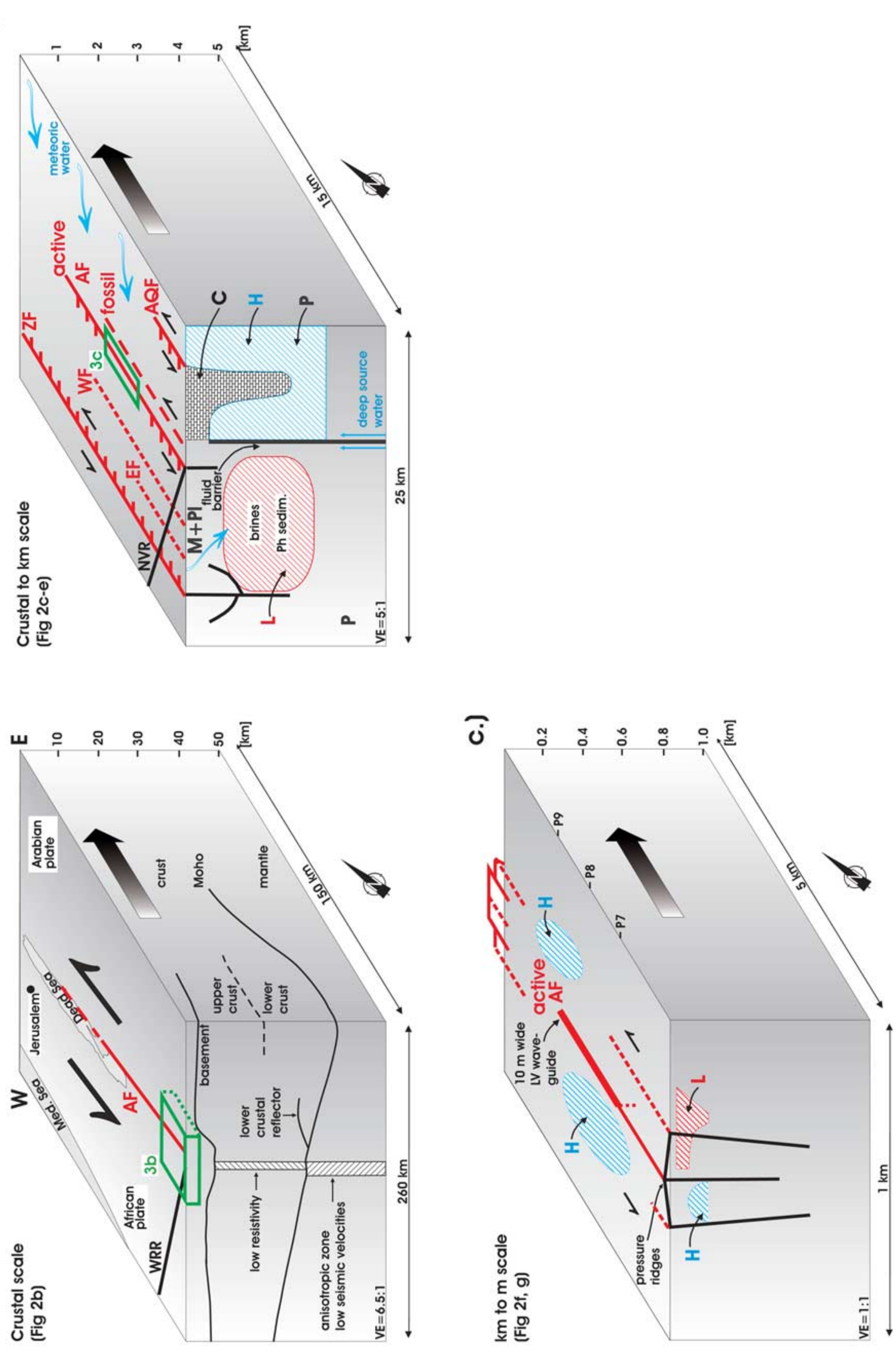
a.)
Crustal scale
(Fig 2b)
W
E
Med. Sea
Jerusalem
Dead Sea
African plate
Arabian plate
WRR
AF
3b
basement
upper crust
lower crust
crust
Moho
mantle
lower crustal reflector
low resistivity
anisotropic zone
low seismic velocities
VE=6.5:1
260 km
150 km
10
20
30
40
50
[km]
b.)
Crustal to km scale
(Fig 2c-e)
ZF
WF
3c
EF
NVR
active
AF
fossil
AQF
meteoric water
M+Pl
fluid barrier
brines
Ph sedim.
L
P
C
H
deep source water
VE=5:1
25 km
15 km
1
2
3
4
5
[km]
c.)
km to m scale
(Fig 2f, g)
10 m wide
LV wave-
guide
active
AF
H
L
pressure ridges
P7
P8
P9
VE=1:1
1 km
5 km
0.2
0.4
0.6
0.8
1.0
[km]

Figure 3

ongoing microseismic activity [e.g., *van Eck and Hofstetter*, 1989; *Salamon et al.*, 2003; *Aldersons et al.*, 2003] show that the DST is a seismically active plate boundary (Figure 4). The historical catalog goes back for more than 2000 years. It is based on documents by the local witnesses of devastating events, by pilgrims who came to the "Holy Land" shortly after the occurrence of the earthquakes, and by historians that provide detailed accounts of the history of the region including the felt earthquakes. Some of those events were catastrophic, causing casualties and widespread damage. Since no instrumental measurements were available until the end of the 19th century and most of the literate population lived north of the latitude of the Dead Sea basin, the historic earthquakes are assumed to have location errors of about 100 km (or more) [*Salamon et al.*, 1996]. The establishment of a few regional seismological stations began in the early 20th century, followed by several WWSSN stations in the mid-20th century and at about 1980 by the seismic networks of Jordan and Israel. This enabled a more accurate localization of the seismicity along the Dead Sea Transform. A. Q. Amrat et al. (The Unified Earthquake Catalog of the Dead Sea Region, 2001, http://www.relemr-merc.org/) compiled and unified the historical and instrumental catalogs of Jordan and Israel, now maintained on a regular basis, serving as a main source for seismotectonic studies and seismic hazard assessment. From Figure 4 it is obvious that the DST poses a considerable seismic hazard to Palestine, Israel, and Jordan. The present-day relative motion between Arabia and Africa is ~5 mm/a [*Klinger et al.*, 2000a; *Wdowinski et al.*, 2004; *Bartov and Sagy*, 2004; *Mahmoud et al.*, 2005; *LeBeon et al.*, 2006; *Reilinger et al.*, 2006].

[9] Because of the political situation in this area and the fact that the DST is situated in the border region between Israel and Jordan, geophysical surveys in that area are a nontrivial logistical task. Here we present the results of an integrated geoscientific investigation along a 260 km long transect (Dead Sea Rift Transect (DESERT)) extending from the Mediterranean coast to the Arabian platform. The central part of the transect crosses the DST at a location in the Arava/Araba Valley which is as far away as possible from the center of the Dead Sea, a pull-apart basin, and the Red Sea, where active rifting occurs, and thus permits the study the DST and the tectonic processes controlling it without the complications of rifting. The fieldwork completed by a team of scientists from Germany, Israel, Jordan, and Palestine started in spring 2000 and lasted until 2004. To facilitate identifying and locating the areas covered by these studies and the results of the analysis on the many scales employed, Figure 2 shows the spatially nested experiments. The areas covered are indicated sequentially by the labeled green boxes with mapped faults indicated in red. Figure 3 summarizes the results of these studies. A detailed discussion of the results leading to Figure 3 will now be given starting with the largest, the lithospheric scale.

2.1. Lithospheric Scale

[10] Using fundamental mode Rayleigh waves at intermediate periods, *Laske et al.* [2008] showed that the subcrustal *S* velocity under the region of the DST is, on average, 5% lower than in the preliminary reference Earth model (PREM) [*Dziewonski and Anderson*, 1981] down to at least 200 km. This is in agreement with the larger-scale study of *Pasyanos and Nyblade* [2007], which shows that such an area of reduced velocities in the lithosphere stretches along

Figure 3. Structure and dynamics of the AF on different scales along the DESERT transect (Figure 2). Solid red lines indicate fault traces visible at the surface, and dashed lines are buried faults. Relative motions at faults are indicated by arrows (strike slip) and ticks (minor normal motion), and buried features (bodies) are outlined at the surface by dashed areas. Red bodies ("L") are regions of low seismic velocity and low resistivity. Blue bodies ("H") are regions of high seismic velocity and moderate to high resistivity. Geological units are also labeled by letters (P, Precambrian; Ph, Phanerozoic; C, Cambrian and Cretaceous; M, Miocene; Pl, Pliocene-Pleistocene). Subsequent blow-ups are indicated by a labeled green box. (a) Tectonic setting of the Levant [see, e.g., *Garfunkel*, 1981; *Ben-Avraham*, 1985]. The left lateral displacement of 105 km is indicated by arrows. The black line at the surface is the WRR profile; compare Figure 2b. The seismic basement is offset 3–5 km under the AF, whereas the Moho shows a gradual increase from 26 to 39 km from west to east with only a maximum of ±1 km undulation under the AF. The Moho shallows to about 33 km toward the north on the eastern side. Prominent features in the crust are a lower crustal reflector under the eastern side and a subvertical zone with low resistivity located ~10 km west of the surface trace of the AF. Below the Moho a low seismic velocity and anisotropic zone with a few kilometers additional offset toward the west continues subvertically deeper into the upper mantle. Vertical exaggeration (VE) = 6.5:1. (b) Central Arava/Araba Valley in Israel/Jordan (green box in Figure 3a). The black line at the surface is the NVR profile; compare also to Figure 2c. Six left-lateral faults, three visible at the surface (solid red lines (ZF, AF, and AQF)) and three buried faults (dashed red lines (EF, WF, and fossil AF)), have been identified. A sedimentary body with low seismic velocities, low resistivity due to brines, and low densities (L) is juxtaposed opposite to a body of Precambrian age with high seismic velocities, moderate resistivity, and higher densities (H). The buried contact of these two bodies (fossil AF) is displaced 0.5–1 km toward the east with respect to the present-day surface trace of the AF (active AF). Note also geological units. The migration of fluids is indicated by blue arrows. VE = 5:1. (c) Central AF (green box in Figure 3b); compare also to Figures 2f and 2g. Several subparallel faults form the AF system on a hundred meter scale. Some of them are visible at the surface, and some are buried (dashed lines). Toward the north, pressure ridge structures dominate. Bodies with low seismic velocities and low resistivity (L) and high seismic velocities and high resistivity (H) can be identified west and/or east of the AF in the shallow subsurface. Note that L and H "bodies" are largely reversed in Figure 3c relative to Figure 3b. In the center of the sketch a ~3 km long and ~10 m wide shallow low-velocity zone detected by FZGW is indicated.

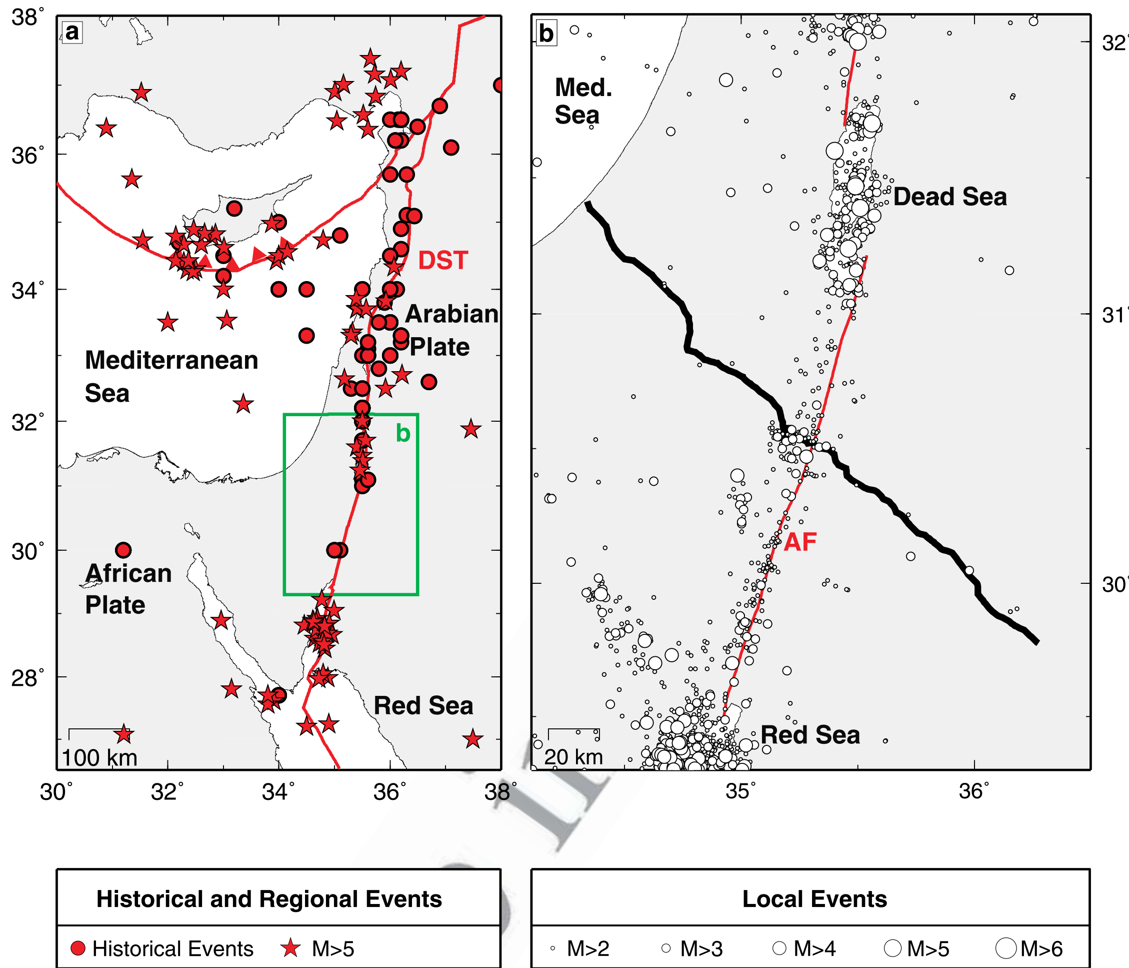

Figure 4. Seismicity of the Levant. Known faults are indicated in red. (a) Historic earthquakes of the last 2000 years are given as red dots, based on *Migowski et al.* [2004] and A. Hofstetter (personal communication, 2008). Earthquakes from 1900 to 2004 with magnitudes larger than 5 are shown as red stars (A. Hofstetter, personal communication, 2008). The area of Figure 4b is given by the labeled green box. (b) Local seismicity from 1983 to 2008 is shown as small white circles, scaled by magnitude (A. Hofstetter, personal communication, 2008). The DESERT profile is indicated in black.

the DST. This reduced value may be due to elevated temperatures connected to rifting processes in the Red Sea. The present-day conductive surface heat flow east and west of the DST, on the other hand, mimics the pre-Cenozoic thermal conditions not affected by thermal imprints. These imprints are associated with the young geodynamic processes that include the Red Sea rifting starting in the Oligocene [e.g., *McGuire and Bohannon*, 1989; *Bosworth et al.*, 2005, and references therein], the eruption and emplacement of basaltic lava flows of Oligocene and younger age [e.g., *Shaw et al.*, 2003], and the formation of the Dead Sea Transform fault system starting in the Miocene [e.g., *Garfunkel et al.*, 1981; *Garfunkel*, 1989; *Ilani et al.*, 2001; *Shaw et al.*, 2003; *Bosworth et al.*, 2005; *Sobolev et al.*, 2005]. East of the DST (Figure 2b), a surface heat flow of 60.3 ± 3.4 mW/m^2 was determined at sites virtually unaffected at shallow depth by basalt extrusions and high-heat-production granites [*Förster et al.*, 2007]. Steady state geotherms calculated on the basis of 60 mW/m^2 surface heat flow yield Moho temperatures of ~800°C at 37 km depth [*Förster et al.*, 2004]. West of the DST, geotherms based on surface heat flow of ~40 mW/m^2 [e.g., *Ben-Avraham et al.*, 1978; *Eckstein and Simmons*, 1978] imply a considerably colder lithosphere, with a Moho temperature as low as 400°C [*Stein et al.*, 1993]. Both geotherms significantly underestimate the xenolith-derived lithospheric mantle temperatures [*Stein et al.*, 1993]. This discrepancy suggests that heating in close proximity to the DST, and the region east of it, may be due to lithospheric thinning. However, the thermal pulse at depth has not yet reached the surface owing to the time/length scale of thermal diffusion through the lithosphere [e.g., *Turcotte and Schubert*, 2002]. *Laske et al.* [2008] find an 80 km thick lid of normal *S* velocity, to the west of the DST, indicative of thermally unaffected crust and upper mantle. The whole region is furthermore underlain by an upper mantle, down to 410 km depth, with 3–4% reduced *S* velocities compared to PREM [*Mohsen et al.*, 2006].

[11] Tomographic inversion of body waves (*P* and PKP phases) from 135 seismic events recorded at the 48 stations

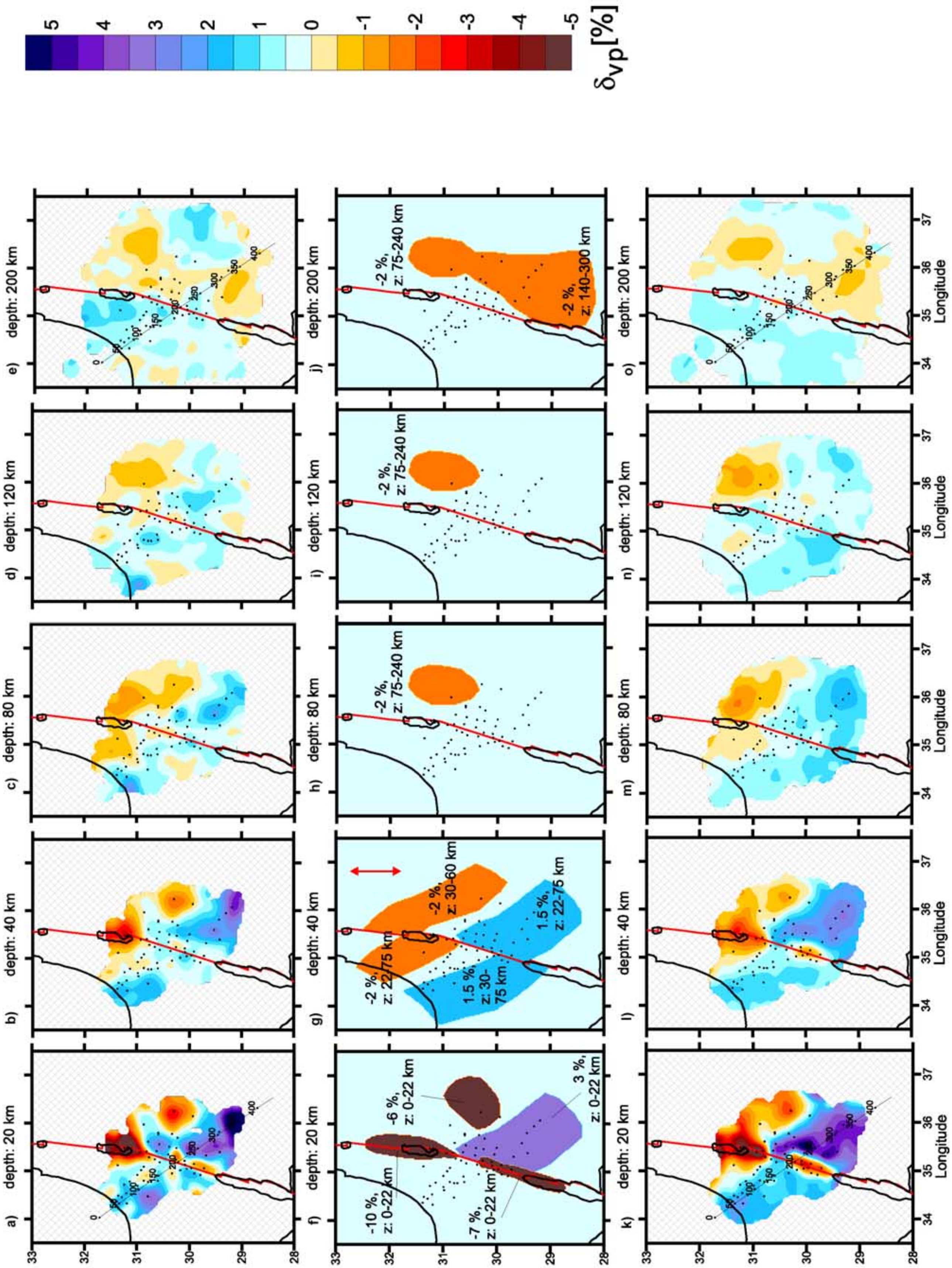
δvp[%]
a) depth: 20 km
b) depth: 40 km
c) depth: 80 km
d) depth: 120 km
e) depth: 200 km
f) depth: 20 km
g) depth: 40 km
h) depth: 80 km
i) depth: 120 km
j) depth: 200 km
k) depth: 20 km
l) depth: 40 km
m) depth: 80 km
n) depth: 120 km
o) depth: 200 km
-10 %, z: 0-22 km
-6 %, z: 0-22 km
-7 %, z: 0-22 km
3 %, z: 0-22 km
-2 %, z: 22-75 km
-2 %, z: 30-60 km
1.5 %, z: 30-75 km
1.5 %, z: 22-75 km
-2 %, z: 75-240 km
-2 %, z: 140-300 km
Latitude
Longitude

Figure 5

of the passive long-term deployment of DESERT (triangles in Figure 2b) is used to image the *P* velocity in the upper mantle under the DST [*Koulakov et al.*, 2006]. After correction for surface topography and crustal thickness the amplitudes of the remaining subcrustal travel time anomalies are small. Figure 5 shows the results of the inversion and corresponding resolution tests. One robust feature is the high-velocity *P* wave anomaly of about +1% from ~40 to 120 km depth in the SE (Figures 5a–5e), which could be due to a slightly lower temperature ($\Delta T < -100°$C) and/or a preexisting lithospheric compositional anomaly in this region. Very little topography of the lithosphere-asthenosphere boundary is observed beneath the DST. This observation is confirmed by receiver function studies [*Mohsen et al.*, 2006] showing a typical lithosphere-asthenosphere thickness of ~70 km east and south of the DST and an increase to 80 km in the north on the eastern side of the DST. Otherwise, no significant *P* velocity anomalies are observed in the upper mantle under the DST. The boundary between the African and the Arabian plate is detected underneath the DST in the subcrustal lithosphere as a narrow, ~20 km wide zone of anisotropic velocity, most likely produced by fault-parallel mineral alignment in response to finite strain.

[12] Figure 6 shows the range of possible models (three clusters of models), based on the inversion of shear wave splitting observations (SKS waves) along the 100 km long near-vertical reflection (NVR) line (white line in Figure 2b) [*Rümpker et al.*, 2003; *Ryberg et al.*, 2005]. The preferred model is cluster 1. It shows that this zone, accommodating the transform motion between the African and the Arabian plate, is displaced ~10 km to the west relative to the surface trace of the AF. The geometry of this zone with an increased anisotropy of ~1.8% and a change in orientation of more than 10° with respect to the neighboring domains suggest subhorizontal, fault-parallel mantle flow within a vertical boundary layer that extends through the entire lithosphere. Interestingly, the width and position of this boundary layer in the upper mantle agree with the zone of relatively low resistivity obtained from the magnetotelluric studies (see section 2.2). The velocity anomaly below the crust, which is also slightly displaced toward the west relative to the surface trace of the AF (Figures 7d and 7i), agrees with the zone of anisotropic velocities detected in the SKS splitting studies (Figure 6). The apparent contradiction of substantial variation of seismic anisotropy beneath the DST and of a seismological homogeneous mantle under the DST found by *Koulakov et al.* [2006] is resolved by the observation that even for high seismic anisotropy in such a vertical zone the travel time residuals of subvertical *P* wave paths are close to zero [*Sobolev et al.*, 1999]. Interestingly, all thermomechanical models of the DST have a similar 20–30 km wide zone of shear flow located beneath the major fault that cut through the entire lithospheric mantle [*Sobolev et al.*, 2005].

[13] Other estimates on the lateral extent of fault zone related deformation based on inferences of seismic anisotropy range from ~40 km for the Altyn Tagh fault in Tibet [*Herquel et al.*, 1999] to 335 km for the Alpine fault in South Island, New Zealand [*Baldock and Stern*, 2005]. This indicates that the width of the decoupling zone increases with the total strain accumulated along the fault as suggested by the analysis of *Baldock and Stern* [2005]. However, for transtensional environments, e.g., within the India-Asian collision zone, some observations show a continuous rotation of SKS fast directions across the faults [*McNamara et al.*, 1994], which may be indicative of neighboring regions of relatively abrupt changes in anisotropy [*Rümpker and Ryberg*, 2000]. In these cases the width of the vertical boundary layer may be reduced because of the more significant compressional component of deformation.

2.2. Crustal Scale

[14] Results of a simultaneous inversion of regional seismic phases for source location (not shown), Moho depth, and 3-D *P* and *S* velocity in crust and the uppermost mantle under the DST are given in Figures 7 and 8 [*Koulakov and Sobolev*, 2006]. The Moho depth increases strongly toward the east (Figure 8). Under Israel/Palestine the crust is similar to a thin continental margin, and under the Levant basin it is either the same or oceanic [*Netzeband et al.*, 2006]. The narrow, NNE–SSW striking low-velocity *P* and *S* velocity anomaly identified in Figure 7 marks the position of the DST and is interpreted as sediments and a zone of fractured and deformed rocks in the middle and lower crust [*Koulakov and Sobolev*, 2006].

[15] In magnetotelluric (MT) images a 3–5 km wide, subvertical conductor (Figure 9, fault conductor 1 (FC1)) is detected in the crust and upper mantle west of the AF. It is spatially confined even in the ductile lower crust, but the bottom of the conductor is not resolved. Therefore, it might even penetrate the lithospheric upper mantle. The width and location of the conductor may correspond to the core of the lithospheric-scale shear zone which continues upper crustal faults down through the entire lithosphere [*Sobolev et al.*, 2005] (see also section 2.5 for more discussion). This statement is in general agreement with the anisotropic vertical boundary layer in SKS splitting (Figure 6) and the

Figure 5. *P* velocity variation in the uppermost mantle under the DST based on tomographic inversion of 3366 P and PKP phases recorded at the 48 stations of the passive long-term deployment of DESERT (triangles in Figure 2b). The color bar gives the *P* velocity deviation in % (δVp) from the reference model (IASP91 [*Kennett and Engdahl*, 1991]). (a–e) *P* velocity anomalies. (f–j) Synthetic model with description of anomaly parameters (amplitude and depth interval). Note the arrow indicating the offset of ~100 km in Figure 5g. (k–o) Synthetic *P* wave anomalies model using the synthetic model and the same ray configuration and parameters as in the data; noise with a root-mean-square (RMS) of 0.14 s is added. The synthetic model provides 35% of variance reduction and 0.22 s of data RMS, similar to those observed in the case of real data inversion. Modified from *Koulakov et al.* [2006], copyright 2006, Elsevier.

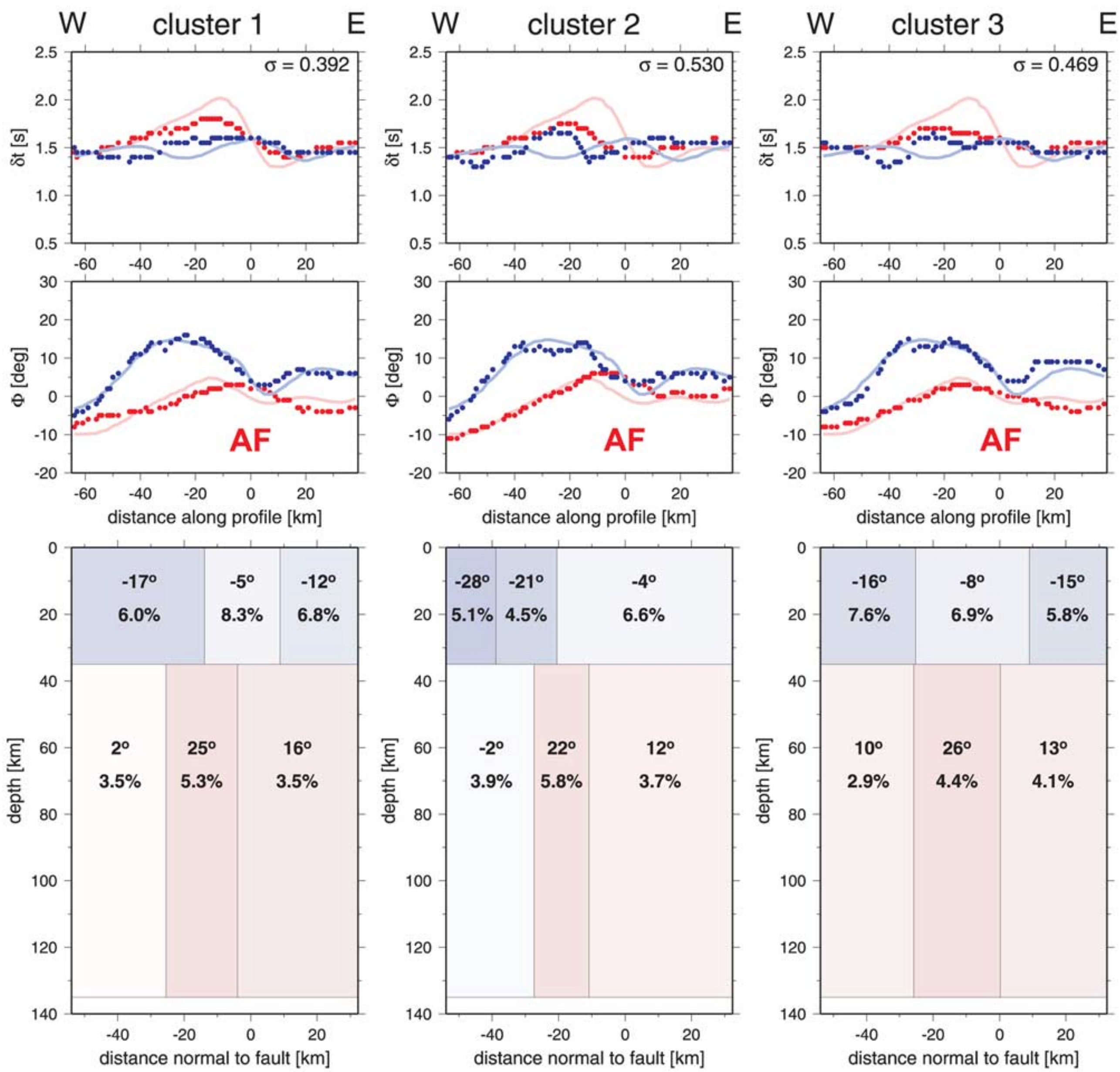

Figure 6. Model range of possible *P* wave velocity anisotropy in the crust and uppermost mantle under the DST on the 100 km long NVR profile (white line in Figure 2b) perpendicular to the AF (at 0 km). (bottom) Models for the three typical clusters of solution given by *Ryberg et al.* [2005]. The preferred model cluster is cluster 1 [see also *Rümpker et al.*, 2003]. The azimuth of the symmetry axis and the magnitude of the anisotropy are given in each block. (middle) Corresponding fast polarization direction Φ. Red corresponds to the period band 5–7 s, and blue corresponds to the results for the period band 2–5 s. Light red and light blue are the smoothed observed splitting parameters. (top) Corresponding delay time δt. All models are characterized by a central upper mantle zone of increased anisotropy, which is differently oriented with respect to its neighbors. Typical features of model cluster 1 are ≈20 km wide anisotropic zones in crust and upper mantle, model cluster 2 has typically narrower anisotropic zones, and model cluster 3 has broader crustal and upper mantle anisotropic zones. Modified from *Ryberg et al.* [2005].

region of low *P* and *S* velocity below the Moho (Figure 7), which also show anomalies displaced toward the west relative to the surface trace of the AF but do not have the lateral resolution of the MT experiment. The enhanced conductivity of FC1 could be explained by a pathway for fluids from the mantle or lower crust. Alternatively, this region could have become permanently conductive by precipitation of conducting minerals such as graphite during the transform motion. The second large fault conductor appears at middle to lower crustal levels and could be related to the Al Quwayra Fault (AQF) (fault conductor 2 (FC2) in Figure 9). Interestingly, FC2 appears to terminate

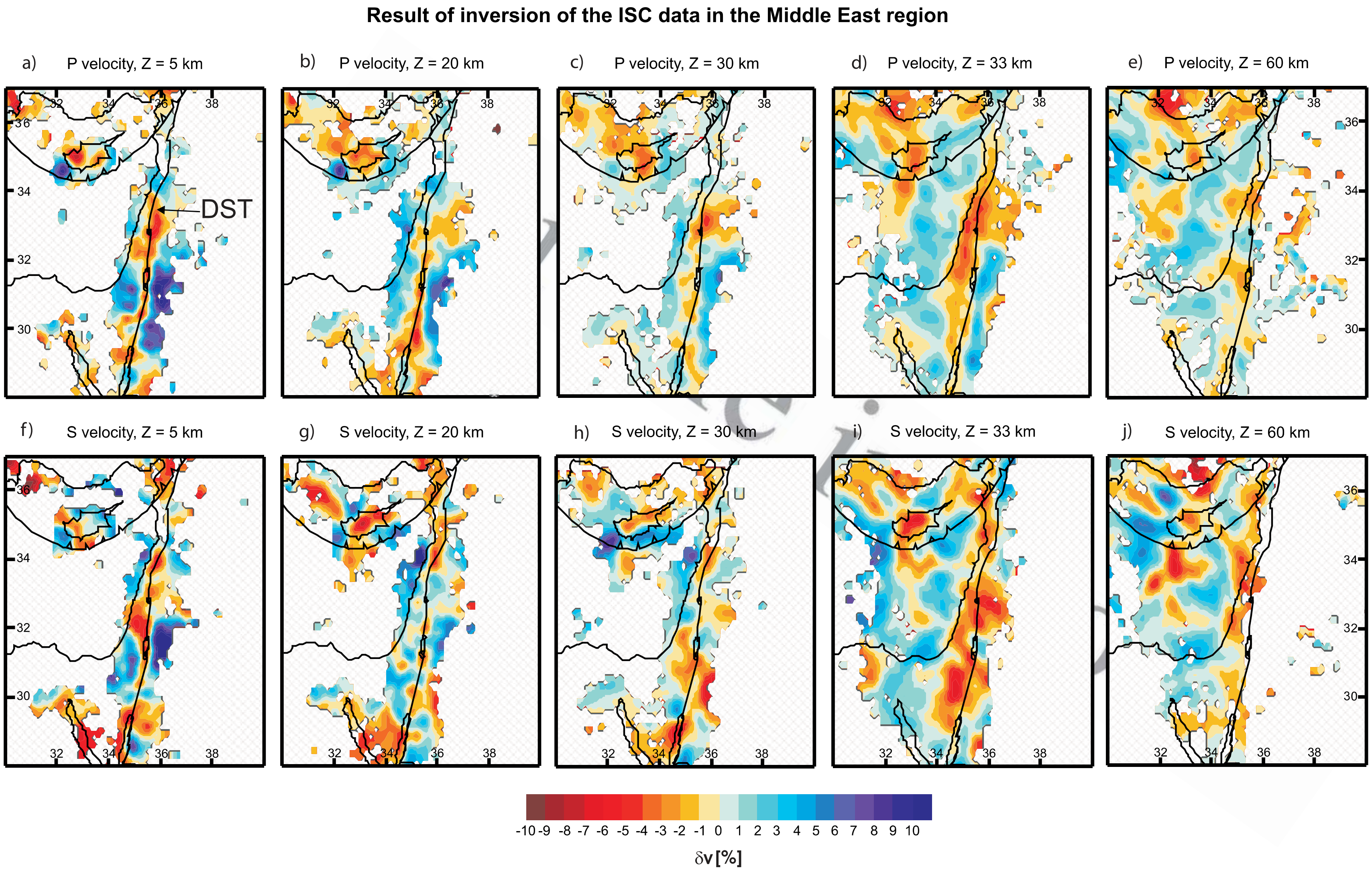

Figure 7. Crustal and uppermost mantle velocity anomalies (δv in % relative to AK135 [*Kennett et al.*, 1995]) in the Levant derived from regional earthquakes and seismic networks. (a–e) P velocities. (f–j) S velocities. The color bar gives the anomalies in percent. Modified from *Koulakov and Sobolev* [2006], copyright Blackwell Publishing.

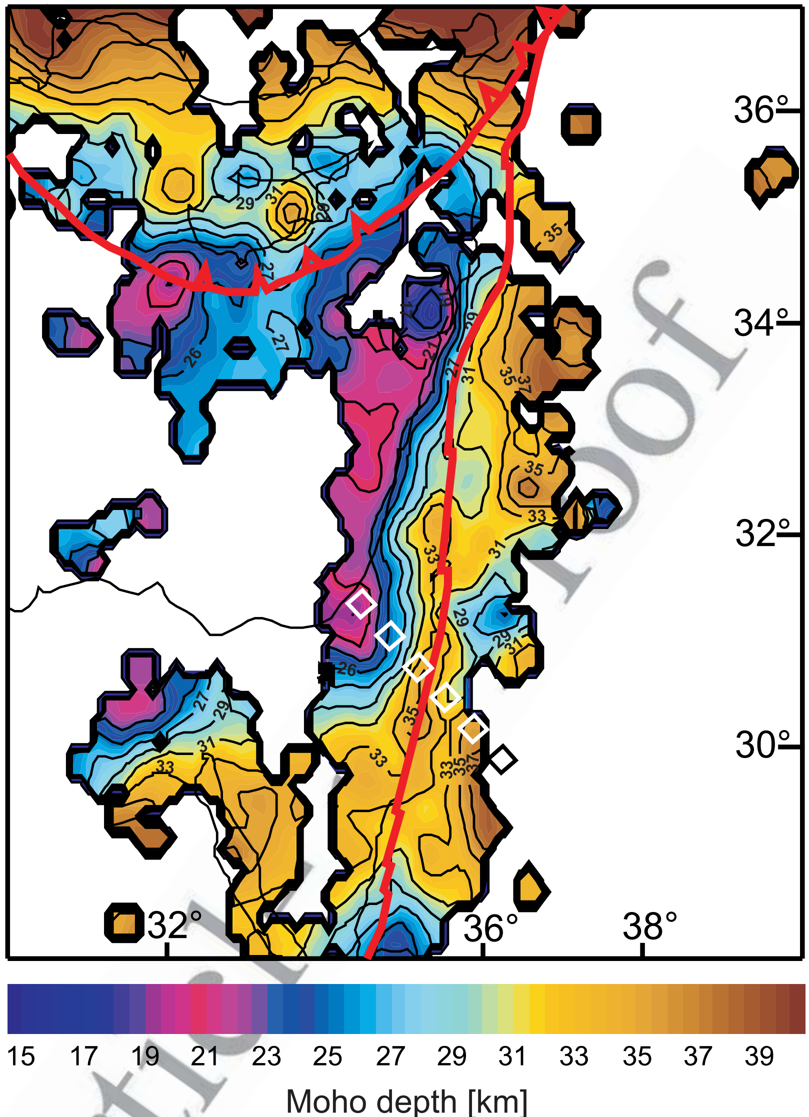

Figure 8. Crustal thickness in the eastern Mediterranean region derived from regional earthquakes and seismological networks in the Levant. The Moho depth was obtained simultaneously with the velocity model shown in Figure 7. The red lines are plate boundaries, the black lines are coast lines, and the white boxes indicate the DESERT profile. The color bar gives the depth of the Moho in kilometers. Modified from *Koulakov and Sobolev* [2006], copyright Blackwell Publishing.

at the lower crustal reflector (LCR), discussed later in this section in more detail.

[16] The results of a combined refraction/reflection survey from the Mediterranean to the Jordan highlands (black and white line in Figure 2b) are shown in Figures 10 and 11c, respectively. The top two layers (Figure 10) consist predominantly of sedimentary rocks with the seismic basement below them offset by 3–5 km near the DST. Since the wide-angle reflection/refraction (WRR) profile lies 30° off the proposed symmetry axis derived from *S* wave (SKS) splitting (Figure 6), the difference of the two *S* waves in the controlled source WRR experiment (N–S and E–W) is too small to be detected. The *P* and *S* wave velocity sections in Figure 10 show a steady increase in the depth of the Moho from ~26 km at the Mediterranean coast to ~39 km under the Jordan highlands, with only a small but visible asymmetric topography of the Moho under the DST. The lack of significant uplift of the Moho under the DST, with the Moho topography varying only ±1 km, argues strongly against a potential extensional rift structure in this area. The *S* wave velocities (Figure 10b) and the corresponding Poisson's ratios (Figure 10c) for the seismic basement can be explained by felsic compositions typical for continental upper crust, while those for the lower crust are representative of a mafic composition characteristic for continental lower crust. These findings, of typical nonextended continental crust, a fact also corroborated by the gravity data discussed later in this section, again speak strongly against extensional processes in this area. The spatial coverage of Moho topography is extended using the receiver function method (RFM) for teleseismic data recorded at the stations of the passive long-term deployment of DESERT (triangles

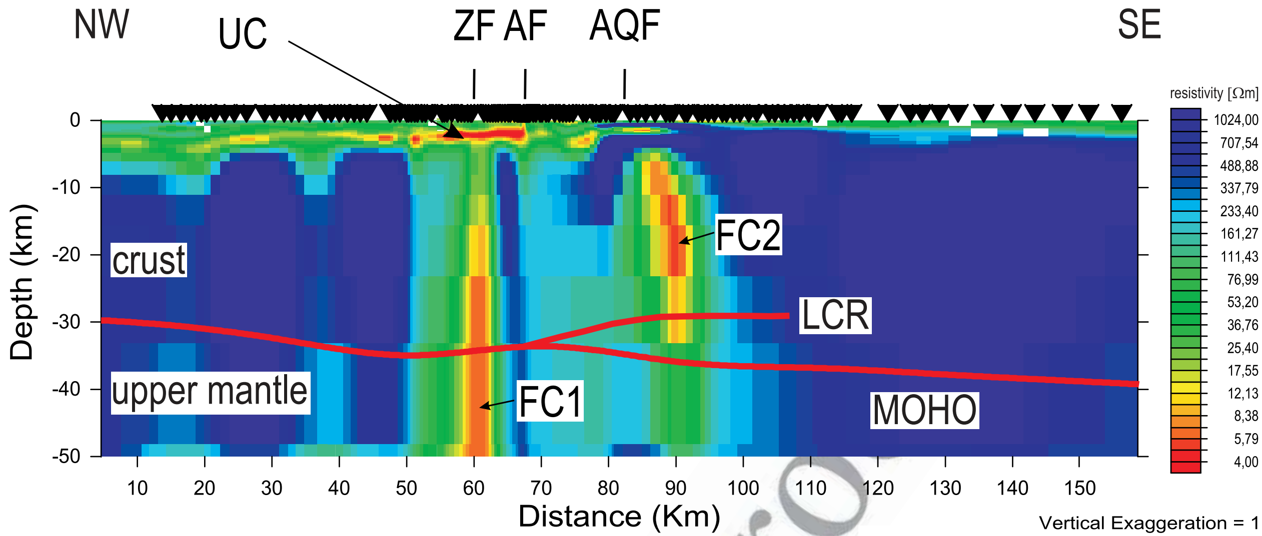

Figure 9. Regional-scale electrical resistivity cross section in Ω m along the magnetotelluric profile given as light blue dots in Figures 2b and 2d. Red and yellow indicate good conductors. The red lines are the Moho and the lower crustal reflector (LCR) determined from seismics and seismology; see Figures 10 and 11 and *DESERT Group* [2004], *Mechie et al.* [2005], and *Mohsen et al.* [2005]. UC is an upper crustal conductor between ~1.5 and 4 km depth, truncated toward the east at about the AF (for more details, see Figure 15 and discussion there). The locations of the ZF, the AF, and the AQF are indicated for orientation. These faults are associated with deep subvertical zones of high conductivity (fault conductor 1 (FC1) and fault conductor 2 (FC2)). Note also the corresponding seismic velocity anomalies in the lower crust and upper mantle west of the AF in Figure 6. The FC2 anomaly, associated with the AQF, appears to terminate at the LCR. No vertical exaggeration is applied. Modified from *Ritter et al.* [2005b].

in Figure 2b) and four permanent stations of the Israel and Jordan seismic networks [*Mohsen et al.*, 2005]. The Moho depth values under these stations are shown in Figure 11a. The depth of the Moho across the DST increases smoothly from about 30 km through 34–38 km toward the east, in agreement with the WRR data, but also shows significant north-south variations east of the DST, in agreement with gravity data discussed later in this section. The depth of the discontinuity associated with the LCR (see previous paragraph) and identified east of the DST (RFM study of *Mohsen et al.* [2005]), is shown in Figure 11b. Figure 11c shows the excellent agreement of the depth determination of the Moho and the LCR along the DESERT profile between the steep-angle (line drawing) and wide-angle (red band) controlled source techniques and the passive data RFM results (green and yellow symbols, respectively). The LCR is interpreted as horizontal north-south oriented shearing at this plate boundary, a process occurring also in the thermomechanical simulation of *Sobolev et al.* [2005] (see, e.g., Figures 24d–24f). On the other hand, the LCR in the NVR profile (line drawings in Figure 11c) and the corresponding intermittent reflections in the WRR *P* wave data mainly east of the DST, from ~30 km depth, could also be from mafic intrusions associated with the nearby Cenozoic volcanism [*DESERT Group*, 2004]. The RFM data and the controlled source data can both be satisfied if the LCR comprises a small first-order discontinuity underlain by a ~2 km thick transition zone [*Mechie et al.*, 2005].

[17] Further constraints come from 3-D density modeling by *Götze et al.* [2006]. The 3-D density model is based on the newly compiled Bouguer anomaly for the area of the DST (Figure 12, top). Three cross sections across the DST are displayed in Figure 13. The density model along a profile coinciding with the WRR and NVR profiles (Figure 13b) matches well with the structure from the seismic data (black line in Figure 2b). The most negative Bouguer anomalies along the DST are mainly caused by the deep low-density sedimentary basins (most prominently the Dead Sea basin with sediment thicknesses of 8–12 km [*Garfunkel and Ben-Avraham*, 1996, 2001; *Ginzburg and Ben-Avraham*, 1997; *Ben-Avraham and Lazar*, 2006; *Ben-Avraham and Schubert*, 2006; *Ben-Avraham et al.*, 2008]), whereas a shallow zone of high-density intrusion at 31°N, 36°E coincides with the local maximum gravity on the eastern flank of the DST. However, the Bouguer anomalies are, in general, characterized by higher values of 0 to −20 mGal in the NW and lower values of −60 to −80 mGal in the SE of the region (Figure 12, top). This trend reflects the gradual thickening of the crust from the Mediterranean toward the Jordan highlands found with the RFM (Figure 11). The gravity-derived Moho depth matches the RFM values. Therefore, the western region, near the Mediterranean, is characterized by the thinnest crust, whereas the Jordan highlands in the southeast are characterized by the thickest crust of 38–42 km (Figure 12, bottom). The thickness (up

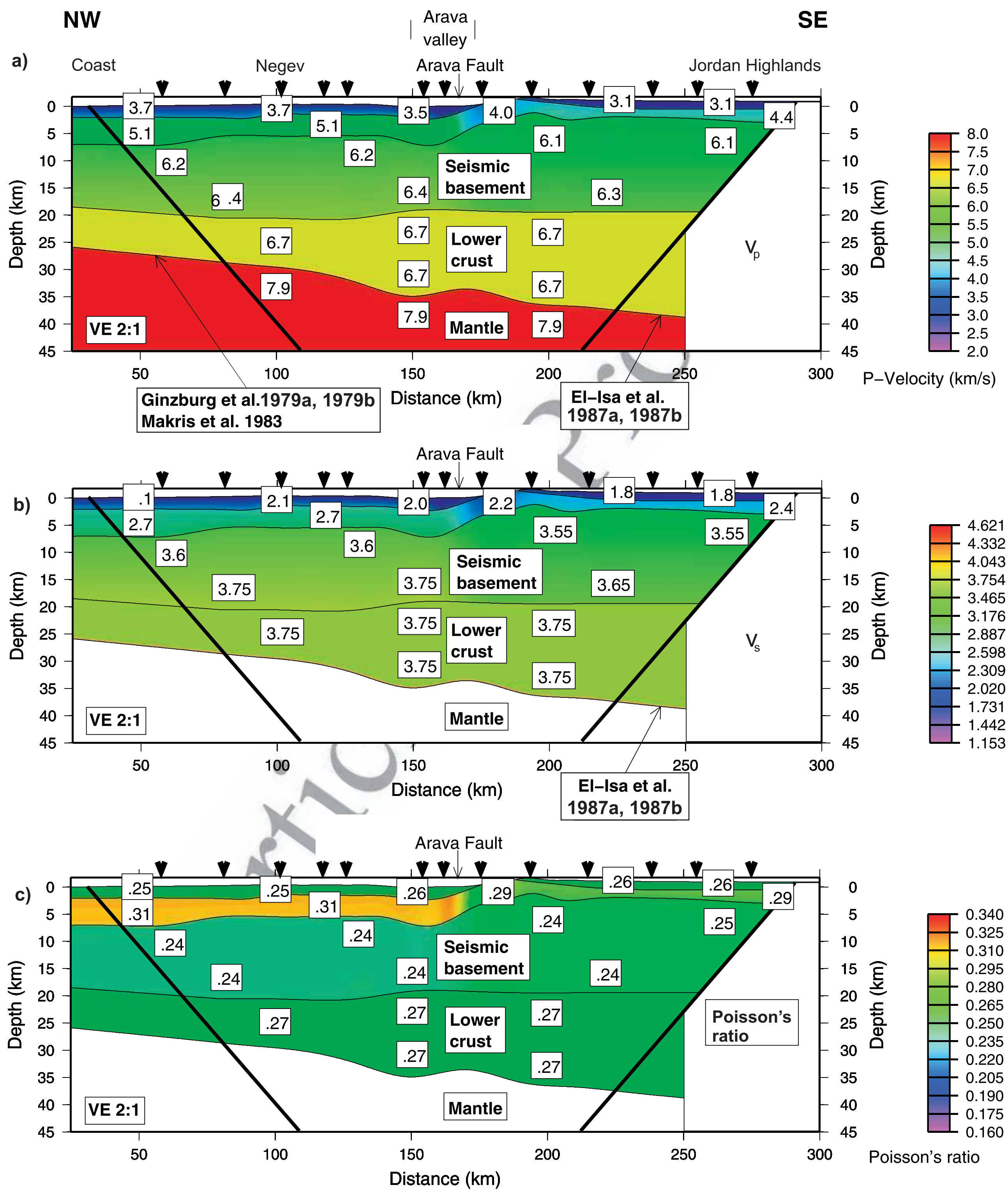

Figure 10. Crustal *P* and *S* velocity structure under the 260 km long WRR profile (black line in Figure 2b) from the Mediterranean coast (NW) to the Jordan highlands (SE). (a) *P* velocity model [after *DESERT Group*, 2004]. (b) *S* velocity model. (c) Corresponding Poisson's ratio model. Velocities are in km/s. Triangles at the top of each section represent the shot points. Only the region within the diagonal lines is resolved in this study. To the NW the boundaries and *P* wave velocities are based on previous work by *Ginzburg et al.* [1979a, 1979b] and *Makris et al.* [1983], while to the SE the boundaries and the *P* and *S* wave velocities are based on *El-Isa et al.* [1987a, 1987b]. Note vertical exaggeration of 2:1. Modified from *Mechie et al.* [2005], copyright Blackwell Publishing.

to 38–42 km) and density of the crust confirm again that the region of the DST is underlain by continental crust.

[18] In summary, integration of fundamental Rayleigh waves, body wave tomography, RFM, and shear wave splitting with *P* and *S* waves from controlled sources, combined with MT studies and 3-D gravity data, allows us to derive an image of the AF on the crustal scale (Figure 3a). The combination of all the findings above suggests localized deformation and

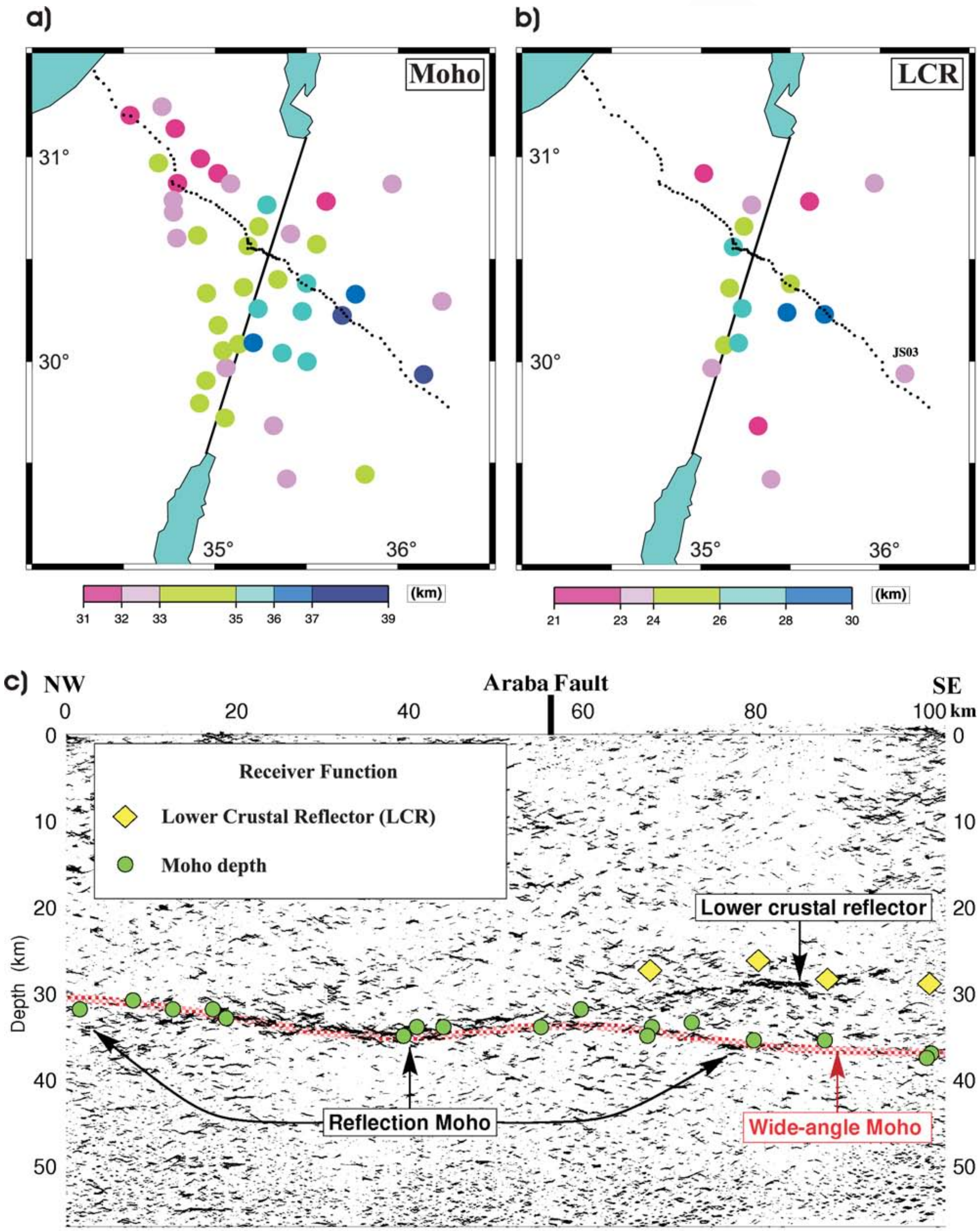

Figure 11

subhorizontal mantle flow within a narrow vertical boundary layer that extends through the entire lithosphere. We conclude that rift-type deformation did not play a dominant role in the dynamics of the DST, a fact supported by the results of *Sobolev et al.* [2005]. All observations can be linked to the left-lateral movement of the two plates, accompanied by strong deformation within a narrow zone of minimum lithospheric strength cutting through the entire crust, consisting most likely of fault-parallel mineral alignment beneath the AF that also gives rise to significant seismic anisotropy.

2.3. Kilometer to Meter Scale

[19] The elongated structure of the rift-like DST is composed of a series of large basins (the Dead Sea being the most prominent one), which are mainly attributed to dilatational jogs related to the left-lateral strike-slip motion. The formation of the Gulf of Aqaba/Elat had also been associated with pull-apart structures [*Garfunkel*, 1981; *Ben-Avraham*, 1985; *Garfunkel and Ben-Avraham*, 2001; *Ben-Avraham et al.*, 2008]. Along the AF the "rift" valley is further divided into a series of smaller subbasins [*ten Brink et al.*, 1999a]. Our study area is situated at the southern termination of the Dead Sea Basin. The fault-bounded structure of this depression had previously been revealed by commercial multichannel seismic reflection and borehole data, which suggested an asymmetric, graben geometry of flat subhorizontal strata of Miocene to recent sediment fill that becomes shallower toward the south [*ten Brink and Ben-Avraham*, 1989; *Garfunkel*, 1997; *Gardosh et al.*, 1997; *Zak and Freund*, 1981; *Neev and Hall*, 1979; *Rotstein et al.*, 1991; *Ginzburg and Kashai*, 1981; *Kashai and Croker*, 1987]. The Miocene Hazeva formation is considered the oldest basin fill unit, overlain by massive evaporite beds and sequences of marl, clay, sand, and gravel [*Gardosh et al.*, 1997; *Zak*, 1967; *Garfunkel*, 1997]. A number of normal, often listric, faults dominate the structure in the southern Dead Sea Basin [*Gardosh et al.*, 1997]. The western side of our study area was previously analyzed by high-resolution seismic profiles [*Bartov et al.*, 1998; *Frieslander*, 2000]. Several prominent faults cut the western half of the Arava/Araba Valley, with the subvertical Zofar Fault (ZF, Figure 2) being the most prominent. In the uppermost kilometer west of the ZF, Cretaceous and Permian rocks are found, while younger strata related to the Dead Sea Basin are exposed east of it [e.g., *Ritter et al.*, 2003]. Toward the center of the Arava/Araba Valley, additional north-south striking faults were found at this longitude, often joining at depth forming negative flower structures [*Frieslander*, 2000].

[20] To study the uppermost crust in the vicinity of the AF in more detail, tomographic inversion techniques were applied to over 280,000 travel time picks of refracted *P* waves along the NVR line (red line in Figure 14a) [*Ryberg et al.*, 2007]. The *P* velocity structure is well resolved down to a depth of several kilometers (Figure 14b). It shows features that correlate well with surface geology, calibrated by boreholes in the vicinity of the DST [*Fleischer and Varshavsky*, 2002; *Bartov et al.*, 1998; *Frieslander*, 2000]. The tomographic *P* velocity model (Figure 14b) is characterized by a thin layer (few 100 m) of low velocities (<2.6 km/s) in the depression containing the AF (range 40–60 km). Geology (Figure 14a) confirms that Quaternary alluvium (unconsolidated) is thin throughout this depression, which is underlain by consolidated sediments ranging in age from Jurassic to Miocene. Basement velocities (>5.0 km/s), interpreted as Precambrian igneous and metamorphic rocks (Figure 14c), are found at a depth of ~2 km below sea level west of the AF and 0–1 km below sea level east of the AF. Strong lateral velocity gradients (steps) are located at the following mapped faults, in order of step size: AF, Al Quwayra, Zofar, and Barak. The high-velocity block on the east side of the AF is interpreted as a high-standing sliver of the crystalline basement. The lithological contrast to the sediment basin west of it could create a hydrological barrier; see Figure 15 and *Ritter et al.* [2003], *Maercklin et al.* [2005], and *Bedrosian et al.* [2007] for details.

[21] Magnetotelluric and seismic models [*Ritter et al.*, 2003; *Maercklin et al.*, 2005; *Ryberg et al.*, 2007] provide complementary information about the resistivity and velocity structure of the subsurface (Figures 15a and 15b), respectively. Using a new classification approach these independently derived models can be combined to map the subsurface structure where regions of high correlation (classes) provide structural and lithological information not always evident in the individual models [*Bedrosian et al.*, 2007]. This method was applied to a 10 km long profile across the AF (seismics (central part of the NVR profile in Figure 2c) and coinciding magnetotellurics (Figure 2d)). Six prominent lithological classes are identified providing a clear delineation of stratigraphy in accordance with geologic results (Figure 15c and Table 1). All classes except 1 and 6 are truncated at the AF. Classes 1 and 2 show typical values of igneous or metamorphic rocks (high-velocity sliver in Figure 14b), classes 5 and 6 can be attributed to sedimentary

Figure 11. Depth of Moho and the LCR in the vicinity of the DST combined with the 2-D reflection seismic image across the DST. (a) Map of Moho depth from *Mohsen et al.* [2005] derived using the receiver function method (RFM) at the stations of the passive long-term DESERT deployment (triangles in Figure 2b). The dotted line indicates the WRR profile. The Moho is deepest near the southeastern end of the DESERT profile and shallowest at the northwest. (b) Map of LCR (see also Figure 11c) occurring mainly east of the DST. (c) Automatic line drawing of the depth-migrated seismic common depth point section of the NVR experiment [after *DESERT Group*, 2004]. The black arrows mark the drop-off of reflectivity, generally interpreted as the Moho in seismic reflection data. The red band indicates the location of the Moho as derived from the WRR experiment in Figure 10a. The green and yellow symbols indicate the Moho and the LCR as determined with the RFM in Figures 11a and 11b, respectively, in a ~20 km wide corridor along the DESERT profile. Modified from *DESERT Group* [2004] and *Mohsen et al.* [2005] (copyright Blackwell Publishing), respectively.

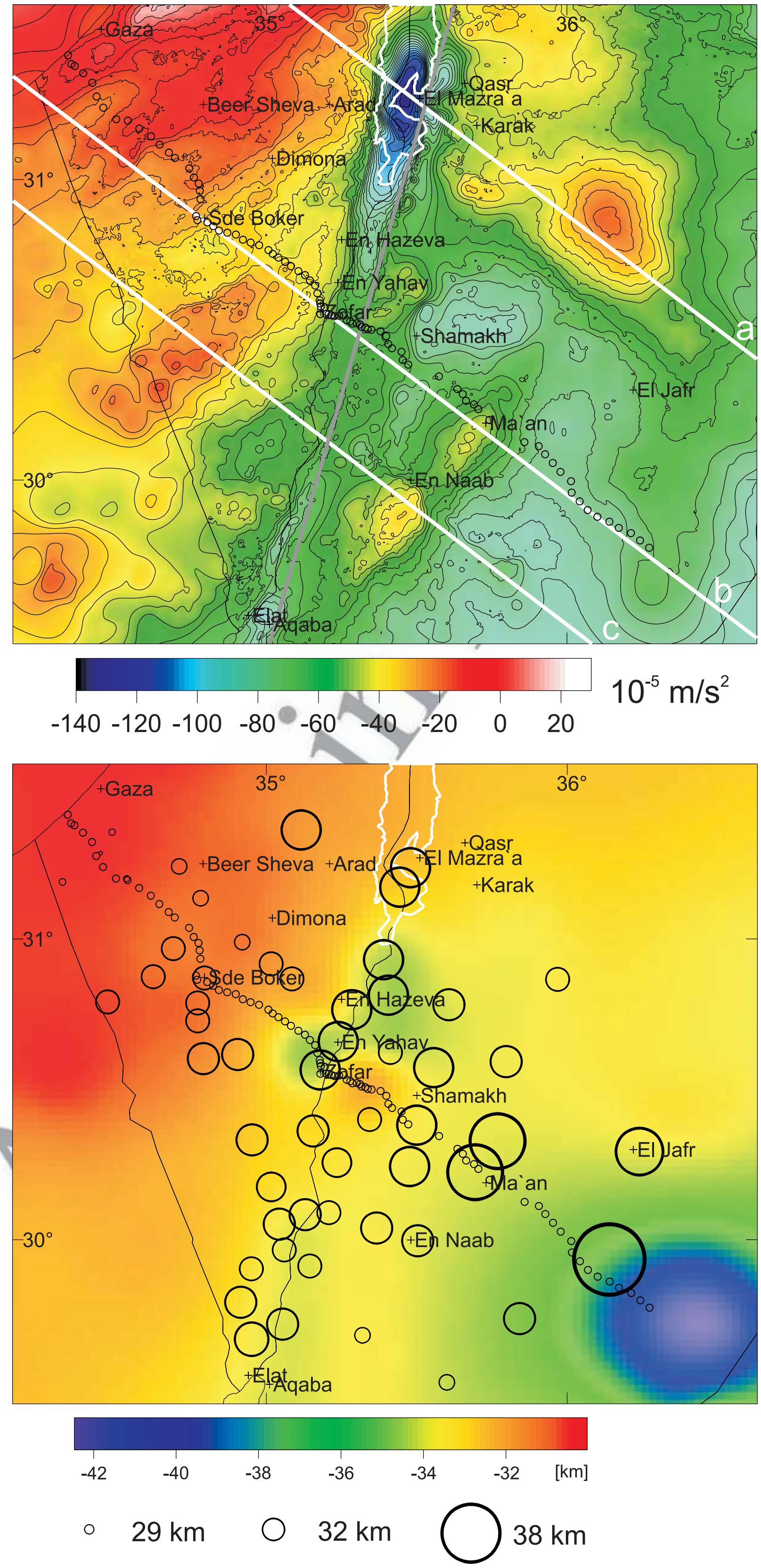

Figure 12. Bouguer anomaly and the gravity-derived Moho depth in the vicinity of the DST. (top) Measured (complete) Bouguer anomaly. The three white lines, subparallel to the seismic profile, mark the positions of the profile view cross sections shown in Figure 13. The WRR profile is indicated by small black circles. (bottom) Moho depth beneath the 3-D gravity modeling area. Also shown is the Moho depth (open circles) from the RFM [*Mohsen et al.*, 2005]. Modified from *Götze et al.* [2006] with kind permission of Springer Science and Business Media.

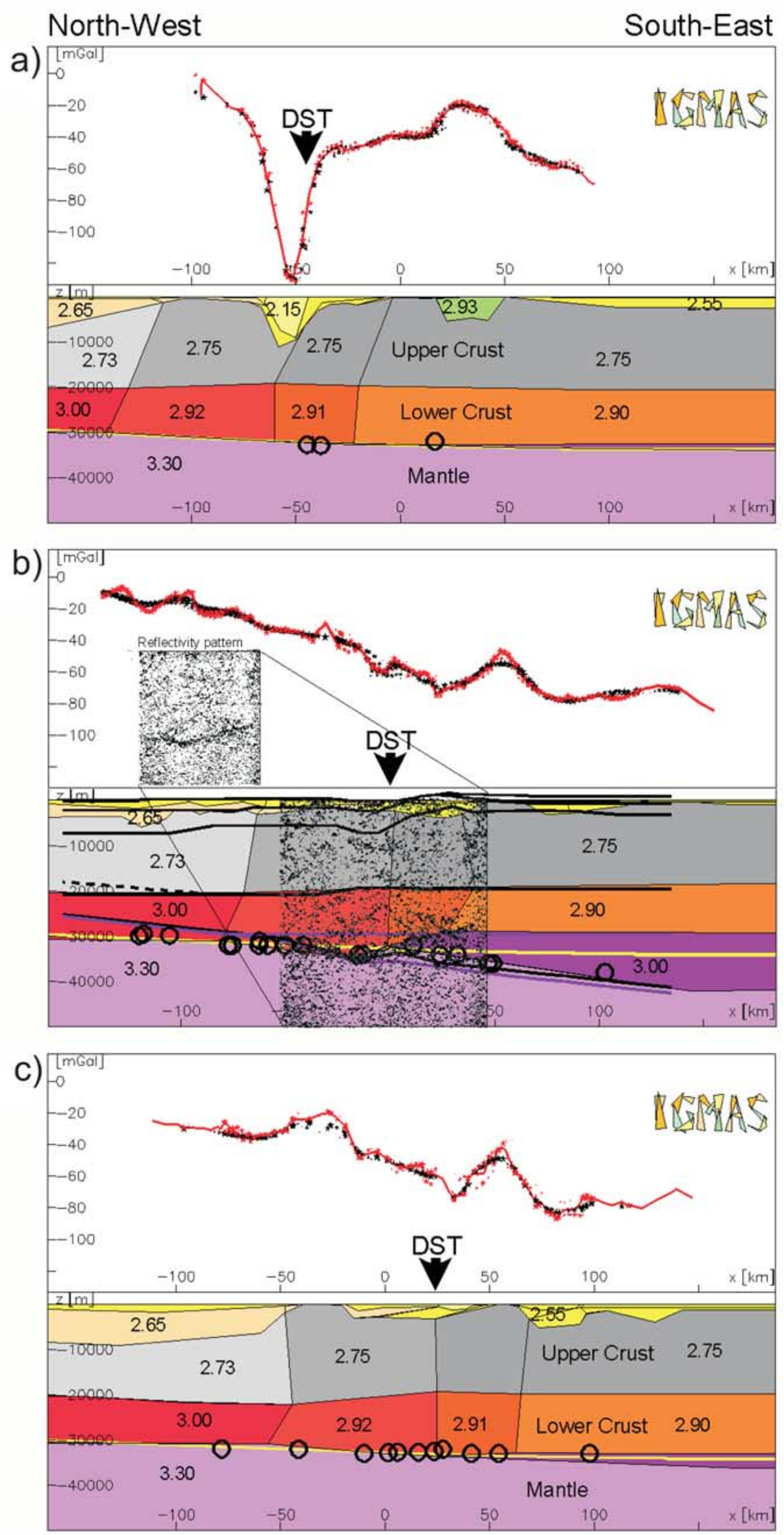
North-West
South-East
a)
b)
c)
[mGal]
IGMAS
DST
Reflectivity pattern
z [m]
x [km]
Upper Crust
Lower Crust
Mantle
2.65
2.73
2.75
2.15
2.93
2.55
3.00
2.92
2.91
2.90
3.30

Figure 13

rocks, and class 4 shows typical values of clastic or consolidated sediment at sufficient depth to have undergone compaction. Class 3 shows moderate seismic velocities, similar to class 4, but extremely low resistivity, lower even than that found in the surface sediments. The most plausible explanation for this class is the presence of a few percent of hypersaline fluid [*Ritter et al.*, 2003; *Maercklin et al.*, 2005; *Bedrosian et al.*, 2007]. This is consistent with the observation of saline brines within the Zofar 20 well a few kilometers west of the study area. Class 3 terminates along a vertical plane ∼500 m east of the surface trace of the AF. For a more detailed discussion of this buried fault (fossil AF (FAF)), see *Maercklin et al.* [2004, 2005] and *Kesten et al.* [2008]. The change in lithology across the AF, from classes 3, 4, and 5 in the west to class 2 in the east, suggests that the fault is, at most, a few hundred meters wide, at a depth of 0.5–3.0 km below the surface. The vertical uplift of the basement is at least 1.3 km, which is in accordance with gravity modeling [*Tašárová et al.*, 2006].

[22] A 3-D image of the electrical conductivity across and along the AF (Figure 16) reveals the continuation of the upper crustal brine zone toward the north. The AF seems to act primarily as an impermeable barrier to cross-fault fluid transport. However, the conductivity images do not reveal a pronounced fault zone conductor associated with the damage zone of the fault as it has been observed, e.g., at the SAF [*Unsworth et al.*, 1999, 2000; *Bedrosian et al.*, 2002; *Becken et al.*, 2008] and the West Fault in Chile [*Hoffmann-Rothe et al.*, 2004].

[23] A 3-D image of seismic contrasts along a 7 km long stretch of the central AF between 1 and 4 km depth (Figure 17) is derived from arrays of controlled seismic sources and receivers, respectively (controlled source arrays (CSA) I experiment; for details, see *Maercklin et al.* [2004]). The well-resolved 7 km wide area (from ∼3 to 10 km in the y direction in Figure 17) begins ∼1 km north of line 1 and ends ∼1 km south of line 3 (Figure 2f). Using a 3-D seismic migration method based on beam forming and coherency analysis of P-to-P scattered waves, a subvertical reflector (red color, FAF in Figure 17) offset roughly 1 km toward the east of the surface (active) AF can be imaged. The dashed line gives the downward projection of the AF (Figure 17a). Resolution tests show that the accuracy of the location of the reflector (FAF) is ∼200 m in the E–W direction. Because of the configuration of source and receiver arrays the extent of this scatterer could not be resolved above 1 km and below 4 km depth and also not farther toward the south, thus not directly encompassing line 1 of the CSA I experiment and the NVR profile (Figure 2f). Integration of the results of this independent data set based on scattered seismic waves with the results of *Ritter et al.* [2003], *Maercklin et al.* [2005], *Ryberg et al.* [2007], and *Bedrosian et al.* [2007] suggests that the reflector imaged here is the northward extension of the western boundary of the high-velocity sliver of crystalline basement (Figures 14b and 15c, respectively).

[24] A detailed local 3-D density model covers an area of ∼30 × 30 km down to a depth of ∼5 km, partly shown in Figure 18. That model was computed from a newly compiled Bouguer gravity anomaly database corrected for effects of regional structures such as the Moho [*Götze et al.*, 2006]. The 3-D structural image of the upper crust reveals that the basement is vertically offset across the AF (Figures 18b–18d). It also shows an abrupt change in the physical parameters of the two lithological blocks, i.e., of the sediments in the west and the sliver of crystalline basement in the east. Analysis of the calculated gravity gradients (not shown) furthermore suggests that the AF could be offset at depth as shown in Figure 17. It should also be noted that such a shift in the location of the active transform was suggested by *Joffe and Garfunkel* [1987] to be the result of a shift of ≤5° in the local direction of plate motion which increased transtension some 5 Ma ago or somewhat earlier, whereas *ten Brink et al.* [1999a] suggested continuous small variations in plate motion as the cause of this shift. Note also that *Rotstein et al.* [1992] found evidence for a similar 2.5 km shift of the active fault trace in the area south of the Sea of Galilee.

[25] The 3-D image presented so far is also supported by the combination and interpretations of geology and seismic reflection studies (Figure 19) with multispectral (ASTER) satellite images (Figure 20) [*Kesten et al.*, 2008]. Such a combination allows us to analyze geologic structures in space and time since reflection seismics image deep faults possibly inactive at present, whereas satellite images reveal neotectonic activity in shallow young sediments.

[26] Starting in the west, we will now discuss distribution of slip along the central part of the NVR profile, i.e., of faults in the Arava/Araba Valley and its immediate vicinity. West of the AF, between profile kilometers 41 and 52, strong sedimentary reflections and indications of faults are visible in the NVR data (Figure 19c). Here, the Barak Fault and the ZF (Figures 19a and 20) are clearly imaged, as previously by *Bartov et al.* [1998] and *Frieslander* [2000]. Whereas the vertical offset at the Barak Fault seems to be minor, the Zofar Fault shows a vertical separation of ∼500 m and has been interpreted as a major fault in the northern Arava/Araba Valley, where it is the western border fault of the southern Dead Sea Basin [*Bartov et al.*, 1998; *Frieslander*, 2000]. On the basis of the general tectonic

Figure 13. (a–c) Three parallel vertical cross sections through the 3-D density model (for location of the profiles in Figures 13a–13c, see Figure 12). The distance between the cross sections is ∼60 km. The density of the various geologic units is given in Mg/m^3. The black circles indicate the Moho depth from the RFM (Figure 11a) [*Mohsen et al.*, 2005]. The black overlay is the NVR line drawing (Figure 11c), and the black lines indicate the interfaces of the seismic refraction model (Figure 10a). At the top of each section, the line of black dots indicates the modeled gravity, and the red line gives the measured gravity along the vertical cross section. Modified from *Götze et al.* [2006] with kind permission of Springer Science and Business Media.

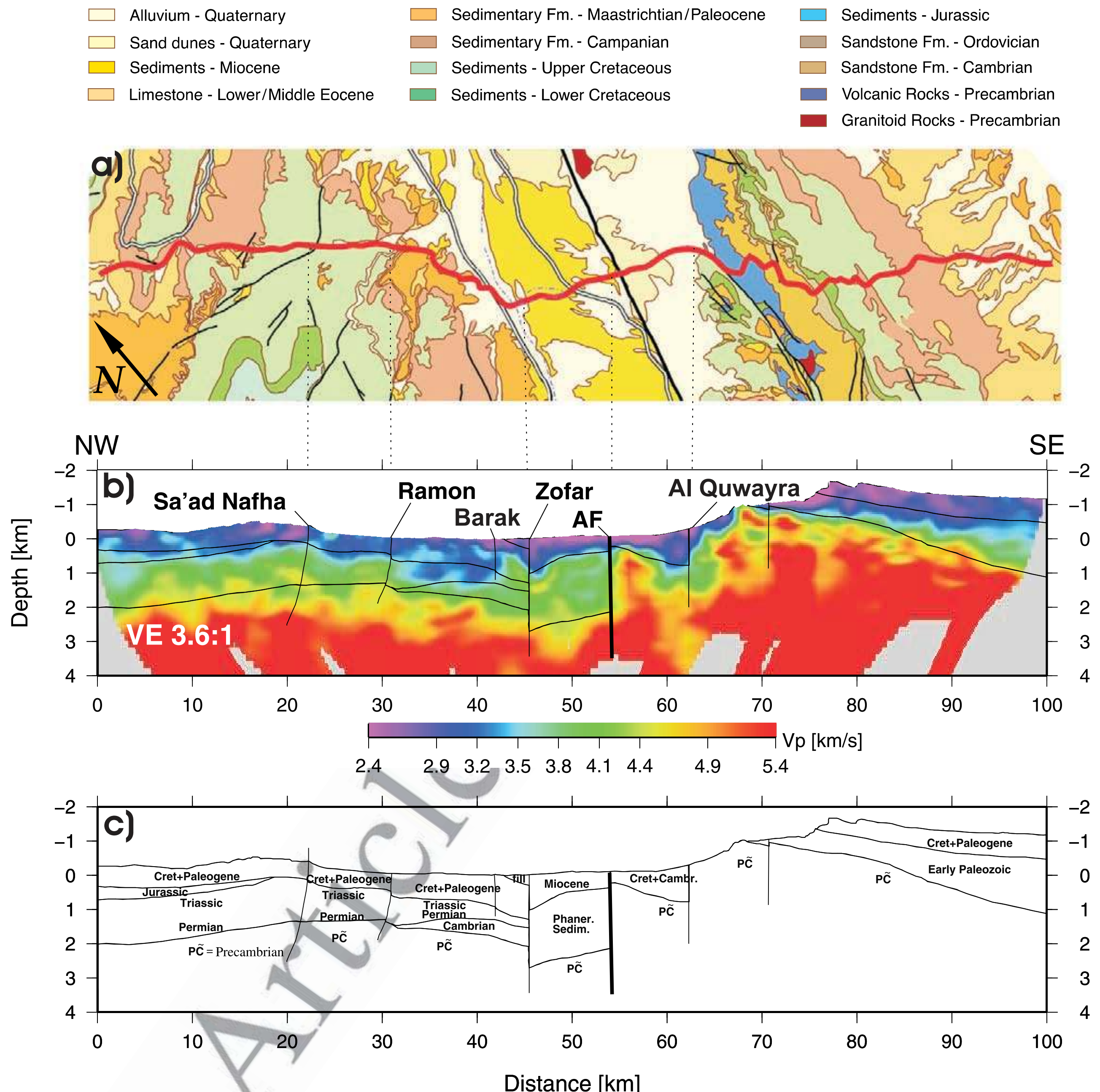

Figure 14. Geology, *P* velocity cross section, and geologic interpretation along the 100 km long NVR profile (white line in Figure 2b) centered on the AF. (a) Simplified geological map along the NVR profile (modified after *Sneh et al.* [1998] and *Bartov et al.* [1998]). The red line is the slightly smoothed reflection line of the NVR experiment. Six dominant faults (Sa'ad Nafha, Ramon, Barak, Zofar, AF, and Al Quwayra) are indicated by black lines (see also Figures 14b and 14c). Here the nomenclature of *Frieslander* [2000] and *Calvo and Bartov* [2001] is used. (b) Tomographic *P* velocity model along the NVR profile to a depth of 4 km using vibroseis and shot data [*Ryberg et al.*, 2007]. The vertical exaggeration is 3.6. The velocity model is characterized by strong horizontal gradients (e.g., at 20, 45, 55, and 62 km model distance, corresponding to the Sa'ad Nafha, Zofar, AF, and Al Quwayra faults, respectively). Several near-surface sedimentary basins (blue; low-velocity regions) bordered by faults can be seen. (c) Geologic cross section interpreted from the NVR profile and well data, to a depth of 4 km [after *DESERT Group*, 2004]. The vertical exaggeration is 3.6 as in Figure 14b. For more details of this area, see Figure 19 and *Kesten et al.* [2008]. Modified from *Ryberg et al.* [2007].

setting, a sinistral strike-slip component has been assumed, even if the total amount of lateral displacement is unknown (Z. Garfunkel, personal communication, 2008), but left-lateral strike-slip creep episodes along the ZF were indicated by InSAR data [*Finzi*, 2004]. An antithetic fault, east of the Zofar Fault at profile km 47 called "Eastern Fault" by *Frieslander* [2000], shows no surface expression and hardly any vertical displacement but is linked to the Zofar Fault at

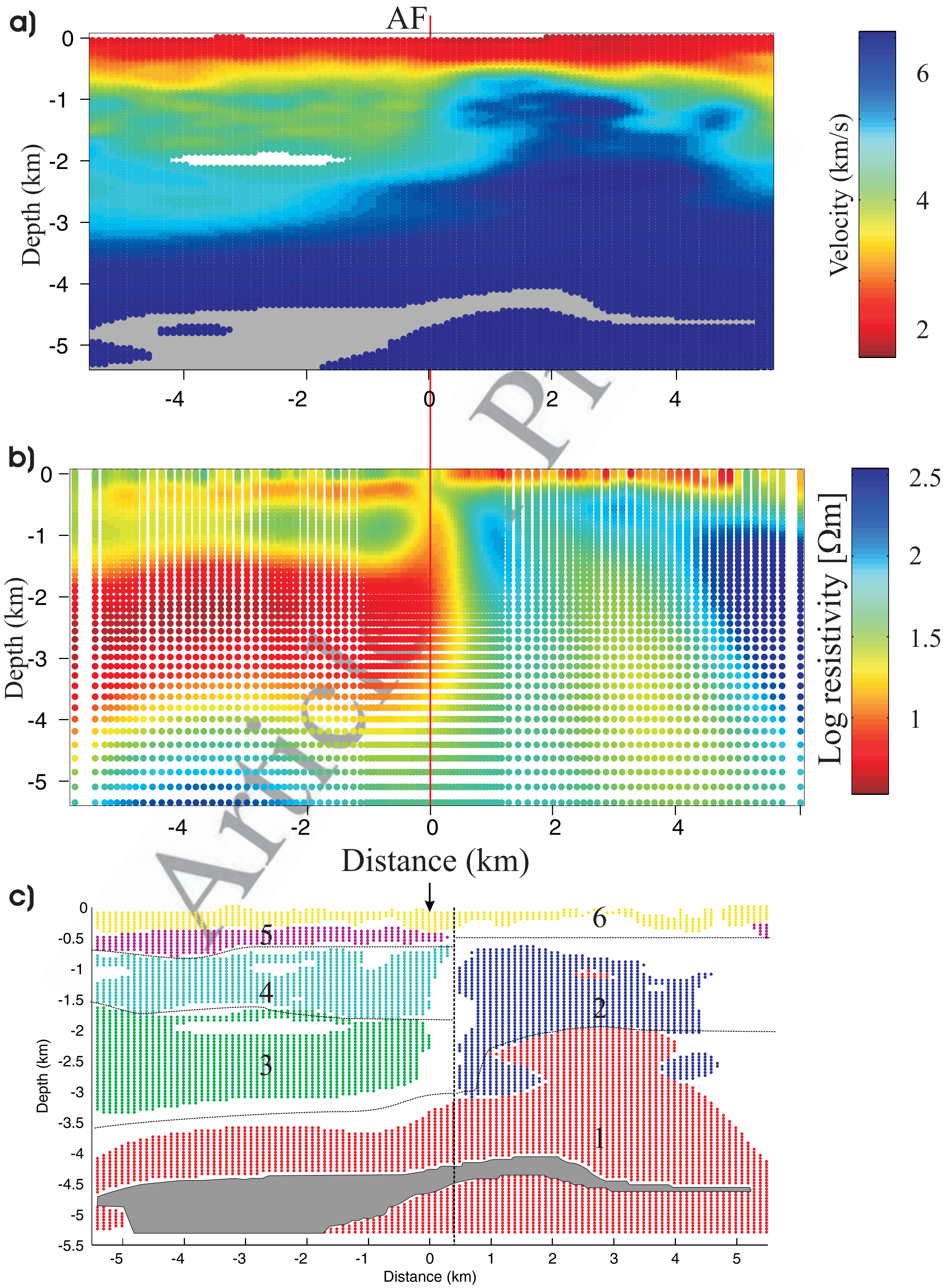
a)
AF
Depth (km)
0
-1
-2
-3
-4
-5
-4
-2
0
2
4
Velocity (km/s)
6
4
2
b)
Depth (km)
0
-1
-2
-3
-4
-5
-4
-2
0
2
4
Distance (km)
Log resistivity [Ωm]
2.5
2
1.5
1
c)
Depth (km)
0
-0.5
-1
-1.5
-2
-2.5
-3
-3.5
-4
-4.5
-5
-5.5
1
2
3
4
5
6
-5
-4
-3
-2
-1
0
1
2
3
4
5
Distance (km)

Figure 15

~2.5 km depth (Figure 19c). The fault at profile kilometer 49 does not seem to cut through the uppermost sediments and is not recognized at the surface. Thus, we assume it has not been active recently. There is, however, a marked contrast in reflectivity across this fault, indicative of previous strike-slip movement. The fault's near-vertical geometry corroborates this interpretation. A subsurface fault (Western Fault in Figures 2c and 19) is revealed ~4 km west of the AF in the industry reflection seismic profile VWJ-9 (Figure 19b) and the NVR profile (Figure 19c). Whereas seismic data in Figure 19b show flower structures typical for strike-slip faults, the satellite image does not reveal the Western Fault in post-Miocene sediments. Taking into account the age estimates from Table 2 and the fact that these sediments overlie the fault trace, the period of inactivity of the "old" strike-slip fault lies between 2 and 7 Ma. For a more detailed discussion, see *Kesten et al.* [2008]. The lack of coherent sedimentary reflections in the direct vicinity of the AF might result from intense brittle deformation of the rocks close to the fault but could also be caused by the absorption of high frequencies in this area covered by sand dunes and alluvium (Figure 19a). There is, however, a slight change in the character of (diffuse) reflectivity across the subsurface continuation of the AF (Figure 19c). Farther to the north (Figure 19b), there is strong indirect evidence of the AF in the seismic profile VWJ-9. Here the AF lies between a zone with strong sedimentary reflections to the west and a purely diffusely reflective upper crust toward the east. The AF itself is imaged as a nonreflective zone of ~800 m width at the surface, probably consisting of three branches (Figure 19b). The central one was also delineated by fault zone guided waves [*Haberland et al.*, 2003] and high-resolution reflection seismics and tomography to be discussed in section 2.4. Farther to the south of the study area, similar subparallel fault segments and flower structures related to the DST are also known from the Evrona playa site [e.g., *Shtivelman et al.*, 1998]. About 1 km east of the AF, another, now buried fault called FAF (Figures 2c and 2f) is detected, in agreement with the FAF scatterers in Figure 17 and the joint interpretation of seismic waves with magnetotellurics [*Ritter et al.*, 2003; *Maercklin et al.*, 2005; *Bedrosian et al.*, 2007]; see also Figure 14 for the vicinity of profile km 57. The AQF (Figures 19 and 20) [see also *Rabb'a*, 1991] is the most prominent fault in SW Jordan. This N–S running fault is more than 100 km long and extends into Saudi Arabia. In an outcrop of the AQF on the NVR profile the Upper Cretaceous sediments dip nearly vertically and show intense, subhorizontal slickensides, indicating sinistral movement. *Abu Taimeh* [1988] proposed a left-lateral displacement of 8 km for the AQF based on offset biotite muscovite aplite granites around latitude 30.3°N and on an 8 km long rhomb-shaped graben in this region. This argument seems to be supported by the geological map by *Bender* [1974] and *Ibrahim* [1991]. *Barjous* [1988], on the other hand, suggested an even larger horizontal slip in the range of ~40 km. His assumption is mainly founded on the southernmost outcrops of Precambrian rhyolites that occur ~40 km farther to the NE of the AQF. This higher value is also supported by stratigraphic observations (for details, see *Kesten et al.* [2008]). The distribution of slip on the faults in the vicinity of the AF, especially the AQF, led *Kesten et al.* [2008] to propose that the AF is clearly the main active fault segment of the southern DST. Despite this dominant role we postulate that the AF has accommodated only a limited part (at least 15 km and up to 60 km) of the overall 105 km of sinistral plate motion since the Miocene.

[27] In summary, integrating the results of these studies leads to the structural image of the crust in the vicinity of the AF given in Figure 3b. Only the integration and cross validation of several seismic methods (2-D and 3-D tomography, scattering mapping, and reflection seismics from controlled-source experiments), 2-D and 3-D MT experiments, 3-D gravity models, the analysis of multispectral satellite images, geology, and novel mathematical approaches (joint classification) allow the imaging of the 3-D structure under the AF on crustal to kilometer scale (Figure 3b). On the basis of these detailed studies of faults in the vicinity of the Arava/Araba Valley we suggest that at the beginning of transform motion deformation occurred in a ~20–30 km wide belt, possibly with the reactivation of older approximately north to south striking structures. Later, deformation became concentrated in the region of the present-day Arava/Araba Valley. Until ~5 Ma ago, there might have been other, now inactive faults in the vicinity of the present-day AF that took up lateral motion (FAF, Figures 2c and 3b). Together with a rearrangement of plates ~5 Ma ago, the main fault trace shifted then from the FAF to the position of today's AF.

2.4. Meter to Microscopic Scale

[28] In a high-resolution small-scale seismic experiment (CSA II, Figure 2f and *Haberland et al.* [2006]) the shallow structure of the (active) AF is analyzed down to a maximum depth of a few hundred meters. The experiment consists of

Figure 15. Lithological cross section derived from joint interpretation of magnetotelluric and seismic models along the seismic NVR profile (white line in Figure 2c) and the 10 km long magnetotelluric pilot profile (dark blue dots in Figure 2d). (a) *P* velocity model [*Ryberg et al.*, 2007]. The seismic model was calculated on a mesh of 10,000 cells. The gray and white areas denote regions where velocities cannot be constrained. (b) Resistivity model to 5 km depth [*Ritter et al.*, 2003]. The model was calculated on a mesh of 5136 cells. No vertical exaggeration is applied. The red line marks the surface trace of the AF. (c) Spatial distribution of lithological classes derived from an automatic class selection. Colors correspond to the classes enumerated in Table 1. The arrow marks the surface trace of the AF, and the thin black lines are our preferred structural interpretation. Gray region indicates missing model data. Modified from *Bedrosian et al.* [2007], copyright Blackwell Publishing.

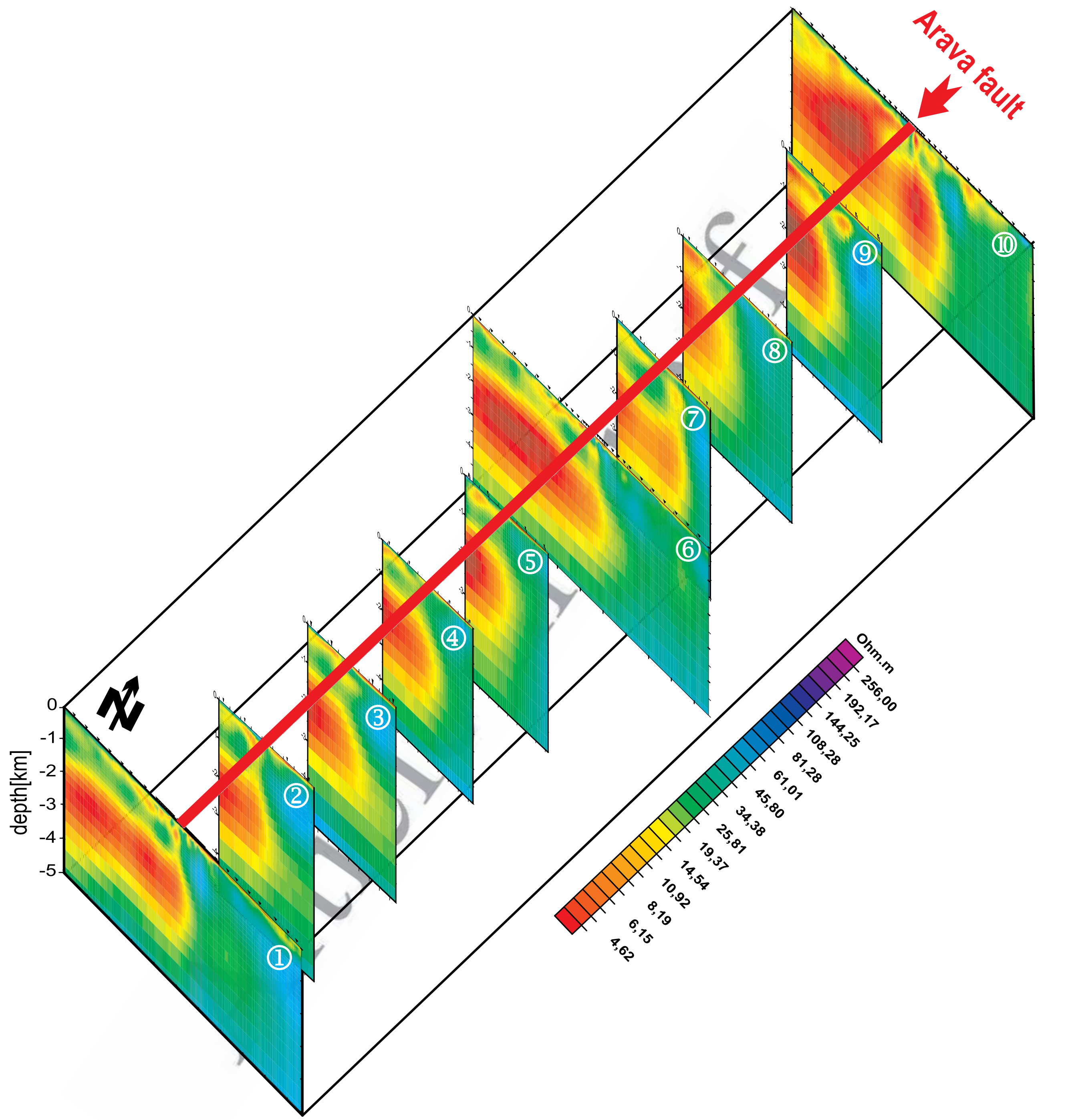

Figure 16. Three-dimensional electrical resistivity image around the AF (red line at top) in a 10 × 10 × 5 km box. The resistivity is given in Ω m, and red and yellow indicate good conductors. The resistivity distribution is derived from 2-D inversions of the three long profiles (10 km length, profiles 1, 6, and 10) and seven short profiles (5 km length, profiles 2, 3, 4, 5, 7, 8, and 9). Profile 1 is also shown in Figure 15b. The locations of the ten magnetotelluric profiles are given by dark blue dots in Figure 2d. The main anomaly is a good conductor from 1.5 to 4 km depth west of the AF, showing some variation in the north-south direction. This anomaly is most likely caused by saline fluids in a sedimentary layer, with the AF acting as a seal for cross-fault fluid flow toward the east [*Ritter et al.*, 2003; *Maercklin et al.*, 2005; *Bedrosian et al.*, 2007]. From south to north a shallowing of this brine layer can be observed. No vertical exaggeration. Modified from *Weckmann et al.* [2003].

eight subparallel 1 km long seismic lines. The combination of first break tomography and reflection seismic images (Figures 21a and 21b) shows a subvertical (main) fault separating two blocks with different seismic (physical) properties, positive flower structures, and, based on their seismic velocity, indications for different sedimentary layers on the two sides of the main fault. Often, the superficial sedimentary layers are bent upward close to the AF,

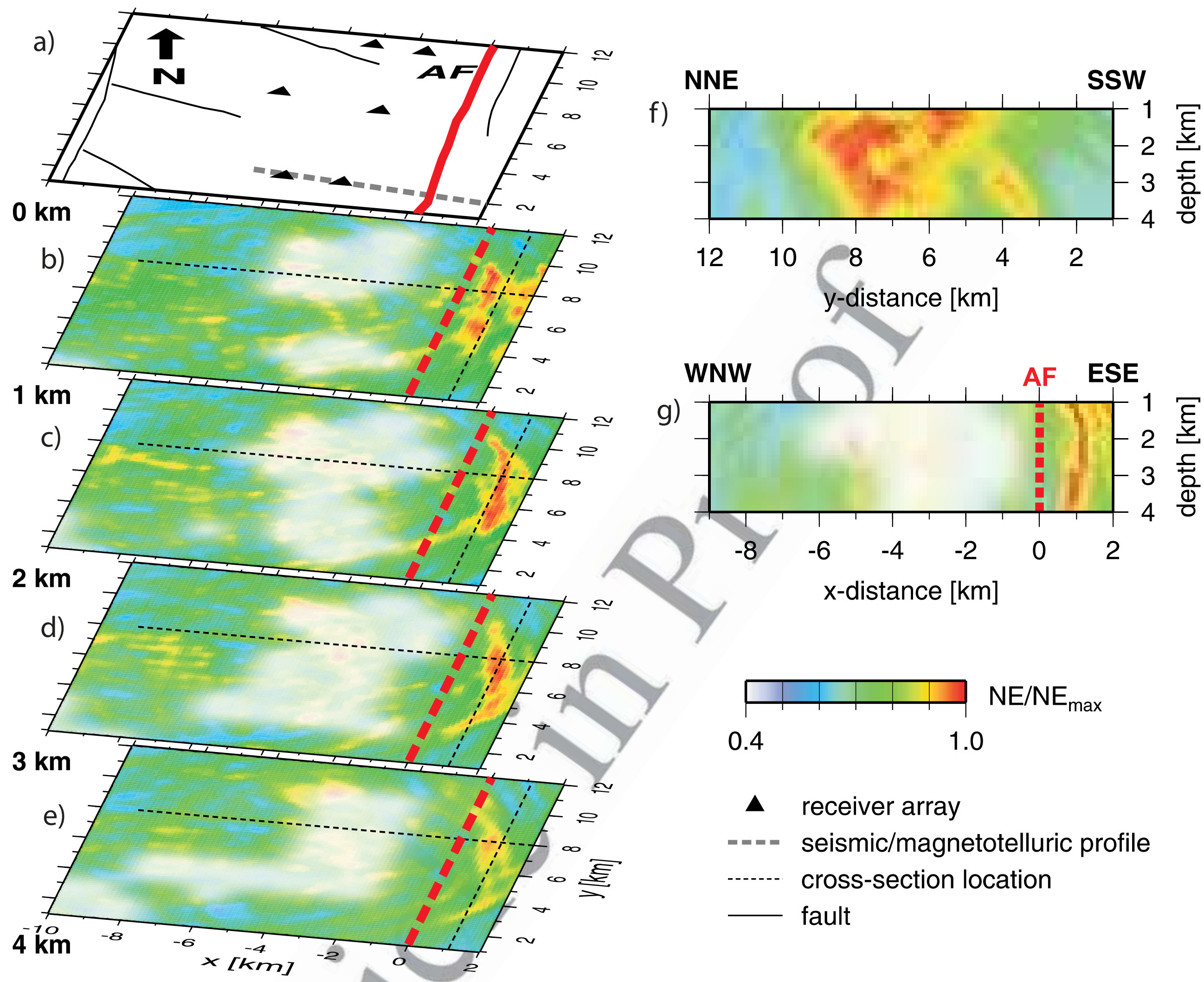

Figure 17. Color coded 3-D scatter image of the AF area in the central Arava/Araba valley. The model is derived from scattered seismic waves in the CSA I experiment. See Figure 2c: 3 × 10 km long profiles (thin black lines in Figure 2c); 9 miniarrays with 10 seismometers each (black triangles in Figure 2c); and 7 × 5, 4 × 3, and 3 × 2 shots (white stars in Figure 2c). Zones of strong scattering are in red. At these zones, high semblance values NE are observed; that is, these are the sources of secondary, scattered waves from the 53 shots located with the 9 miniarrays and the 3 profiles. For details of the method and the processing, see *Maercklin et al.* [2004]. Areas with poor resolution are whitened out. (a) A zoom of Figure 2c, with fault traces in black (except the AF, shown as a red line) and miniarrays (black triangles). (b–e) The four color-coded horizontal depth slices show the distribution of scatterers from 1 to 4 km depth, respectively. The downward projection of the AF is indicated by the dashed red line in each of the four depth slices. Note the 1 km offset of the scatterers (red) toward the east relative to the AF (dashed red line). Two vertical cross sections through the imaged volume at the two locations indicated by thin dashed black lines in the depth slices: (f) cut along the fossil AF (FAF) at x = 1.125 km running NNE to SSW and (g) cut across FAF at y = 8 km running WNW to ESE. The location of the AF at 0 km is indicated as a dashed red line. Modified from *Maercklin et al.* [2004], copyright Blackwell Publishing.

Figure 18. Selected cross sections of the 3-D density model of the central Arava/Araba Valley (see Figure 2e). (a) Study area and the residual gravity field in 10−5 m/s^2. The local survey gravity stations are marked by small black dots (green dots in Figure 2e). The 3-D density model consists of 13 cross sections (thin black oblique lines) with 1–3 km of separation. The position of the five seismic velocity cross sections from the 3-D seismic tomography model [*Maercklin*, 2004; *Maercklin et al.*, 2005] used to constrain the gravity modeling are marked by thick black lines (L1, L12, L2, L23, and L3). The AF (thick black line) and the ZF (thick dashed black line) are also indicated. Cross sections along (b) L3, (c) L2, and (d) L1, corresponding to lines 3, 2, and 1, respectively, in Figures 2c and 2f, of the 3-D gravity model with the corresponding density values in Mg/m^3. Above each density cross section the observed (red) and modeled (black) gravity anomalies in 10−5 m/s^2 are shown. The dashed lines are the velocity isolines of 3.5 km/s (top line), 4 km/s (middle line), and 4.5 km/s (bottom line) from the tomography model (P velocity cross sections) of *Maercklin et al.* [2005], shown below each panel. Distance and depth are in kilometers. Modified from *Tašárová et al.* [2006].

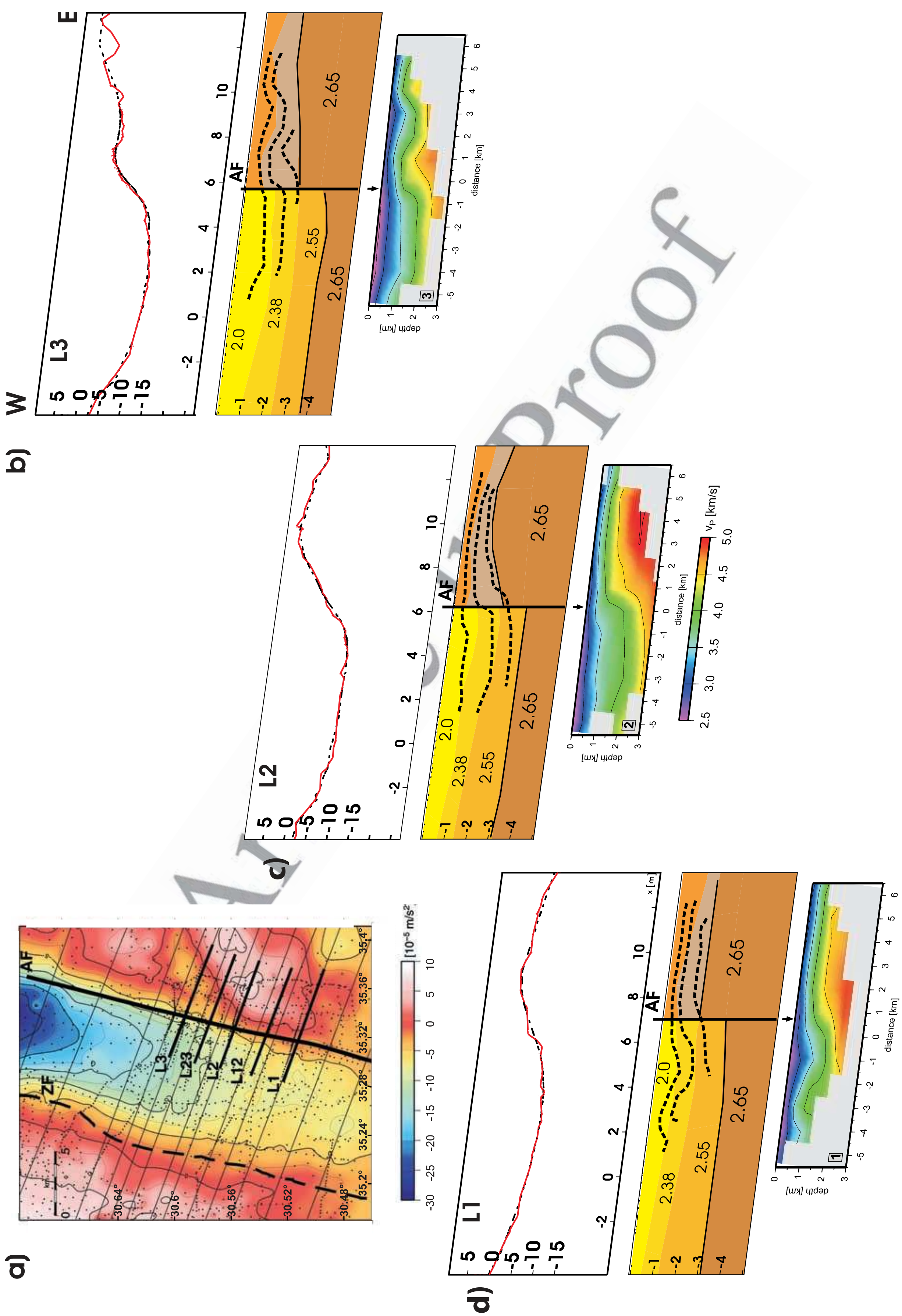
a)
b)
c)
d)
W
E
L1
L2
L3
L12
L23
AF
ZF
2.0
2.38
2.55
2.65
depth [km]
distance [km]
v_P [km/s]
$[10^{-5}$ m/s$^2]$
30.64°
30.6°
30.56°
30.52°
30.48°
35.2°
35.24°
35.28°
35.32°
35.36°
35.4°

Figure 18

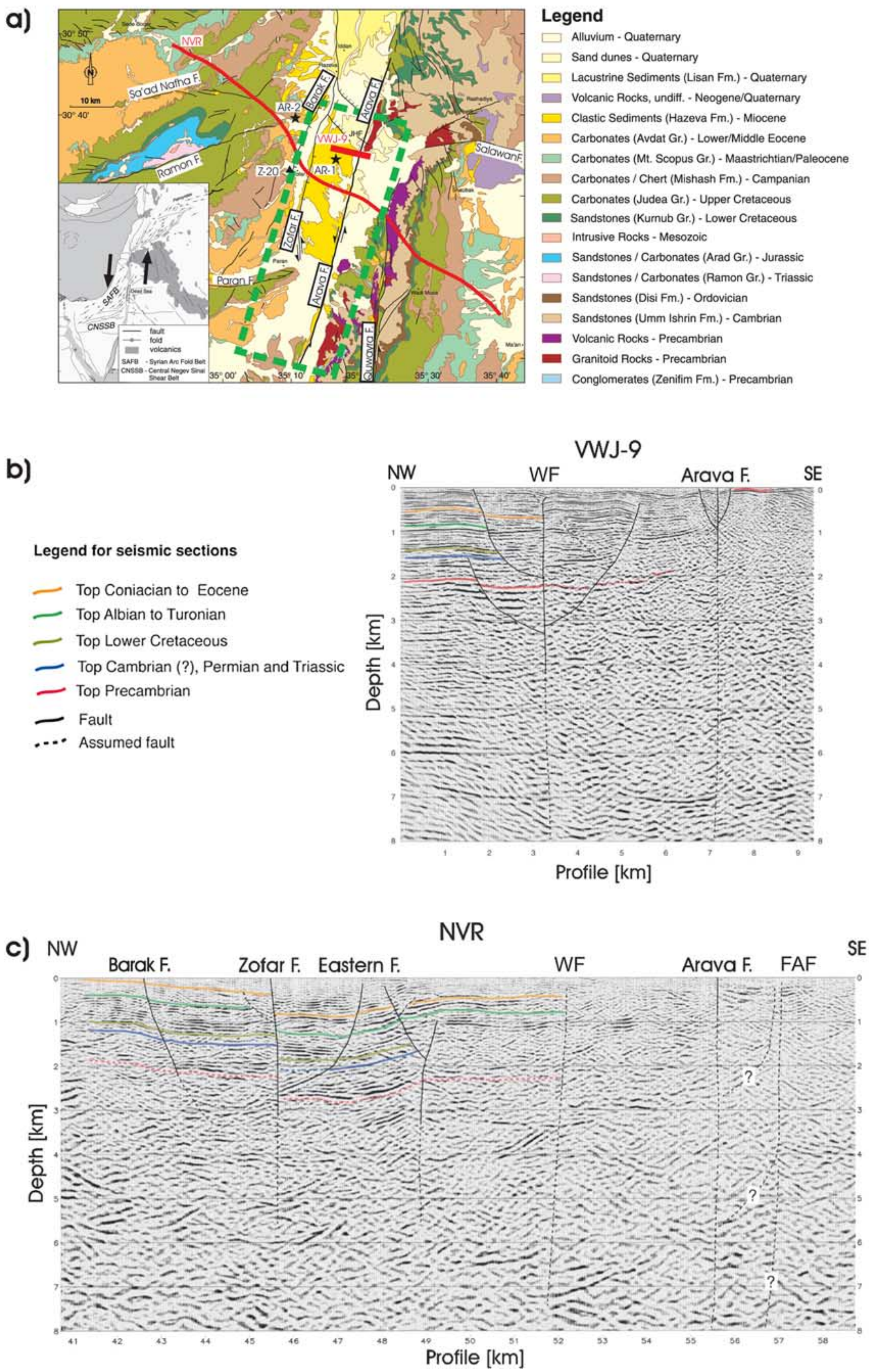
a)
Legend
Alluvium - Quaternary
Sand dunes - Quaternary
Lacustrine Sediments (Lisan Fm.) - Quaternary
Volcanic Rocks, undiff. - Neogene/Quaternary
Clastic Sediments (Hazeva Fm.) - Miocene
Carbonates (Avdat Gr.) - Lower/Middle Eocene
Carbonates (Mt. Scopus Gr.) - Maastrichtian/Paleocene
Carbonates / Chert (Mishash Fm.) - Campanian
Carbonates (Judea Gr.) - Upper Cretaceous
Sandstones (Kurnub Gr.) - Lower Cretaceous
Intrusive Rocks - Mesozoic
Sandstones / Carbonates (Arad Gr.) - Jurassic
Sandstones / Carbonates (Ramon Gr.) - Triassic
Sandstones (Disi Fm.) - Ordovician
Sandstones (Umm Ishrin Fm.) - Cambrian
Volcanic Rocks - Precambrian
Granitoid Rocks - Precambrian
Conglomerates (Zenifim Fm.) - Precambrian
NVR
Sa'ad Natha F.
Ramon F.
10 km
30° 50'
30° 40'
AR-2
AR-1
Z-20
VWJ-9
Barak F.
Arava F.
Zofar F.
Paran F.
Qurayqira F.
SalawanF.
SAFB
CNSSB
35° 00'
35° 10'
35° 30'
35° 40'
b)
Legend for seismic sections
Top Coniacian to Eocene
Top Albian to Turonian
Top Lower Cretaceous
Top Cambrian (?), Permian and Triassic
Top Precambrian
Fault
Assumed fault
VWJ-9
NW
WF
Arava F.
SE
Depth [km]
Profile [km]
c)
NVR
NW
Barak F.
Zofar F.
Eastern F.
WF
Arava F.
FAF
SE
Depth [km]
Profile [km]

Figure 19

indicating that this section of the fault (at shallow depths) is characterized by a transpressional regime [see, e.g., *Harding and Lowell*, 1979; *Lowell*, 1985]. To the north, these structures correspond to the transpressional elements at the surface (pressure ridges, see Figure 1c) caused by the local restraining eastward bend of the AF near Jebel Humrat Fidan (Figure 20a at 30.62°N). A 100–300 m wide heterogeneous zone of deformed and displaced material (Figures 21b and 21c) is detected which, however, is not characterized by low seismic velocities at a larger scale. Note that the shallow part of the DST in the southern Arava/Araba Valley is also several hundred meters wide [*ten Brink et al.*, 2007; *Shtivelman et al.*, 1998]. At depth below ~400 m, geophysical images indicate a blocked cross-fault structure (Figures 21d and 21e). The fault cores are not wider than ~10 m, in agreement with the study of fault zone guided waves from *Haberland et al.* [2003] indicated by black triangles in profiles P6, P7, and P8 (Figures 21c–21e). For a layout of that experiment, see Figures 2f and 2g. Such a narrow fault core is consistent with the up to 60 km displacement postulated for the AF [*Kesten et al.*, 2008]. Similar, wide (~1 km) flower structures related to the DST had been revealed within the sediments of the Evrona playa basin just north of the Gulf of Aqaba/Elat by high-resolution seismic studies [*Shtivelman et al.*, 1998]. In trenching analysis, *Niemi et al.* [2001] also found subparallel fault strands, pressure ridges, and comparable narrow fault zones at the AF zone ~50 km north of our study area. At a segment ~200 km farther to the north, the main faults of the DST are observed as wide zones of deformation rather than as distinct fault planes [*Rotstein et al.*, 1992].

[29] Geological and geochemical studies of carbonate fault rocks at the AF [*Janssen et al.*, 2004, 2005, 2007a, 2007b] document mesoscale to microscale faulting and veining in limestone at two locations (areas I and II in Figure 22) representing faulting at depths of 2–5 km and up to 3 km, respectively. The role of fluids in faulting deformation in the AF is locally quite different from that of other major fault zones, like, e.g., the SAF. At the AF, the small amount of veins and the lack of alteration and dissolution processes in limestone suggest reduced fluid-rock interactions and limited fluid flow within the fault. Note that on the kilometer to meter scale the AF acts as a barrier for fluids (see, e.g., Figure 15). Hydrothermal reactions (cementation and dissolution) did not affect the strength of the fault zone, indicating that the AF is a strong fault near the surface down to a few kilometers in the upper crust. Other segments of the AF show some iron mineralization, which might be related to an older fault system, known as the Central Negev-Sinai shear zone (CNSSB in Figure 19a (inset)) [see also *Frieslander*, 2000] or the Syrian Arc Fold Belt System (SAFB in Figure 19a (inset)) [see, e.g., *Bartov*, 1974; *Sneh et al.*, 1998; *Shamir et al.*, 2005]. In area I, where pressure ridges expose the exhumed fault and samples could be taken (red diamonds in Figure 2e), calcite mineralization reveals an open fluid system with fluids originating from two sources. Stable isotopes ($\delta^{13}C$ and $\delta^{18}O$) and trace elements indicate predominant infiltration of descending meteoric water, possibly supplied from the high eastern escarpment in Jordan [*Janssen et al.*, 2005]. This source is indicated by the good shallow electrical conductor east of the AF interpreted as a clay layer and possibly acting as caprock for meteoric water (near-surface red color east of the AF in Figure 22 (bottom); *Ritter et al.* [2003] and class 6 in Figure 15). This good conductor is also confirmed in the Short Offset Transient Electromagnetics experiments (blue profiles in Figure 2f; S. Helwig (personal communications, 2008)), showing that the subsurface groundwater flow is blocked at the AF. In area II (Figure 22, top right), geochemical data indicate only local (small-scale) fluid redistribution along profile B. These fluids were derived from the adjacent limestone under nearly closed system conditions [*Janssen et al.*, 2004].

2.5. Modeling and Interpretation

[30] Finite element 2.5-D thermomechanical modeling of the DST on plate tectonic to kilometer scale is used by *Sobolev et al.* [2005] to study the dynamics of this continental transform boundary between the Arabian and African plates. 2.5-D means calculation of all three components of the displacement (velocity) vectors under assumption of no changes in material properties, temperature, and velocity along the strike of the DST. The results of geological, geophysical, geothermal, and petrophysical observations, mostly from the DESERT project reported here, are used to constrain initial and boundary conditions and to choose the thermal and rheological parameters. The preferred model combines plate-scale transtension (strongly dominated by a strike-slip deformation component of 105 km) with thinning of the mantle lithosphere of the Arabian Shield at about 5–10 Ma and has a relatively weak crust [*Sobolev et al.*, 2005]. Figure 23 shows the setup of the thermomechanical model. In the initially cold lithosphere expected at the DST, shear deformation localizes in a 20–40 km wide zone (Figure 23) where the temperature-controlled mantle strength is minimal. The largest strain rates and finite strain are concentrated in the 5 km wide core of this zone. The

Figure 19. Geological map of the central Arava/Araba Valley and near-surface structure derived from seismic reflection data. Faults: BF, ZF, EF, WF, AF, and FAF. (a) Geological map (compiled after *Sneh et al.* [1998], *Bender* [1968], and *Frieslander* [2000]). The NVR and the VWJ-9 common depth point lines are given in red (white lines in Figure 2c). The green dashed box indicates the area of Figure 20a. Information on the stratigraphy can be found in Table 2. The inset shows information on some major tectonic elements in the Dead Sea region [after *Sneh et al.*, 1998]. Z-20, Zofar-20 well; AR-1 and AR-2, outcrops of Arava/Araba Formation; JHF, Jebel Humrat Fidan; CNSSB, Central Negev-Sinai shear zone; SAFB, Syrian Arc Fold Belt System. (b) Depth migrated shallow seismic reflection profile VWJ-9 [*Kesten*, 2004]. (c) Upper central part of the depth migrated NVR profile, where only the 18 km range in the green box in Figure 19a is shown (profile km 40.5–58.5). Modified from *Kesten et al.* [2008] with kind permission of Springer Science and Business Media.

resulting mechanically weak decoupling zone (20–40 km wide with the 5 km wide weakest core), controlled by shear heating and temperature and strain rate dependence of the viscosity, extends subvertically through the entire lithosphere. That is in general agreement with seismological, seismic, and magnetotelluric observations (Figures 6–9 and 3a), although important details remain unexplained (see discussion later in this section). Modeling furthermore

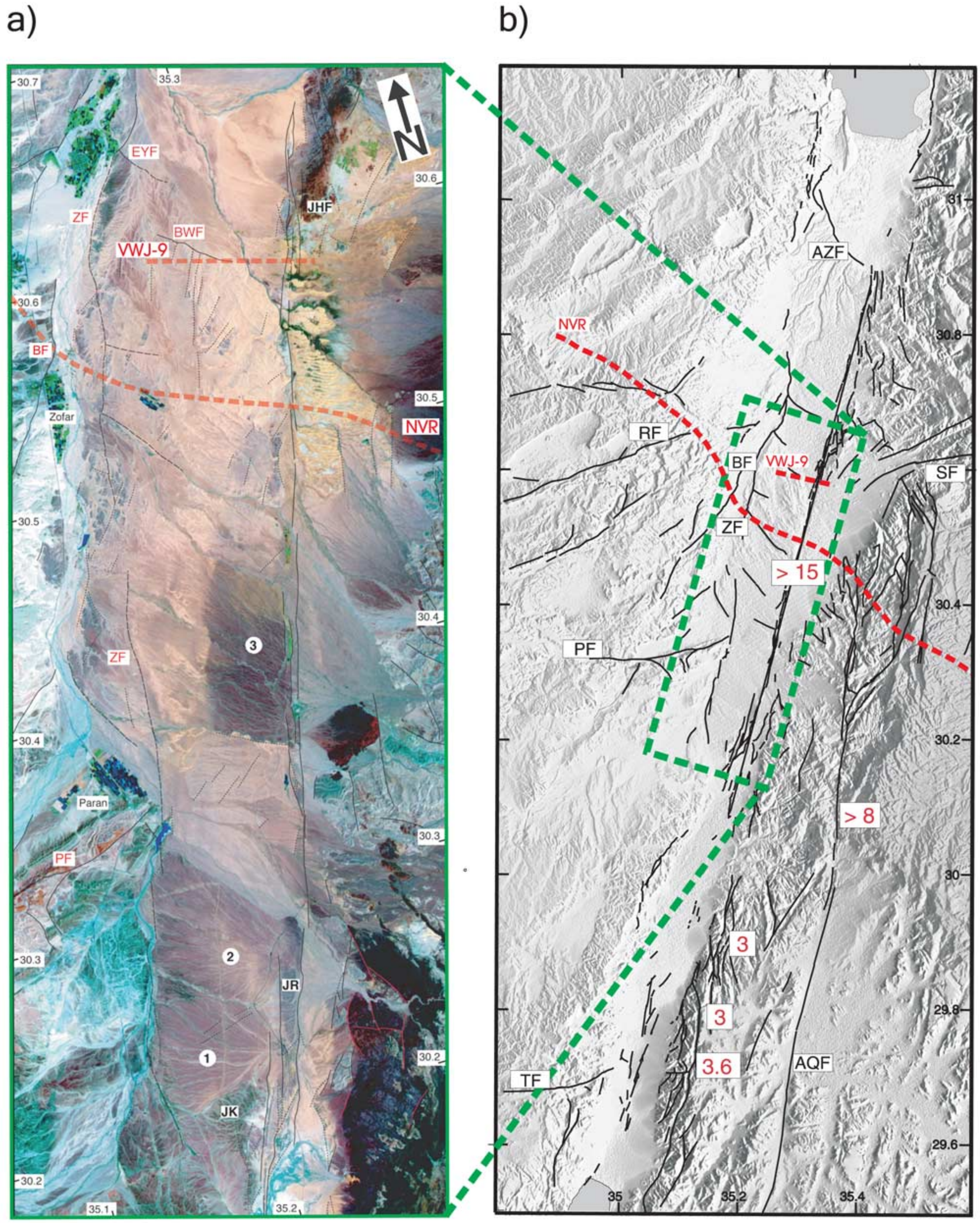

Figure 20

suggests that the location of the AF has been controlled by the minimum in lithospheric strength possibly associated with the margin of the Arabian Shield lithosphere and/or by the increased crustal thickness toward the east, also visible in seismic data [*Koulakov and Sobolev*, 2006; *DESERT Group*, 2004; *Mechie et al.*, 2005]. In the crust, one or two major faults take up most of the transform displacement, but a few kilometers of displacement occur also at several minor faults. These modeling results are consistent with geological and geophysical observations of several faults in the crust (Figures 14–20, 3a, and 3b) and the lithosphere structure imaged along the DESERT profile. The modeling also shows that less than 3 km of transform-perpendicular extension occur (Figure 24), suggesting that the AF segment of the DST is a dominantly strike-slip plate boundary. Note also the area of strong fault-parallel deformation in the lower crust (especially in the weak crust model (Figures 24d–24f)), which possibly is responsible for the LCR in Figure 11. We would furthermore like to point out that the hypothesis of the AF as a strong fault [*Janssen et al.*, 2004, 2005, 2007a, 2007b] holds only for the near-surface region but not for the crustal scale discussed here. Other geological, geophysical, and geodetic observations, like the slight asymmetric topography of the Moho, are also well reproduced. The uplift of the Arabian Shield adjacent to the DST requires young (<10 Ma) thinning of the lithosphere at of the plate boundary. Such lithospheric thinning is consistent with seismological observations and the high temperatures derived from mantle xenoliths in Neogene–Quaternary basalts [*Sobolev et al.*, 2005].

[31] An interesting question is the nature of the westward shift of the zone of higher seismic anisotropy and of the MT conductor relative to the surface trace of the DST, i.e., the AF. If both seismic anisotropy and conductor are associated with the locus of the shear deformation in the lower crust and lithospheric mantle as we suggest, then the present-day shear zones in the upper crust (AF) and in the deeper crust and mantle lithosphere (marked by the MT conductor and zone of seismic anisotropy) appear to be mutually shifted. Thermomechanical modeling [*Sobolev et al.*, 2005] demonstrates that such a shift is indeed possible (Figures 23c and 23f) because of heterogeneity of the lithospheric strength. However, the model suggests shift of the mantle shear zone to the east rather than to the west of the AF (Figure 23f). The most likely reason for such contradiction is that the model does not include the Dead Sea pull-apart basin which is located <100 km north of the DESERT line. If the mantle deformation zone is placed right beneath the Dead Sea basin and continues to the south parallel to the strike of the DST, as it is suggested by the numerical model of a pull-apart basin [*Petrunin and Sobolev*, 2006], then it must cross the DESERT line indeed west of the AF. Another possibility is that the AF at the DESERT line is a relatively young feature, and most of the strike-slip displacement is taken by other faults west of it, located above the zone of strongly anisotropic mantle. This idea is in line with seismic observation suggesting that the uppermost section of the AF is very narrow (10 m) but apparently contradicts geological observations [*Bartov et al.*, 1998].

[32] Finally, we would like to discuss how the DST modifies strength of the lithosphere, which it cuts through, on the basis of thermomechanical model and multidisciplinary observations. Various seismic observations presented in sections 2.2 and 2.3 indicate reduced seismic velocities and increased seismic anisotropy in the crust beneath the DST. This is likely due to the high crack density and indicates mechanical weakening of the crust, suggesting that the hypothesis of the AF as a strong fault [*Janssen et al.*, 2004, 2005, 2007a, 2007b] holds only for the near-surface region but not for the crustal scale discussed here. The thermomechanical modeling [*Sobolev et al.*, 2005] also suggests that major faults in the upper crust of the DST must be significantly weaker that the bulk of the crust. The model also infers that the zone of mechanical weakening continues deeper below the brittle-ductile transition and crosses the entire lithosphere (see distribution of viscosity in Figures 23d and 23g). There are at least two reasons why viscosity drops in the DST shear zone. One is the strain rate dependency of the viscosity related to the dislocation creep in lithospheric rocks, which leads to the reduction of the viscosity in the zone of the highest strain rate. Another reason is shear heating, which increases temperature in the shear zone. As a result of a number of processes also including fluid flow (recall MT conductor in the middle-deep crust), the lithospheric-scale shear zone appears to be a self-weakening body crossing the entire lithosphere.

3. DISCUSSION AND COMPARISON OF THE DEAD SEA TRANSFORM AND THE SAN ANDREAS FAULT

[33] The DST has a relatively slow present-day plate motion of ∼5 mm/a with a total displacement of 105 km in 20 Ma (up to 60 km of it along the AF). This puts the

Figure 20. Satellite image and fault map of the Arava/Araba Valley. (a) Advanced Spaceborne Thermal Emission and Reflection Radiometer (ASTER) scene of the central Arava/Araba Valley taken on 6 April 2001. Three types of lineaments can be distinguished: (1) Solid lines represent lineaments that are clearly recognized as faults (by displaced geological units, offset alluvial fans, or clear "doglegs" of streams); (2) dashed lines are lineaments that were identified as faults in other, mainly shallow seismic studies [e.g., *Frieslander*, 2000]; and (3) dotted lines are lineaments whose origin could not be clarified for lack of geological or geophysical information. EYF, En Yahav Fault; BWF, Buweirida Fault; PF, Paran Fault; JR, Jebel Er Risha; JK, Jebel El Khureij. Numbers 1–3 indicate alluvial fans. (b) Fault map of the southern DST, derived from the interpretation of ASTER satellite images [*Kesten*, 2004; *Kesten et al.*, 2008] over shaded relief map. The red numbers indicate the minimum amount of left-lateral strike-slip displacement along the respective faults in kilometers. AZF, Amaziahu Fault; RF, Ramon Fault; SF, Salawan Fault; TF, Themed Fault. Here the nomenclature of *Frieslander* [2000] and *Calvo and Bartov* [2001] is used. Modified from *Kesten et al.* [2008] with kind permission of Springer Science and Business Media.

TABLE 1. Resistivity (ρ), Seismic Velocity (Vp), and Thickness (t) of Classes Denoted in Figure 15c[a]

Class	ρ (Ωm)	Vp (km/s)	t (km)	Age	Lithology Type	Stratigraphic Unit
1	16–92	5.5 ± 0.3	1.5+	*l*PC	ark, cgl, volc	Zenifim formation (W); Aqaba complex: Ghuwayr volcanic, Araba complex (undifferentiated) (E)
2	26–173	4.8 ± 0.4	3+	*l*PC	cgl, qtz porph	Fidan granite, Araba complex: Ahaymir volcanic (E)
3	2–11	4.4 ± 0.5	1.6	C-K	sst, lst, dolm, mar, clst	Yam Suf, Negev, Ramon, Kurnub, Judea groups (W) ≈ 1.7 km
4	6–39	3.9 ± 0.3	1.0	*l*K-T	chk, cht, lst, mar	Mount Scopus, Avedat groups (W) (equivalent to Belqa group), 700 m
5	10–43	3.0 ± 0.3	0.5	Tm	sst, clst, cgl	Hazeva group (W) ≈ 500 m
6	11–39	2.2 ± 0.4	0.2	Tp-Qp	alluv: cgl, sd, slt, grv	Arava formation (W, E)

[a]Also included are inferred age (*l*PC, Late Precambrian; C-K, Cambrian-Cretaceous; *l*K-T, Late Cretaceous-Tertiary; Tm, Miocene; Tp-Qp, Pliocene-Pleistocene), lithology type (ark, arkose; cgl, conglomerates; volc, volcanic rocks; qtz, quartz; porph, igneous rocks; sst, silt stone; lst, limestone; dolm, dolomite; mar, marl; clst, clastic rocks; chk, chalk; cht, chert; alluv, alluvium; sd, sand; slt, silt; grv, gravel), and stratigraphic units. Classes spanning the Araba Fault are identified by geologic unit on both the west (W) and east (E) sides of the fault. Modified from *Bedrosian et al.* [2007].

DST in marked contrast to other major plate-bounding transform fault systems such as the NAF zone (presently 20 to 30 mm/a; 80 km in ~5 Ma) located amidst an orogenic belt [see, e.g., *Sengör*, 1979; *Barka*, 1992; *McClusky et al.*, 2000; *Hubert-Ferrari et al.*, 2002] and the dominantly transpressional SAF system (50 mm/a distributed among numerous faults from offshore to Colorado plateau; 300 km since 5–6 Ma) which originated from a complicated interaction between oceanic subplates and continental rocks [see, e.g., *Nicholson et al.*, 1994; *Holbrook et al.*, 1996; *Henstock et al.*, 1997; *Fuis*, 1998; *Atwater and Stock*, 1998; *Powell*, 1993; *Oskin et al.*, 2001; *Mooney et al.*, 2007; *Fuis et al.*, 2008]. A comparison of the characteristics of the DST and the SAF is given in Table 3. In contrast to the SAF the recent seismicity at the DST is moderate. As at the SAF, earthquakes are clustered in time at the DST, with large earthquakes occurring in a long cycle of several hundred to thousand years [*Marco et al.*, 1996; *Amit et al.*, 2002; *Marco et al.*, 2005], whereas the recurrence intervals at the SAF are typically 100–400 years [*Fumal et al.*, 2002] depending on the segment. *Lyakhovsky et al.* [2001] find that where the rate of healing is large compared to the rate of loading, the system exhibits short memory, and fault geometry evolves along several seismic cycles. The low rate of loading on the AF is compatible with such a system and with the distribution of the total slip across several strands, each active at a different time (see Figures 3, 9, 14, 15, 17, 19, 20, 23, and 24).

[34] In the subcrustal lithosphere the DST is a narrow 5–20 km wide anisotropic zone of (most likely) fault-parallel mineral alignment, suggesting subhorizontal fault-parallel mantle flow within a zone with distinct mineral alignment that extends through the entire lithosphere (Figures 6 and 9). The SAF also cuts through the crust [*Holbrook et al.*, 1996; *Henstock et al.*, 1997; *Unsworth et al.*, 2000; *Silver*, 1996; *Mooney et al.*, 2007; *Becken et al.*, 2008] and even the lithosphere [*Fuis et al.*, 2008], but estimates of the width of the fault-related seismically anisotropic zone below the crust range from 30 to 150 km [*Silver*, 1996; *Savage*, 1999]. This difference between the DST and the SAF could possibly indicate that the width of the decoupling zone scales with the total strain accumulated along the fault. One of the most likely main driving forces for the differences in strain and decoupling zones between the SAF and the DST is the difference in mantle thermal structure. While the DST originated in thick, cold lithosphere, which only recently may have been thinned to ~80 km [*Sobolev et al.*, 2005], the SAF has been generated in thin lithosphere underplated by hot mantle penetrating the opening slab window [e.g., *Dickinson and Snyder*, 1979; *Furlong et al.*, 1989; *ten Brink et al.*, 1999b; *Fuis et al.*, 2008; *Wilson et al.*, 2005].

[35] Both the DST and the SAF systems show a strong asymmetry in subhorizontal lower crustal reflectors (LCR in Figure 11) and a deep reaching narrow deformation zone of about 5 km width in the middle and lower crust (Figures 7 and 9 for the DST and *Holbrook et al.* [1996], *Silver* [1996], *Henstock et al.* [1997], *Mooney et al.* [2007], *Becken et al.* [2008], and *Fuis et al.* [2008] for the SAF). Whereas two large subvertical crustal conductivity zones are found in the Arava/Araba Valley and its vicinity (Figure 9), one SW

Figure 21. Tomographic and reflection seismic images of the top few hundred meters along a ~8 km long N–S segment of the (active) AF derived from the CSA II experiment (eight short white lines in Figure 2f, P1–P10, station spacing 5 m, and shot spacing of 20 m). (a) Tomographic inversion of the eight seismic lines. P wave velocities are in color (see scale at the bottom), and unresolved regions are masked (white). Depth range down to ~200 m. (b) Migrated reflection seismic sections down to ~500 m depth of all eight lines. Positive and negative amplitudes are shown as blue and red, respectively. (c) Migrated reflection seismic images (black wiggles) overlaid on the tomography (color) together with geological interpretation. Black thick lines indicate inferred faults, and dashed lines indicate less well constrained faults. M, S, and C indicate the main fault, secondary/flanking faults, and the sedimentary cover east and west, respectively. Inverted black triangles indicate the position of FZGW observations from *Haberland et al.* [2003]. The shots and receivers producing and recording FZGW are indicated in Figure 2g by red triangles and stars, respectively. (d) Summary of interpreted sections down to 500 m depth along a ~8 km long N–S segment of the AF based on Figures 21a–21c. The main fault is indicated by the red area. (e) Reconstruction of the fault structure based on seismic results. A few subparallel faults form the AF system in the study area; to the north the pressure ridge structure dominates. Modified from *Haberland et al.* [2006], copyright 2006, Elsevier.

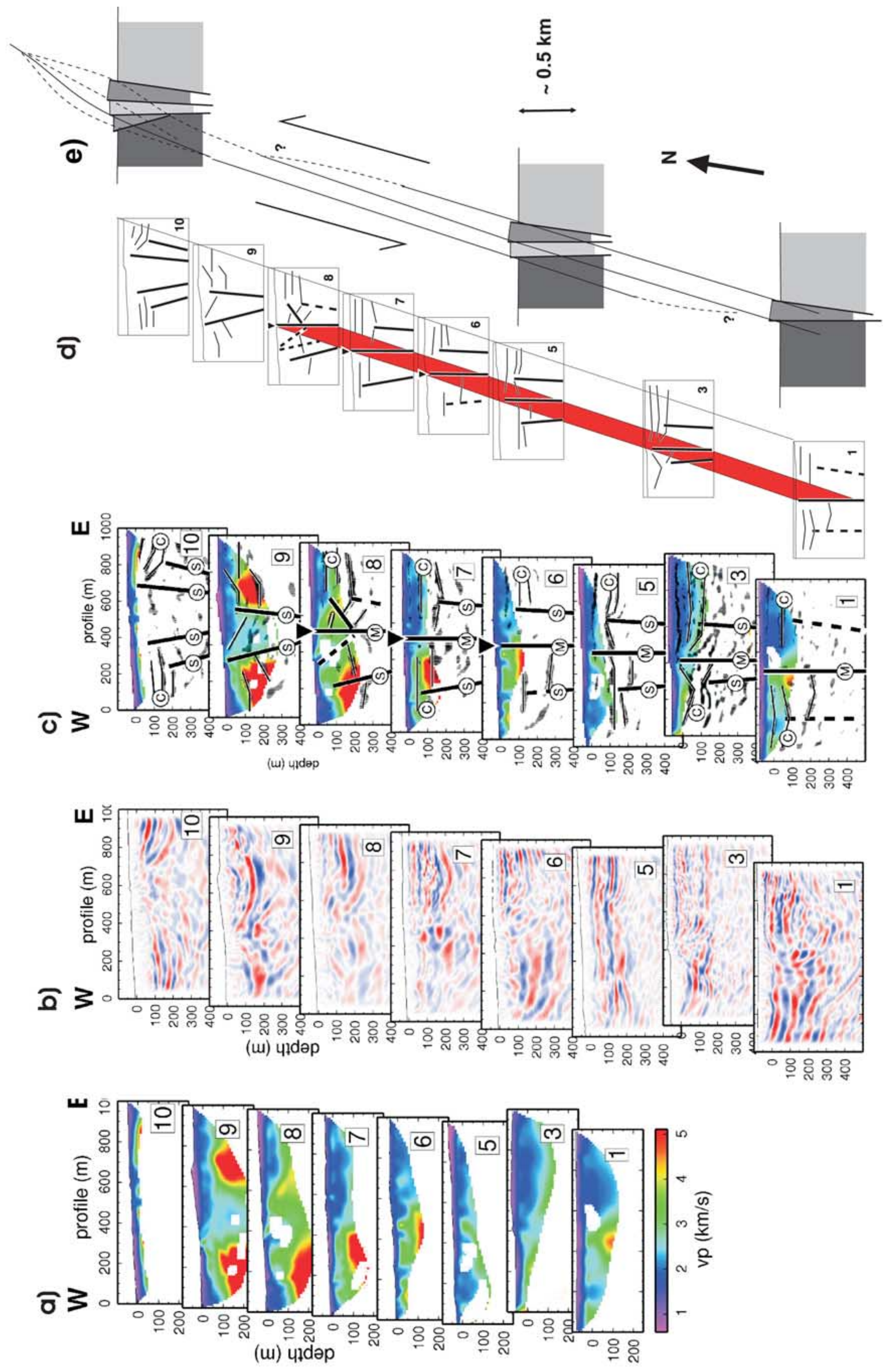

Figure 21

tilted crustal conductivity zone is found in the vicinity of the SAF at Parkfield [*Becken et al.*, 2008, Figure 14]. Such anomalies could be due to ascending fluids; see *Janssen et al.* [2005, 2007a] for the AF and *Wiersberg and Erzinger* [2007] for the SAF. At the SAF this conductive zone widens in the lower crust and seems connected to a broad conductivity anomaly in the upper mantle, but as stressed by *Becken et al.* [2008], the upper crustal branch of the inferred fluid conduit is located NE of the seismically defined SAF, suggesting that the SAF itself does not act as a major fluid pathway, at least not in the area near Parkfield. At the AF, only reduced rock interactions and limited fluid flow were

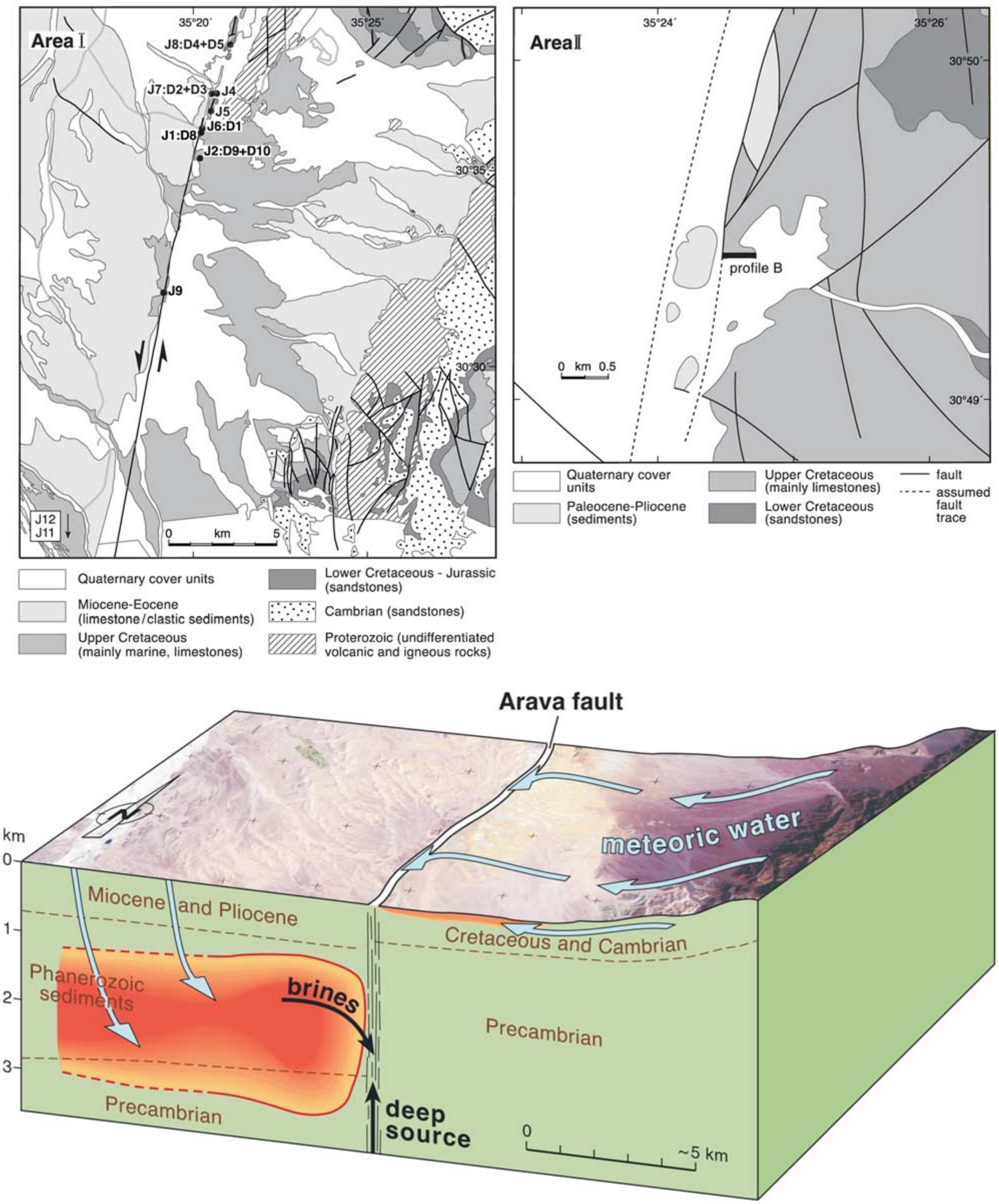

Figure 22

observed [*Janssen et al.*, 2005]. This leads us to conclude that neither the SAF (at least at Parkfield) nor the AF act as important fluid conduits, despite their strong signal in seismological and MT studies. We would also like to point out that the bright spot under the San Gabriel Mountains [*Ryberg and Fuis*, 1998] implies large fluid contents. As this feature is connected geometrically to the SAF in crust and mantle the SAF is interpreted as a fluid conduit there [*Fuis et al.*, 2001].

[36] In the uppermost crust the AF occurs as a barrier to fluid flow (Figures 9, 15, 16, and 3b) and not as a single, wide damage zone, a characteristic element of large, brittle fault zone structures [*Chester and Logan*, 1986; *Scholz*, 1987, 2000, 2002]. The SAF has multiple strands and is at ∼3 km depth a barrier to fluids, at least at SAFOD [*Unsworth et al.*, 1999, 2000; *Bedrosian et al.*, 2002; *Becken et al.*, 2008]. The West Fault in Chile [*Hoffmann-Rothe et al.*, 2004] also shows a pronounced fault zone conductor in the top 2–3 km. The central segment of the SAF near Parkfield is a location in transition between locked and creeping. Here the zone of high conductivity within the upper 2–3 km is attributed to fluids within a highly fractured damage zone [*Unsworth et al.*, 2000; *Ritter et al.*, 2005a]. The depth extent of the corresponding seismic low-velocity zone is ∼3 km, the base of which coincides with a cluster of small earthquakes. The width of this seismic low-velocity zone inferred from fault zone guided waves [*Li et al.*, 1990, 1997; *Mooney et al.*, 2007] is 100–700 m. Note also that at the NAF, *Ben-Zion and Sammis* [2003] found similar fault zone widths of ∼100 m. Possible reasons why no shallow, single, wide damage zone is observed at the AF could include the lower slip or reduced seismic activity along the AF in the last few hundred years. At the AF, strain may have been localized for a considerable time span along a narrow, meter-scale damage zone, with a sustained strength difference between the shear plane and the surrounding host rock. As a consequence, the existence or nonexistence of high electrical conductivity in the central part of large-scale strike-slip fault zones may be an indicator for the degree of strain localization during faulting [see also *Ritter et al.*, 2005a].

[37] In the top kilometer a network of (subparallel) individual faults characterized by narrow fault cores/damage zones is observed at the AF (Figures 21 and 3c). A narrow fault zone width of the main strand, between 5 and 20 m, was found by analysis of fault zone guided waves [*Haberland et al.*, 2003]. These narrow faults (black lines in Figure 21c) then form a broad heterogeneous zone of deformed and displaced material, which, however, is not characterized by low seismic velocities at a larger scale. On the other hand, throughgoing, subvertical low-velocity zones with a typical width of 100–300 m have been found at large shear zones such as the SAF and the NAF [see, e.g., *Li et al.*, 1997, 1998; *Ben-Zion and Sammis*, 2003; *Lewis et al.*, 2005]. A comparison of the few-meters-wide main strand of the AF with the thickness of gouge in laboratory experiments is consistent with corresponding total slip along the AF of 60 km [*Kesten et al.*, 2008]. The apparent distribution of deformation across several fault strands and the concentration of the deformation to individual narrow fault zones might be related to the low loading to healing ratio at the AF. The size of the damage zone is determined by a competition between localization and delocalization processes and thus depends strongly on the segment of the fault studied. The SAF zone does not heal completely on the time scale of the seismic cycle, and ruptures tend to repeat on the same smooth trend [*Stirling et al.*, 1996] and in very narrow zones [*Rockwell and Ben-Zion*, 2007].

[38] Structural and fluid properties of large fault systems vary in time and space [*Evans and Chester*, 1995; *Caine et al.*, 1996; *Evans et al.*, 1997; *Hoffmann-Rothe et al.*, 2004]. The internal structures of the Nojima fault zone (Japan) and the SAF are very similar, exhibiting a continuous meter-thick fault core containing foliated and nonfoliated ultra-cataclastites and alteration minerals surrounded by a wider zone of damaged host rocks [*Chester et al.*, 1993; *Ohtani et al.*, 2000]. Such a narrow fault core, composed of chemically altered rocks, was only observed in one outcrop at the DST, the Serghaya fault section in Syria, ∼500 km north of the study area [*Janssen et al.*, 2007a, 2007b], but not on the AF. In fluid properties, however, some similarities between the DST, the SAF, and the Nojima fault zone systems exist. Both the DST and SAF show significant variations in the intensity of fluid-rock interaction depending on fault segment. In all three fault systems, fluids originated from a variety of sources under different flow conditions, and geochemical results show that the fluids are predominantly of meteoric origin and migrated downward at shallow to moderate depths [*Kharaka et al.*, 1999; *Lin et al.*, 2001; *Pili et al.*, 2002; *Janssen et al.*, 2004, 2005, 2007a, 2007b].

Figure 22. Detailed geological maps of two locations at the AF and sketch of fluid flow at the AF. (top left) Geological map of the Fidan region (area I) slightly modified from *Rabb'a* [1991] with locations of mesostructural and microstructural analysis indicated by black dots with labels (J, location number; D, sample number from *Janssen et al.* [2004]). These locations are also indicated by red diamonds in Figure 2e. (top right) Geological map of the Fifa region (area II in Figure 2b, slightly modified from *Tarawneh* [1992]). (bottom) Sketch of the fluid movement at the AF (area I, Figure 22 (top left)) illustrating fluid infiltration from different sources. Geological units are from Figure 14c [*DESERT Group*, 2004]. Red and yellow areas are regions of high electrical conductivity, indicative of (saline) fluids [*Ritter et al.*, 2003; *Maercklin et al.*, 2005; *Bedrosian et al.*, 2007; *Weckmann et al.*, 2003] (see also Figures 15 and 16). Meteoric water (the red near-surface conductor east of the AF) is supplied from the high eastern escarpment in Jordan. Rare earth element and Sr isotopes analysis also suggest minor involvement of fluids from a deep source that ascend through the AF. Modified from *Janssen et al.* [2004] (copyright 2004 by the University of Chicago) and *Janssen et al.* [2005] (with kind permission of Springer Science and Business Media).

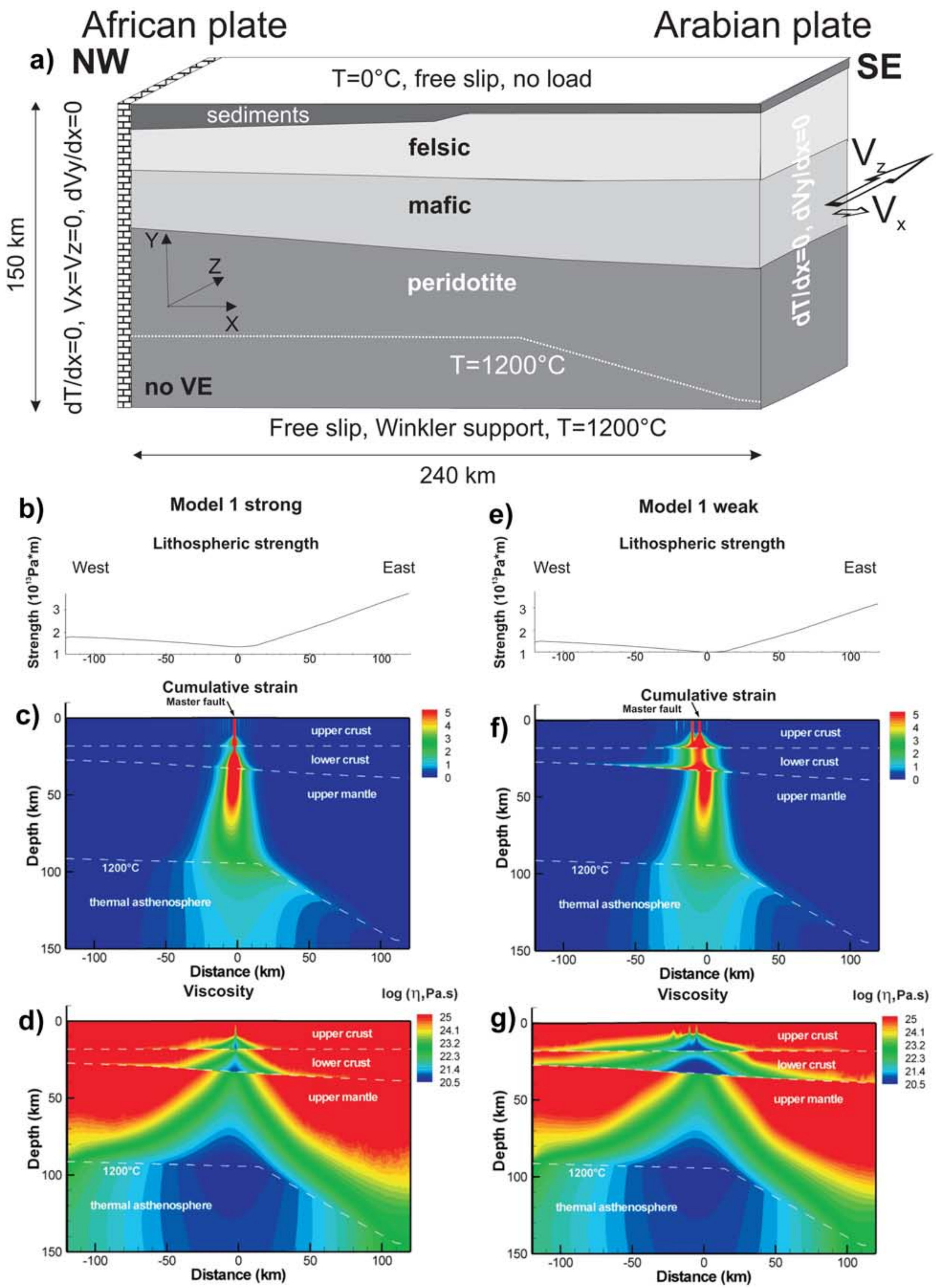
African plate
Arabian plate
a) NW
SE
T=0°C, free slip, no load
sediments
felsic
mafic
peridotite
T=1200°C
no VE
150 km
dT/dx=0, Vx=Vz=0, dVy/dx=0
dT/dx=0, dVy/dx=0
Free slip, Winkler support, T=1200°C
240 km
b)
Model 1 strong
Lithospheric strength
West
East
Strength (10^13 Pa*m)
c)
Cumulative strain
Master fault
upper crust
lower crust
upper mantle
1200°C
thermal asthenosphere
Depth (km)
Distance (km)
d)
Viscosity
log (η,Pa.s)
e)
Model 1 weak
f)
g)

Figure 23

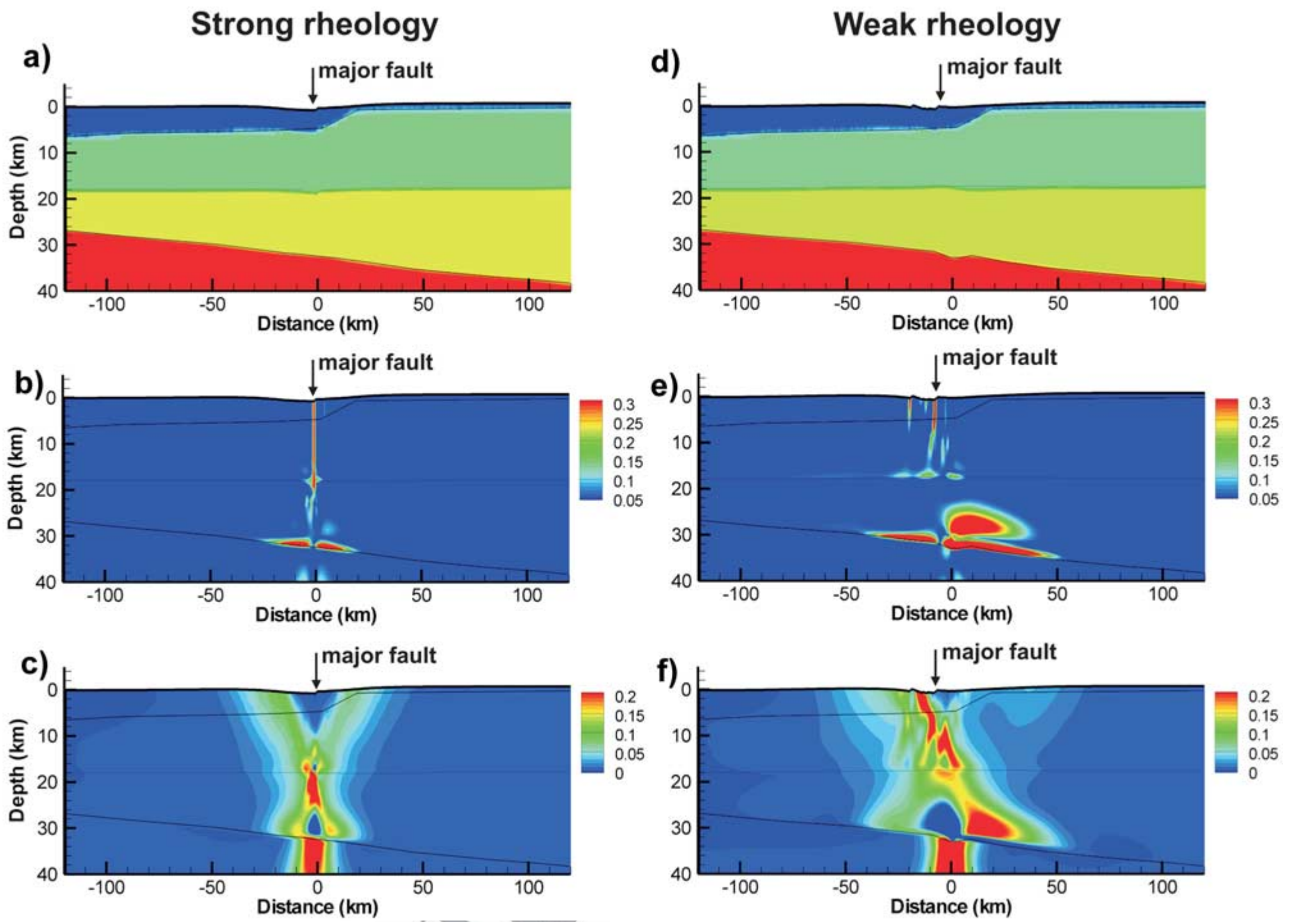

Figure 24. Distribution of crustal structure, shear strain, and extension at t = 17 Ma in the strong and weak crust models shown in Figure 23. Additionally, the lithosphere was thinned at t = 12 Ma; that is, the mantle lithosphere was then replaced by the asthenosphere with a temperature of 1200°C, and a few kilometers of transform-perpendicular (east-west) extension were added. For details, see *Sobolev et al.* [2005]. (a–c) Model with strong crust. (d–f) Model with weak crust. Figures 24a and 24d show crustal structure. Note the occurrence of Moho flexure in the weak-crust model (Figure 24d). Figures 24b and 24e show distributions of absolute values of shear strain $|e_{12}|$ (horizontal shear at horizontal plane or vertical shear at vertical plane). Note intensive shear deformation in the lower crust in the weak crust (Figure 24e) and its absence in the strong crust (Figure 24b). Figures 24c and 24f show distributions of transform-perpendicular extension (e_{11} component of the finite strain tensor). Note asymmetric deformation in the weak crust (Figure 24f). The vertical exaggeration is 2. Modified from *Sobolev et al.* [2005], copyright 2005, Elsevier.

Besides meteoric fluids, infiltration of brines is observed in all three faults. Upward fluid migration is found at the SAF (mantle fluids [*Kennedy et al.*, 1997; *Wiersberg and Erzinger*, 2007]) and to a minor extent at the DST (hydrothermal fluids from crystalline basement in area II [*Janssen et al.*, 2005]). However, as pointed out previously in this section, the geochemical and geophysical studies of *Wiersberg and Erzinger* [2007] and *Becken et al.* [2008] indicate that mantle fluids seem to migrate through the northeastern fault block of the SAF on the North American Plate, while the seismically defined SAF is not very permeable in the vertical direction. In addition to fluid migration under open system conditions, local fluid redistribution under closed conditions is found at the DST and

Figure 23. Setup of thermomechanical models with two pure strike slip models and strong and weak crust, respectively. Lithospheric strength, cumulative finite strain, and viscosity are shown. (a) General model setup with boundary conditions and lithospheric structure. Results for pure strike-slip models of cold and thick lithosphere with (b–d) a strong crust and (e–g) a weak crust. Figures 23b and 23e show lithospheric strength prior to deformation (t = 0 Ma) on a W–E profile. Figures 23c and 23f show the distribution of the cumulative finite strain (square root of the second invariant of the finite strain tensor) at t = 17 Ma, corresponding to present conditions. Thin white lines indicate major lithospheric boundaries from *DESERT Group* [2004] and *Mechie et al.* [2005]. Figures 23d and 23g present the distribution of viscosity at t = 17 Ma. No vertical exaggeration. Modified from *Sobolev et al.* [2005], copyright 2005, Elsevier.

TABLE 2. Miocene to Recent Stratigraphic Units in Northern Arava/Araba[a]

Age	Stratigraphic Unit	Absolute Age (Based on)
Pleistocene to recent	Zehiha formation/Lisan formation, alluvium, sand dunes, playa deposits	1.5–0.5 Ma (basalt flows, Jordan)
Pliocene	Arava formation/Mazar formation	3.7–1.7 Ma (basalt flows, Jordan), 6 Ma (En Yahav dike, Israel, and basalt flows, Jordan)
Miocene	Hazeva formation/Dana conglomerate	19–21 Ma (dolerite dikes, Karak)
Eocene	Avedat group/Um Rijam Chert-Limestone formation	

[a]After *Sneh et al.* [1998] and *Avni et al.* [2001]. Age dating after *Steinitz and Bartov* [1991].

the SAF [*Evans and Chester*, 1995], but it has to be pointed out again that the SAF (at Parkfield) and the AF do not act as important conduits for deep fluids.

[39] The principal difference in the geodynamic evolution of the DST and SAF is that the SAF is evolving within a thin lithosphere and in a system with a highly variable thermal state. During the northward migration of the Mendocino triple junction along the Pacific–North America plate boundary, the slab being subducted beneath it was replaced by hot asthenospheric material in a slab window or slab gap [e.g., *Dickinson and Snyder*, 1979; *Furlong et al.*, 1989; *Wilson et al.*, 2005]. The transform deformation along the northern part of the plate boundary thus developed simultaneously with thermal reequilibration of the lithosphere. Along the southernmost part of the transform, active rifting with high heat flow is occurring. Along the central SAF, older rocks are offset and heat flow is moderate [*Lachenbruch and Sass*, 1980] (see also Table 3). Another key difference between the DST and SAF systems is that the North American lithosphere must have been affected by the passage of the Mendocino triple junction below it [*Goes et al.*, 1997; *Furlong and Govers*, 1999]. This makes the geodynamic situation at the SAF strongly three-dimensional, since right-lateral shear is accommodated at the SAF, but compressional deformation occurs over a much wider belt, basically across the entire Coast and Transverse Range province. In contrast to the SAF, at the AF, strike-parallel changes in lithospheric structure can be ignored in a first-order approximation [*Sobolev et al.*, 2005].

4. CONCLUSIONS AND OUTLOOK

[40] On the basis of the multidisciplinary approach presented here, we find that the main characteristics identified for the Arava/Araba Fault (AF) segment of the DST are as follows: (1) a narrow, subvertical zone cutting through the entire crust, extending into the lithosphere, where the fault zone width ranges between 20 and 30 km; (2) a Moho depth that smoothly increases from 26 to 39 km from NE to SW; (3) a subhorizontal lower crustal reflector east of the AF; (4) the existence of several large faults in the upper crust in the vicinity of the AF, none of which has a large zone of decreased seismic velocities/high conductivity typical for damage zones; (5) that the AF acts as a barrier to fluids and

TABLE 3. Comparison of Several Characteristics of the Dead Sea Transform and the San Andreas Fault[a]

Characteristic	DST	SAF
Age of onset	≈20 Ma	28 Ma
Total offset of main FZ	105 km	480 km (1000 km if distributed shear east to Colorado Plateau allowed)
Offset in last 5–6 Ma	≈60 km	≈300 km
Present displacement rate	≈5 mm/a	35 mm/a in northern/central CA and a few mm/a convergence, 30 mm/a in southern CA and 10 mm/a convergence
Current thickness of lithosphere	≈80 km	≈30 km in northern CA (crust only), 35+ km in southern CA
Quake size	≈*M*7.5	*M*8
Quake frequency	100–1000 years	100–400 years
Number of faults currently active	1–2	3–4 depending on segment
Number of inactive faults in FZ	3–4	3–4+
Thickness of fault core, active fault	5–20 m	100+ m
Fluid involvement/barriers and fault manifestation at depths	0–1 km: shallow fluid layers separated by barrier	3 km: gas and fluid barrier at SAFOD
	1–4 km: west of AF, brine body stops at fossil AF	30+ km: interpreted fluid channel east of SAF at SAFOD, dips steeply west
	10–50+ km: vertical FZ ≈ 10 km west of AF	15–20 km: subhorizontal fluid-rich layer connecting to SAF (southern CA)
	5–30 km: AQF dipping east	
Heat flow	low to moderate	high at north and south ends, moderate in center

[a]DST, Dead Sea Transform; SAF, San Andreas Fault; FZ, fault zone; AF, Arava/Araba Fault; AQF, Al Quwayra Fault; SAFOD, San Andreas Fault Observatory at depth. See also Figure 3.

abrupt changes in lithology across the AF occur down to a depth of 4 km; (6) ongoing tectonic activity in shallow sediments in at least two AF strands (fossil and active AF); (7) a damage zone of individual faults with widths of only 5–20 m; and (8) a mainly meteoric origin of fluids in the AF. As pointed out in more detail at the end of each section, these eight features (see Figure 3 for a representation at different scales) could not have been identified reliably if only one (geophysical) method had been used. Only an interdisciplinary approach integrating findings from seismology, seismics, electromagnetics, gravity, geothermics, petrology, geochemistry, and field mapping based on surface geology, multispectral satellite images, and remote sensing gives sufficient independent confirmation, which then is tested by thermomechanical modeling. Considering the dynamics of the DST we find that deformation began in a 20–40 km wide zone, which later became concentrated in one or two major faults in today's Arava/Araba Valley. Until ~5 Ma ago, other, now inactive fault traces in the vicinity of the present-day AF took up lateral motion. Then, together with a rearrangement of plates, the main fault trace shifted to its present position. The AF is the main active fault of the DST system, but it has only accommodated up to 60 km of the overall plate motion. The AF is a system of almost pure strike-slip faulting and the shear deformation is controlled by the location of minimum mantle strength, which produced the subvertically mechanically weak decoupling zone extending through the entire lithosphere.

[41] A comparison of the AF with the SAF and other large faults shows that the width of the AF is significantly smaller than that of other major faults, most likely because of less total slip on the AF (up to 60 km). The narrow damage zone at the AF could be the result of a faulting mechanism where strain is extremely localized. Prominent similarities between the DST and the SAF, on the other hand, are that both have an asymmetry in subhorizontal lower crustal reflectors and deep reaching deformation zones and show flower structures in transpressional regimes at local scale. Such features are most likely fundamental characteristics of large transform plate boundaries.

[42] Large transform faults represent varying structure and dynamics in both time and space. However, a number of common features can be detected. The dominant mechanisms for the development and occurrence of large fault systems are as follows: (1) the large-scale forces acting on the plates and their transfer into the contact area between the plates, where the faults then develop; (2) the previous history and the geochemical, thermal, and petrological fabrics inherited during geological time in the contact area of the plates; and (3) the local hydrological and geological setting controlling the strength of the fault(s) as they develop in time. The dependence of the development of faults on such a large range of spatial and temporal scales, their specific inherited structures, and the limited number of large faults studied in detail up to now makes it nontrivial to isolate fundamental and characteristic features of large transform faults. The only way to gain a better understanding of the controlling forces and settings that determine how faults come into being, evolve, and become inactive is the multidisciplinary study of more active and fossil faults. Of special interest for future studies is also how more complicated 3-D structures like deep sedimentary basins/pull-apart basins (e.g., the Dead Sea Basin) evolve along large faults. This is the topic of an ongoing study.

[43] **ACKNOWLEDGMENTS.** The work presented here by the Dead Sea Rift Transect (DESERT) Group was supported by the Deutsche Forschungsgemeinschaft (DFG), the GeoForschungs-Zentrum Potsdam (GFZ), and the Alexander von Humboldt Foundation. N. Kukowski and G. Fuis provided constructive reviews of an earlier version of this manuscript, though their views do not necessarily agree with those presented here. We thank the editor M. Manga, the reviewers W. Mooney and T. Stern, and an anonymous reviewer for comments on an earlier version of this manuscript and A. Siebert for her help in drafting Figures 1, 2, 4, 11, 14, 17, 19, 20, and 21, most of them created with the GMT software [*Wessel and Smith*, 1998]. We thank the National Ministry of Infrastructure of Israel, the Natural Resources Authority of Jordan, and the An-Najah National University in Nablus, Palestine, for their support during the field work. We thank our contractors the Geophysical Institute of Israel, the Site Group (Jordan), and the Chemical and Mining Industries (Jordan) for their excellent work under difficult logistic conditions. The instruments for the field work were provided by the Geophysical Instrument Pool of the GFZ. The experiments were funded by the DFG, the GFZ, and the Minerva Dead Sea Research Centre. For more information on DESERT and the Dead Sea Integrated Research Project (DESIRE), its successor, see http://www.gfz-potsdam.de/portal/-?$part=CmsPart&docId=2434369 (DESERT) and http://www.gfz-potsdam.de/portal/-?$part=CmsPart&docId=2266356 (DESIRE).

[44] The Editor responsible for this paper was Michael Manga. He thanks Walter Mooney and Timothy Stern as technical reviewers and one anonymous cross-disciplinary reviewer.

REFERENCES

Abu Taimeh, A. (1988), Structural and applied remote sensing studies at Gharandal-Petra area, eastern Wadi Araba, M.Sc. thesis, Univ. of Jordan, Amman, Jordan.

Agnon, A., S. Marco, and C. Migowski (2006), Intraclast breccia layers in laminated sequences: Recorders of paleo-earthquakes, in *New Frontiers in Paleoenvironmental Research*, edited by Y. Enzel, A. Agnon, and M. Stein, *Spec. Pap. Geol. Soc. Am.*, *401*, 195–214.

Aldersons, F., Z. Ben-Avraham, A. Hofstetter, E. Kissling, and T. Al-Yazjeen (2003), Lower-crustal strength under the Dead Sea basin from local earthquake data and rheological modelling, *Earth Planet. Sci. Lett.*, *214*, 129–142, doi:10.1016/S0012-821X(03)00381-9.

Ambraseys, N. N., C. P. Melville, and R. D. Adams (1994), *The Seismicity of Egypt, Arabia and the Red Sea: A Historical Review*, Cambridge Univ. Press, Cambridge, U. K.

Amiran, D. H. K., E. Arieh, and T. Turcotte (1994), Earthquakes in Israel and adjacent areas, macroscopic observations since 100 B.C.E, *Isr. Explor. J.*, *44*, 260–305.

Amit, R., E. Zilberman, and Y. Enzel (2002), Paleoseismic evidence for time dependency of seismic response on a fault system in the southern Arava Valley, Dead Sea rift, Israel, *Geol. Soc. Am. Bull.*, *114*(2), 192–206, doi:10.1130/0016-7606(2002)114<0192:PEFTDO>2.0.CO;2.

Atwater, T., and J. Stock (1998), Pacific-North America plate tectonics of the Neogene southwestern United States: An update, *Int. Geol. Rev.*, *40*, 375–402.

Avni, Y., Z. Bartov, Z. Garfunkel, and H. Ginat (2001), The Arava Formation—A Pliocene sequence in the Arava Valley and its western margin, southern Israel, *Isr. J. Earth Sci.*, *50*, 101–120, doi:10.1092/5U6A-RM5E-M8E3-QXM7.

Baldock, G., and T. Stern (2005), Width of mantle deformation across a continental transform: Evidence from upper mantle (Pn) seismic anisotropy measurements, *Geology*, *33*, 741–744, doi:10.1130/G21605.1.

Bandel, K., and H. Khouri (1981), Lithostratigraphy of the Triassic of Jordan, *Facies*, *4*, 1–26, doi:10.1007/BF02536584.

Barjous, M. O. (1988), Structural study of the area between Petra and Ash Shawbak, M.Sc. thesis, Univ. of Jordan, Amman, Jordan.

Barka, A. (1992), The North Anatolian Fault, *Ann. Tecton.*, *6*, 164–195.

Bartov, Y. (1974), A structural and paleogeographic study of the central Sinai faults and domes (in Hebrew), Ph.D. thesis, Hebrew Univ., Jerusalem.

Bartov, Y., and H. Sagy (2004), Late Pleistocene extension and strike slip in the Dead Sea Basin, *Geol. Mag.*, *141*, 565–572, doi:10.1017/S001675680400963X.

Bartov, Y., Y. Avni, R. Calvo, and U. Frieslander (1998), The Zofar Fault—A major intra-rift feature in the Arava rift valley, *Geol. Surv. Isr. Curr. Res.*, *11*, 27–32.

Becken, M., O. Ritter, S. K. Park, P. A. Bedrosian, U. Weckmann, and M. Weber (2008), A deep crustal fluid channel into the San Andreas Fault system near Parkfield, California, *Geophys. J. Int.*, *173*, 718–732, doi:10.1111/j.1365-246X.2008.03754.x.

Bedrosian, P. A., M. J. Unsworth, and G. Egbert (2002), Magnetotelluric imaging of the creeping segment of the San Andreas Fault near Hollister, *Geophys. Res. Lett.*, *29*(11), 1506, doi:10.1029/2001GL014119.

Bedrosian, P., N. Maercklin, U. Weckmann, Y. Bartov, T. Ryberg, and O. Ritter (2007), Lithology-derived structure classification from joint interpretation of magnetotelluric and seismic models, *Geophys. J. Int.*, *170*, 737–748, doi:10.1111/j.1365-246X.2007.03440.x.

Ben-Avraham, Z. (1985), Structural framework of the Gulf of Elat (Aqaba), northern Red Sea, *J. Geophys. Res.*, *90*, 703–726, doi:10.1029/JB090iB01p00703.

Ben-Avraham, Z., and M. Lazar (2006), The structure and development of the Dead Sea basin: Recent studies, in *New Frontiers in Dead Sea Paleoenvironmental Research*, edited by Y. Enzel, A. Agnon, and M. Stein, *Spec. Pap. Geol. Soc. Am.*, *401*, 1–13, doi:10.1130/2006.2401(01).

Ben-Avraham, Z., and G. Schubert (2006), Deep "drop-down" basin in the southern Dead Sea, *Earth Planet. Sci. Lett.*, *251*, 254–263, doi:10.1016/j.epsl.2006.09.008.

Ben-Avraham, Z., R. Haenel, and H. Villinger (1978), Heat flow through the Dead Sea rift, *Mar. Geol.*, *28*, 253–269, doi:10.1016/0025-3227(78)90021-X.

Ben-Avraham, Z., Z. Garfunkel, and M. Lazar (2008), Geology and evolution of the southern Dead Sea fault with emphasis on subsurface structure, *Annu. Rev. Earth Planet. Sci.*, *36*, 357–387, doi:10.1146/annurev.earth.36.031207.124201.

Bender, F. (1968), *Geologie von Jordanien, Beitr. zur Reg. Geol. der Erde*, vol. 7, Gebrüder Borntraeger, Berlin.

Bender, F. (1974), Geological map of the Wadi Araba, Jordan, scale 1:100,000, 3 sheets, Geol. Surv. of the Fed. Rep. of Ger., Hannover, Germany.

Ben-Zion, Y., and C. G. Sammis (2003), Characterization of fault zones, *Pure Appl. Geophys.*, *160*, 677–715, doi:10.1007/PL00012554.

Bosworth, W., P. Huchon, and K. McClay (2005), The Red Sea and Gulf of Aden basins, *J. Afr. Earth Sci.*, *43*, 334–378, doi:10.1016/j.jafrearsci.2005.07.020.

Brocher, T. M., J. McCarthy, P. E. Hart, W. S. Holbrook, K. P. Furlong, T. V. McEvilly, J. A. Hole, and S. L. Klemperer (1994), Seismic evidence for a lower-crustal detachment beneath San Francisco Bay, California, *Science*, *265*, 1436–1439, doi:10.1126/science.265.5177.1436.

Caine, J. S., J. P. Evans, and C. P. Forster (1996), Fault zone architecture and permeability structure, *Geology*, *24*, 1025–1028, doi:10.1130/0091-7613(1996)024<1025:FZAAPS>2.3.CO;2.

Calvo, R., and Y. Bartov (2001), Hazeva Group, southern Israel: New observations, and their implications for its stratigraphy, paleogeography, and tectono-sedimentary regime, *Isr. J. Earth Sci.*, *50*, 71–99.

Chester, F. M., and J. M. Logan (1986), Implications for mechanical properties of brittle faults from observations of Punchbowl fault zone, California, *Pure Appl. Geophys.*, *124*, 79–106, doi:10.1007/BF00875720.

Chester, F. M., J. P. Evans, and R. L. Biegel (1993), Internal structure and weakening mechanisms of faults of the San Andreas Fault system, *J. Geophys. Res.*, *98*, 771–786, doi:10.1029/92JB01866.

DESERT Group (2004), The crustal structure of the Dead Sea Transform, *Geophys. J. Int.*, *156*, 655–681, doi:10.1111/j.1365-246X.2004.02143.x.

Dickinson, W. R., and W. S. Snyder (1979), Geometry of subducted slabs related to San Andreas transform, *J. Geol.*, *87*, 609–627.

Dziewonski, A. M., and D. L. Anderson (1981), Preliminary reference Earth model, *Phys. Earth Planet. Inter.*, *25*, 297–356, doi:10.1016/0031-9201(81)90046-7.

Eckstein, Y., and G. Simmons (1978), Review of heat flow data from the eastern Mediterranean region, *Pure Appl. Geophys.*, *117*, 150–159, doi:10.1007/BF00879742.

El-Isa, Z., J. Mechie, C. Prodehl, J. Makris, and R. Rihm (1987a), A crustal structure study of Jordan derived from seismic refraction data, *Tectonophysics*, *138*, 235–253, doi:10.1016/0040-1951(87)90042-4.

El-Isa, Z., J. Mechie, and C. Prodehl (1987b), Shear velocity structure of Jordan from explosion seismic data, *Geophys. J. R. Astron. Soc.*, *90*, 265–281.

Evans, J. P., and F. M. Chester (1995), Fluid-rock interaction in faults of the San Andreas system: Inferences from San Gabriel fault rock geochemistry and microstructures, *J. Geophys. Res.*, *100*, 13,007–13,020, doi:10.1029/94JB02625.

Evans, J. P., C. B. Forster, and V. J. Goddard (1997), Permeability of fault related rocks, and implications for hydraulic structure of fault zones, *J. Struct. Geol.*, *19*, 1393–1404, doi:10.1016/S0191-8141(97)00057-6.

Eyal, M., Y. Eyal, Y. Bartov, and G. Steinitz (1981), The tectonic development of the western margin of the Gulf of Elat (Aqaba) rift, *Tectonophysics*, *80*(1–4), 39–66, doi:10.1016/0040-1951(81)90141-4.

Faulkner, D. R., A. C. Lewis, and E. H. Rutter (2003), On the internal structure and mechanics of large strike-slip zones: Field observations of the Carboneras fault in southeast Spain, *Tectonophysics*, *367*, 235–251, doi:10.1016/S0040-1951(03)00134-3.

Finzi, Y. (2004), Current deformation in the southern Dead Sea Transform: Radar interferometry measurements and tectonic implication analysis, M.Sc. thesis, Inst. of Earth Sci., Hebrew Univ., Jerusalem.

Fleischer, L., and A. Varshavsky (2002), A lithostratigraphic data base of oil and gas wells drilled in Israel, *Rep. OG/9/02*, 19 pp., Oil and Gas Unit, Minist. of Natl. Infrastruct., Jerusalem.

Förster, A., H. J. Förster, R. Masarweh, A. Masri, K. Tarawneh, and DESERT Group (2007), The terrestrial heat flow of the Arabian shield in Jordan, *Int. J. Earth Sci.*, *30*, 271–284, doi:10.1016/j.jseaes.2006.09.002.

Förster, H.-J., R. Oberhänsli, S. V. Sobolev, A. Förster, and D. Stromeyer (2004), Lithosphere composition and thermal regime across the Dead Sea Transform in Israel and Jordan, *Eos Trans. AGU*, *85*(17), Jt. Assem. Suppl., Abstract T11A-05.

Freund, R. (1965), A model for the development of Israel and adjacent areas since the Upper Cretaceous, *Geol. Mag.*, *102*, 189–205.

Freund, R., Z. Garfunkel, I. Zak, M. Goldberg, T. Weissbrod, and B. Derin (1970), The shear along the Dead Sea rift, *Philos. Trans. R. Soc. London, Ser. A*, *267*(1181), 107–130.

Frieslander, U. (2000), The structure of the Dead Sea Transform emphasizing the Arava, using new geophysical data (in Hebrew), Ph.D. thesis, Hebrew Univ., Jerusalem.

Fuis, G. (1998), West margin of North America—A synthesis of recent seismic transects, *Tectonophysics*, *288*, 265–292, doi:10.1016/S0040-1951(97)00300-4.

Fuis, G. S., T. Ryberg, N. Godfrey, D. A. Okaya, and J. M. Murphy (2001), Crustal structure and tectonics from the Los Angeles basin to the Mojave Desert, southern CA, *Geology*, *29*, 15–18, doi:10.1130/0091-7613(2001)029<0015:CSATFT>2.0.CO;2.

Fuis, G. S., M. D. Kohler, M. Scherwath, U. ten Brink, H. J. A. Van Avendong, and J. M. Murphy (2008), A comparison between the transpressional plate boundaries of the South Island, New Zealand, and southern California, USA: The Alpine and San Andreas Fault systems, in *A Continental Plate Boundary: Tectonics at South Island, New Zealand, Geophys. Monogr. Ser.*, vol. 175, edited by D. Okaya, T. Stern, and F. Davey, pp. 307–327, doi:10.1029/175GM16, AGU, Washington, D. C.

Fumal, T. E., J. R. Weldon II, G. P. Biasi, T. E. Dawson, G. G. Seitz, W. T. Frost, and D. P. Schwartz (2002), Evidence for large earthquakes on the San Andreas Fault at the Wrightwood, California, paleoseismic site: A.D. 500 to present, *Bull. Seismol. Soc. Am.*, *92*(7), 2726–2760, doi:10.1785/0120000608.

Furlong, K. P., and R. Govers (1999), Ephemeral crustal thickening at a triple junction: The Mendocino crustal conveyor, *Geology*, *27*, 127–130, doi:10.1130/0091-7613(1999)027<0127:ECTAAT>2.3.CO;2.

Furlong, K. P., W. D. Hugo, and G. Zandt (1989), Geometry and evolution of the San Andreas Fault zone, *J. Geophys. Res.*, *94*, 3100–3110, doi:10.1029/JB094iB03p03100.

Gardosh, M., E. Kashai, S. Salhov, H. Shulman, and E. Tannenbaum (1997), Hydrocarbon exploration in the southern Dead Sea area, in *The Dead Sea*, edited by T. N. Niemi, Z. Ben-Avraham, and J. Gat, pp. 57–72, Oxford Univ. Press, Oxford, U. K.

Garfunkel, Z. (1981), Internal structure of the Dead Sea leaky transform (rift) in relation to plate kinematics, *Tectonophysics*, *80*, 81–108, doi:10.1016/0040-1951(81)90143-8.

Garfunkel, Z. (1988), The pre-Quaternary geology of Israel, in *The Zoogeography of Israel*, edited by Y. Yom-Tov and E. Ternov, pp. 7–34, W. Junk, Dordrecht, Netherlands.

Garfunkel, Z. (1989), The tectonic setting of Phanerozoic magmatism in Israel, *Isr. J. Earth Sci.*, *38*, 51–74.

Garfunkel, Z. (1997), The history and formation of the Dead Sea basin, in *The Dead Sea*, edited by T. N. Niemi, Z. Ben-Avraham, and J. Gat, pp. 36–56, Oxford Univ. Press, Oxford, U. K.

Garfunkel, Z., and Z. Ben-Avraham (1996), The structure of the Dead Sea basin, *Tectonophysics*, *266*, 155–176, doi:10.1016/S0040-1951(96)00188-6.

Garfunkel, Z., and Z. Ben-Avraham (2001), Basins along the Dead Sea Transform, in *Peri-Tethys Memoir 6*, edited by P. A. Ziegler et al., *Mem. Mus. Natl. Hist. Nat.*, *186*, 607–627.

Garfunkel, Z., and M. Beyth (2006), Constraints on the structural development of Afar imposed by the kinematics of the major surrounding plates, in *The Afar Volcanic Province within the East African Rift System*, edited by G. Yirgu, C. J. Ebinger, and P. K. H. Maguire, *Geol. Soc. Spec. Publ.*, *259*, 23–42.

Garfunkel, Z., I. Zak, and R. Freund (1981), Active faulting in the Dead Sea Rift, *Tectonophysics*, *80*, 1–26, doi:10.1016/0040-1951(81)90139-6.

Gass, I. G. (1970), The evolution of volcanism in the junction area of the Red Sea, gulf of Aden and Ethiopian rifts, *Philos. Trans. R. Soc. London, Ser. A*, *267*, 369–381, doi:10.1098/rsta.1970.0042.

Ginzburg, A., and Z. Ben-Avraham (1997), A seismic refraction study of the north basin of the Dead Sea, *Geophys. Res. Lett.*, *24*, 2063–2066, doi:10.1029/97GL01884.

Ginzburg, A., and E. Kashai (1981), Seismic measurements in the southern Dead Sea, *Tectonophysics*, *80*, 67–80, doi:10.1016/0040-1951(81)90142-6.

Ginzburg, A., J. Makris, K. Fuchs, C. Prodehl, W. Kaminski, and U. Amitai (1979a), A seismic study of the crust and upper mantle of the Jordan–Dead Sea Rift and their transition toward the Mediterranean Sea, *J. Geophys. Res.*, *84*, 1569–1582, doi:10.1029/JB084iB04p01569.

Ginzburg, A., J. Makris, K. Fuchs, B. Perathoner, and C. Prodehl (1979b), Detailed structure of the crust and upper mantle along the Jordan–Dead Sea Rift, *J. Geophys. Res.*, *84*, 5605–5612, doi:10.1029/JB084iB10p05605.

Goes, S., R. Govers, S. Schwartz, and K. Furlong (1997), Three-dimensional thermal modeling for the Mendocino triple junction area, *Earth Planet. Sci. Lett.*, *148*, 45–57, doi:10.1016/S0012-821X(97)00044-7.

Götze, H. J., R. El-Kelani, S. Schmidt, M. Rybakov, H. J. Förster, and J. Ebbing (2006), Integrated 3-D density modelling and segmentation of the Dead Sea Transform, *Int. J. Earth Sci.*, *96*, 289–302, doi:10.1007/s00531-006-0095-5.

Haberland, C., A. Agnon, R. El-Kelani, N. Maercklin, I. Qabbani, G. Rümpker, T. Ryberg, F. Scherbaum, and M. Weber (2003), Modeling of seismic guided waves at the Dead Sea Transform, *J. Geophys. Res.*, *108*(B7), 2342, doi:10.1029/2002JB002309.

Haberland, C., N. Maercklin, D. Kesten, T. Ryberg, C. Janssen, A. Agnon, M. Weber, A. Schulze, I. Qabbani, and R. El-Kelani (2006), Shallow architecture of the Wadi Araba fault (Dead Sea Transform) from high-resolution seismic investigations, *Tectonophysics*, *432*, 37–50, doi:10.1016/j.tecto.2006.12.006.

Handy, M. R., G. Hirth, and N. Hovius (2007), *Tectonic Faults—Agents of Change on a Dynamic Earth, Dahlem Workshop Rep. 95*, MIT Press, Cambridge, Mass.

Harding, T. P., and J. Lowell (1979), Structural styles, their plate-tectonic habitats, and hydrocarbon traps in petroleum provinces, *Am. Assoc. Pet. Geol. Bull.*, *63*(7), 1016–1058.

Henstock, T. J., A. Levander, and J. A. Hole (1997), Deformation in the lower crust of the San Andreas Fault system in northern California, *Science*, *278*, 650–653, doi:10.1126/science.278.5338.650.

Herquel, G., P. Tapponnier, G. Wittlinger, J. Mei, and S. Danian (1999), Teleseismic shear wave splitting and lithospheric anisotropy beneath and across the Altyn Tagh fault, *Geophys. Res. Lett.*, *26*, 3225–3228, doi:10.1029/1999GL005387.

Hoffmann-Rothe, A., O. Ritter, and C. Janssen (2004), Correlation of electrical conductivity and structural damage at a major strike-slip fault in northern Chile, *J. Geophys. Res.*, *109*, B10101, doi:10.1029/2004JB003030.

Hofstetter, A., H. K. Thio, and G. Shamir (2003), Source mechanism of the 22/11/1995 Gulf of Aqaba earthquake and its aftershock sequence, *J. Seismol.*, *7*, 99–114, doi:10.1023/A:1021206930730.

Holbrook, W. S., T. M. Brocher, U. S. Ten Brink, and J. A. Hole (1996), Crustal structure of a transform plate boundary: San Francisco Bay and the central California continental margin, *J. Geophys. Res.*, *101*, 22,311–22,334, doi:10.1029/96JB01642.

Holdsworth, R. E., M. Hand, J. A. Miller, and I. S. Buick (2001), Continental reactivation and reworking: An introduction, in *Continental Reactivation and Reworking*, edited by J. A. Miller et al., *Geol. Soc. Spec. Publ.*, *184*, 1–12.

Hole, J. A., R. D. Catchings, K. C. St. Clair, M. J. Rymer, D. A. Okaya, and B. J. Carney (2001), Steep-dip seismic imaging of the shallow San Andreas Fault near Parkfield, *Science*, *294*, 1513–1515, doi:10.1126/science.1065100.

Hubert-Ferrari, A., R. Armijo, G. King, and B. Meyer (2002), Morphology, displacement and slip rates along the North Anatolian Fault, Turkey, *J. Geophys. Res.*, *107*(B10), 2235, doi:10.1029/2001JB000393.

Ibrahim, K. M. K. (1991), The geology of the Wadi Rahma, *Geol. Mapp. Ser., Geol. Bull., 15*, map sheet 3049 IV, scale 1:50,000, Geol. Mapp. Div., Geol. Dir., Nat. Resour. Auth., Amman, Jordan.

Ilani, S., Y. Harlavan, K. Tarawneh, I. Rabba, R. Weinberger, K. Ibrahim, S. Petz, and G. Steinitz (2001), New K-Ar ages of basalts from the Harrat Ash Shaam volcanic field in Jordan: Implications for the span and duration of the upper-mantle upwelling beneath the western Arabian plate, *Geology*, *29*, 171–174, doi:10.1130/0091-7613(2001)029<0171:NKAAOB>2.0.CO;2.

Janssen, C., R. L. Romer, A. Hoffmann-Rothe, D. Kesten, and H. Al-Zubi (2004), The Dead Sea Transform: Evidence for a strong fault?, *J. Geol.*, *112*, 561–575, doi:10.1086/422666.

Janssen, C., R. L. Romer, A. Hoffmann-Rothe, B. Mingram, P. Dulski, P. Möller, H. Al-Zubi, and the DESERT Research Group (2005), The role of fluids in faulting deformation a case study from the Dead Sea Transform (Jordan), *Int. J. Earth Sci.*, *94*, 243–255, doi:10.1007/s00531-004-0461-0.

Janssen, C., A. Hoffmann-Rothe, M. Bohnhoff, U. Wetzel, A. Matar, M. Khatib, and the DESERT Research Group (2007a), Different styles of faulting deformation along the Dead Sea Transform and possible consequences for the recurrence of major earthquakes, *J. Geodyn.*, *44*, 66–89, doi:10.1016/j.jog.2007.01.002.

Janssen, C., R. L. Romer, B. Plessen, R. Naumann, A. Hoffmann-Rothe, and A. Matar (2007b), Contrasting fluid regimes along the Dead Sea Transform, *Geofluids*, *7*, 275–291, doi:10.1111/j.1468-8123.2007.00185.x.

Jiracek, G. R., V. M. Gonzalez, T. G. Caldwell, P. E. Wannamaker, and D. Kilb (2008), Seismogenic, electrically conductive, and fluid zones at continental plate boundaries in New Zealand, Himalaya, and California-USA, in *A Continental Plate Boundary: Tectonics at South Island, New Zealand, Geophys. Monogr. Ser.*, vol. 175, edited by D. Okaya, T. Stern, and F. Davey, pp. 347–369, doi:10.1029/175GM18, AGU, Washington, D. C.

Joffe, S., and Z. Garfunkel (1987), The plate kinematics of the circum Red Sea—A re-evaluation, *Tectonophysics*, *141*, 5–22, doi:10.1016/0040-1951(87)90171-5.

Kashai, E. L., and P. F. Croker (1987), Structural geometry and evolution of the Dead Sea–Jordan rift system as deduced from new subsurface data, *Tectonophysics*, *141*, 33–60, doi:10.1016/0040-1951(87)90173-9.

Kennedy, B. M., Y. K. Kharaka, W. C. Evans, A. Ellwood, D. J. DePaolo, J. Thordsen, and R. H. Mariner (1997), Mantle fluids in the San Andreas Fault system, California, *Science*, *278*, 1278–1281, doi:10.1126/science.278.5341.1278.

Kennett, B. L. N., and E. R. Engdahl (1991), Travel-times for global earthquake location and phase identification, *Geophys. J. Int.*, *105*, 429–465, doi:10.1111/j.1365-246X.1991.tb06724.x.

Kennett, B. L. N., E. R. Engdahl, and R. Buland (1995), Constraints on seismic velocities in the Earth from traveltimes, *Geophys. J. Int.*, *122*, 108–124, doi:10.1111/j.1365-246X.1995.tb03540.x.

Ken-Tor, R., A. Agnon, Y. Enzel, M. Stein, S. Marco, and J. F. W. Negendank (2001), High-resolution geological record of historic earthquakes in the Dead Sea basin, *J. Geophys. Res.*, *106*, 2221–2234, doi:10.1029/2000JB900313.

Kesten, D. (2004), Structural observations at the southern Dead Sea Transform from seismic reflection data and ASTER satellite images, Ph.D. thesis, Univ. Potsdam, Potsdam, Germany.

Kesten, D., M. Weber, C. Haberland, C. Janssen, A. Agnon, Y. Bartov, I. Rabba, and the DESERT Group (2008), Combining satellite and seismic images to analyze the shallow structure of the Dead Sea Transform near the DESERT transect, *Int. J. Earth Sci.*, *97*, 153–169, doi:10.1007/s00531-006-0168-5.

Kharaka, Y. K., J. T. James, W. C. Evans, and B. M. Kennedy (1999), Geochemistry and hydromechanical interactions of fluids associated with the San Andreas Fault system, California, in *Faults and Subsurface Fluid Flow in the Shallow Crust, Geophys. Monogr. Ser.*, vol. 113, edited by W. C. Haneberg, pp. 129–148, AGU, Washington, D. C.

Klinger, Y., J. Avouac, L. Dorbath, N. A. Karaki, and N. Tisnerat (2000a), Seismic behavior of the Dead Sea fault along Araba valley, Jordan, *Geophys. J. Int.*, *142*, 769–782, doi:10.1046/j.1365-246x.2000.00166.x.

Klinger, Y., J. Avouac, N. A. Karaki, L. Dorbath, D. Bourles, and J. L. Reyss (2000b), Slip rate on the Dead Sea Transform fault in northern Araba valley (Jordan), *Geophys. J. Int.*, *142*, 755–768, doi:10.1046/j.1365-246x.2000.00165.x.

Koulakov, I., and S. V. Sobolev (2006), Moho depth and three-dimensional *P* and *S* structure of the crust and uppermost mantle in the eastern Mediterranean and Middle East derived from tomographic inversion of local ISC data, *Geophys. J. Int.*, *164*, 218–235, doi:10.1111/j.1365-246X.2005.02791.x.

Koulakov, I., S. V. Sobolev, M. Weber, S. Oreshin, K. Wylegalla, and R. Hofstetter (2006), Teleseismic tomography reveals no signature of the Dead Sea Transform in the upper mantle structure, *Earth Planet. Sci. Lett.*, *252*, 189–200, doi:10.1016/j.epsl.2006.09.039.

Lachenbruch, A. H., and J. H. Sass (1980), Heat flow and energetics of the San Andreas Fault zone, *J. Geophys. Res.*, *85*, 6185–6222, doi:10.1029/JB085iB11p06185.

Laske, G., M. Weber, and the DESERT Working Group (2008), Lithosphere structure across the Dead Sea Transform as constrained by Rayleigh waves observed during the DESERT experiment, *Geophys. J. Int.*, *173*, 593–610, doi:10.1111/j.1365-246X.2008.03749.x.

LeBeon, M., Y. Klinger, A. Agnon, L. Dorbath, G. Baer, A. S. Mériaux, J. C. Ruegg, O. Charade, R. Finkel, and F. Ryerson (2006), Geodetic versus geologic slip rate along the Dead Sea Fault, paper presented at Annual Meeting, Seismol. Soc. of Am., San Francisco, Calif., 18–22 April.

Lewis, M., Z. Peng, Y. Ben-Zion, and F. Vernon (2005), Shallow seismic trapping structure in the San Jacinto fault zone near Anza, California, *Geophys. J. Int.*, *162*, 867–881, doi:10.1111/j.1365-246X.2005.02684.x.

Li, Y. G., P. Leary, K. Aki, and P. E. Malin (1990), Seismic trapped modes in the Oroville and San Andreas Fault zone, *Science*, *249*, 763–765, doi:10.1126/science.249.4970.763.

Li, Y. G., W. L. Ellsworth, C. H. Thurber, P. E. Malin, and K. Aki (1997), Fault-zone guided waves from explosions in the San Andreas Fault at Parkfield and Cienega Valley, California, *Bull. Seismol. Soc. Am.*, *87*(1), 210–221.

Li, Y. G., K. Aki, J. E. Vidale, and M. G. Alvarez (1998), A delineation of the Nojima fault ruptured in the *M* 7.2 Kobe, Japan, earthquake of 1995 using fault zone trapped waves, *J. Geophys. Res.*, *103*(B4), 7247–7263, doi:10.1029/98JB00166.

Lin, A., N. Tanaka, S. Uda, and M. Satish-Kumar (2001), Infiltration of meteoric and sea water into deep fault zones during episodes of coseismic events: A case study of the Nojima Fault, Japan, *Bull. Earthquake Res. Inst. Univ. Tokyo*, *76*, 341–353.

Lowell, J. D. (1985), *Structural Styles in Petroleum Exploration*, Oil and Gas Consult. Int., Tulsa, Okla.

Lyakhovsky, V., Y. Ben-Zion, and A. Agnon (2001), Earthquake cycle, fault zones, and seismicity patterns in a rheologically layered lithosphere, *J. Geophys. Res.*, *106*, 4103–4120, doi:10.1029/2000JB900218.

Maercklin, N. (2004), Seismic structure of the Arava Fault, Dead Sea Transform, Ph.D. thesis, Univ. Potsdam, Potsdam, Germany.

Maercklin, N., C. Haberland, T. Ryberg, M. Weber, Y. Bartov, and the DESERT Group (2004), Imaging the Dead Sea Transform with scattered seismic waves, *Geophys. J. Int.*, *158*, 179–186, doi:10.1111/j.1365-246X.2004.02302.x.

Maercklin, N., P. A. Bedrosian, C. Haberland, O. Ritter, T. Ryberg, M. Weber, and U. Weckmann (2005), Characterizing a large shear-zone with seismic and magnetotelluric methods: The case of the Dead Sea Transform, *Geophys. Res. Lett.*, *32*, L15303, doi:10.1029/2005GL022724.

Mahmoud, S., R. Reilinger, S. McClusky, P. Vernant, and A. Tealeb (2005), GPS evidence for northward motion of the Sinai Block: Implications for E. Mediterranean tectonics, *Earth Planet. Sci. Lett.*, *238*, 217–224, doi:10.1016/j.epsl.2005.06.063.

Makris, J., Z. Ben-Avraham, A. Behle, A. Ginzburg, P. Giese, L. Steinmetz, R. B. Whitmarsch, and S. Eleftheriou (1983), Seismic refraction profiles between Cyprus and Israel and their interpretation, *Geophys. J. R. Astron. Soc.*, *75*, 575–591.

Marco, S., M. Stein, and A. Agnon (1996), Long-term earthquake clustering: A 50,000 year paleoseismic record in the Dead Sea Graben, *J. Geophys. Res.*, *101*, 6179–6191, doi:10.1029/95JB01587.

Marco, S., T. K. Rockwell, A. Heimann, U. Frieslander, and A. Agnon (2005), Late Holocene activity of the Dead Sea Transform revealed in 3D paleo-seismic trenches on the Jordan Gorge segment, *Earth Planet. Sci. Lett.*, *234*, 189–205, doi:10.1016/j.epsl.2005.01.017.

McClusky, S., et al. (2000), Global Positioning System constraints on plate kinematics and dynamics in the eastern Mediterranean and Caucasus, *J. Geophys. Res.*, *105*, 5695–5719.

McGuire, A. V., and R. G. Bohannon (1989), Timing of mantle upwelling: Evidence for a passive origin for the Red Sea Rift, *J. Geophys. Res.*, *94*, 1677–1682, doi:10.1029/JB094iB02p01677.

McNamara, D. E., T. J. Owens, P. G. Silver, and F. T. Wu (1994), Shear wave anisotropy beneath the Tibetan Plateau, *J. Geophys. Res.*, *99*, 13,655–13,665, doi:10.1029/93JB03406.

Mechie, J., K. Abu-Ayyash, Z. Ben-Avraham, R. El-Kelani, A. Mohsen, G. Rümpker, J. Saul, and M. Weber (2005), Crustal shear velocity structure across the Dead Sea Transform from two-dimensional modelling of DESERT project explosion seismic data, *Geophys. J. Int.*, *160*, 910–924, doi:10.1111/j.1365-246X.2005.02526.x.

Migowski, C., A. Agnon, R. Bookman, J. F. W. Negendank, and M. Stein (2004), Recurrence pattern of Holocene earthquakes along the Dead Sea Transform revealed by varve-counting and radiocarbon dating of lacustine sediments, *Earth Planet. Sci. Lett.*, *222*, 301–314, doi:10.1016/j.epsl.2004.02.015.

Mohsen, A., R. Hofstetter, G. Bock, R. Kind, M. Weber, K. Wylegalla, G. Rümpker, and the DESERT Group (2005), A receiver function study across the Dead Sea Transform, *Geophys. J. Int.*, *160*, 948–960, doi:10.1111/j.1365-246X.2005.02534.x.

Mohsen, A., R. Kind, S. V. Sobolev, M. Weber, and the DESERT Group (2006), Thickness of the lithosphere east of the Dead Sea Transform, *Geophys. J. Int.*, *167*, 845–852, doi:10.1111/j.1365-246X.2006.03185.x.

Mooney, W. D., G. C. Beroza, and R. Kind (2007), Fault zones from top to bottom: A geophysical perspective, in *Tectonic Faults—Agents of Change on a Dynamic Earth, Dahlem Workshop Rep. 95*, edited by M. R. Handy, G. Hirth, and N. Hovius, pp. 9–46, MIT Press, Cambridge, Mass.

Neev, D., and J. K. Hall (1979), Geophysical investigations in the Dead Sea, *Sediment. Geol.*, *23*, 209238, doi:10.1016/0037-0738(79)90015-0.

Netzeband, G., K. Gohl, C. Hübscher, Z. Ben-Avraham, A. Dehghani, D. Gajewski, and P. Liersch (2006), The Levantine Basin—Crustal structure and origin, *Tectonophysics*, *418*, 178–188, doi:10.1016/j.tecto.2006.01.001.

Nicholson, C., C. C. Sorlien, T. Atwater, J. C. Crowell, and B. P. Luyendyk (1994), Microplate capture, rotation of the western Transverse Ranges, and initiation of the San Andreas transform as a low-angle fault system, *Geology*, *22*, 491–495, doi:10.1130/0091-7613(1994)022<0491:MCROTW>2.3.CO;2.

Niemi, T. M., H. Zhang, M. Atallah, and J. B. Harrison (2001), Late Pleistocene and Holocene slip rate of the northern Wadi Araba fault, Dead Sea Transform, Jordan, *J. Seismol.*, *5*, 449–474, doi:10.1023/A:1011487912054.

Ohtani, T., K. Fujimoto, H. Ito, H. Tanaka, N. Tomida, and T. Higuchi (2000), Fault rocks and past to recent fluid characteristics from the borehole survey of the Nojima fault ruptured in the 1995 Kobe earthquake, southwest Japan, *J. Geophys. Res.*, *105*, 16,161–16,171, doi:10.1029/2000JB900086.

Oskin, M., J. Stock, and A. Martin-Barajas (2001), Rapid localization of the Pacific–North America plate motion in the Gulf of California, *Geology*, *29*, 459–462, doi:10.1130/0091-7613(2001)029<0459:RLOPNA>2.0.CO;2.

Pasyanos, M., and A. A. Nyblade (2007), A top to bottom lithospheric study of Africa and Arabia, *Tectonophysics*, *444*, 27–44, doi:10.1016/j.tecto.2007.07.008.

Petrunin, A. G., and S. V. Sobolev (2006), What controls thickness of sediments and lithospheric deformation at a pull-apart basin?, *Geology*, *34*(5), 389–392.

Pili, E., F. Poitrasson, and J. P. Gratier (2002), Carbon-oxygen isotope and trace element constraint on how fluids percolate faulted limestones from the San Andreas Fault system: Partitioning of fluid sources and pathways, *Chem. Geol.*, *190*, 231–250, doi:10.1016/S0009-2541(02)00118-3.

Powell, R. E. (1993), Balanced palinspastic reconstruction of pre-late Cenozoic paleogeology, southern California: Geologic and kinematic constraints on evolution of the San Andreas Fault system, *Mem. Geol. Soc. Am.*, *178*, 1–106.

Quennell, A. M. (1958), The structural and geomorphic evolution of the Dead Sea Rift, *Q. J. Geol. Soc. London*, *114*, 1–24.

Rabb'a, I. (1991), Al Quwayra, *Geol. Map 3051 II*, scale 1:50,000, Geol. Dir., Nat. Resour. Auth., Amman, Jordan.

Reilinger, R., et al. (2006), GPS constraints on continental deformation in the Africa-Arabia-Eurasia continental collision zone and implications for the dynamics of plate interactions, *J. Geophys. Res.*, *111*, B05411, doi:10.1029/2005JB004051.

Ritter, O., T. Ryberg, U. Weckmann, A. Hoffmann-Rothe, A. Abueladas, Z. Garfunkel, and DESERT Research Group (2003), Geophysical images of the Dead Sea Transform in Jordan reveal an impermeable barrier for fluid flow, *Geophys. Res. Lett.*, *30*(14), 1741, doi:10.1029/2003GL017541.

Ritter, O., A. Hoffmann-Rothe, P. A. Bedrosian, U. Weckmann, and V. Haak (2005a), Electrical conductivity images of active and fossil fault zones, in *High-Strain Zones: Structure and Physical Properties*, *Geol. Soc. Spec. Publ.*, *245*, 165–186.

Ritter, O., U. Weckmann, P. A. Bedrosian, M. Becken, and S. Park (2005b), Imaging the deep roots of the Dead Sea Fault and the San Andreas Fault with magnetotelluric measurements, paper presented at General Assembly 2005, Eur. Geosci. Union, Vienna, 24–29 Apr.

Rockwell, T. K., and Y. Ben-Zion (2007), High localization of primary slip zones in large earthquakes from paleoseismic trenches: Observations and implications for earthquake physics, *J. Geophys. Res.*, *112*, B10304, doi:10.1029/2006JB004764.

Rotstein, Y., Y. Bartov, and A. Hofstetter (1991), Active compressional tectonics in the Jericho area, Dead Sea Rift, *Tectonophysics*, *198*, 239–259, doi:10.1016/0040-1951(91)90153-J.

Rotstein, Y., Y. Bartov, and U. Frieslander (1992), Evidence for local shifting of the main fault and changes in the structural setting, Kinarot basin, Dead Sea Transform, *Geology*, *20*, 251–254, doi:10.1130/0091-7613(1992)020<0251:EFLSOT>2.3.CO;2.

Rümpker, G., and T. Ryberg (2000), New "Fresnel-zone" estimates for shear-wave splitting observations from finite-difference modeling, *Geophys. Res. Lett.*, *27*, 2005–2008, doi:10.1029/2000GL011423.

Rümpker, G., T. Ryberg, G. Bock, and the DESERT Seismology Group (2003), Boundary-layer mantle flow under the Dead Sea Transform fault inferred from seismic anisotropy, *Nature*, *425*, 497–501, doi:10.1038/nature01982.

Ryberg, T., and G. S. Fuis (1998), The San Gabriel Mountains bright reflective zone: Possible evidence of mid-crustal thrust faulting in southern California, *Tectonophysics*, *286*, 31–46, doi:10.1016/S0040-1951(97)00253-9.

Ryberg, T., G. Rümpker, C. Haberland, D. Stromeyer, and M. Weber (2005), Simultaneous inversion of shear waves splitting observations from seismic arrays, *J. Geophys. Res.*, *110*, B03301, doi:10.1029/2004JB003303.

Ryberg, T., M. Weber, Z. Garfunkel, and Y. Bartov (2007), The shallow velocity structure across the Dead Sea Transform fault, Arava Valley, from seismic data, *J. Geophys. Res.*, *112*, B08307, doi:10.1029/2006JB004563.

Salamon, A., A. Hofstetter, Z. Garfunkel, and H. Ron (1996), Seismicity of the eastern Mediterranean region: Perspective from the Sinai subplate, *Tectonophysics*, *263*, 293–305, doi:10.1016/S0040-1951(96)00030-3.

Salamon, A., A. Hofstetter, Z. Garfunkel, and H. Ron (2003), Seismotectonics of the Sinai sub-plate—The eastern Mediterranean region, *Geophys. J. Int.*, *155*, 149–173, doi:10.1046/j.1365-246X.2003.02017.x.

Savage, M. K. (1999), Seismic anisotropy and mantle deformation: What have we learned from shear wave splitting?, *Rev. Geophys.*, *37*, 65–106, doi:10.1029/98RG02075.

Scholz, C. H. (1987), Wear and gauge formation in brittle faulting, *Geology*, *15*, 493–495, doi:10.1130/0091-7613(1987)15<493:WAGFIB>2.0.CO;2.

Scholz, C. H. (2000), Evidence for a strong San Andreas Fault, *Geology*, *28*, 163–166, doi:10.1130/0091-7613(2000)28<163:EFASSA>2.0.CO;2.

Scholz, C. H. (2002), *The Mechanics of Earthquakes and Faulting*, 2nd ed., Cambridge Univ. Press, Cambridge, U. K.

Sengör, A. M. C. (1979), The North Anatolian transform fault: Its age offset and tectonic significance, *J. Geol. Soc.*, *136*, 269–282, doi:10.1144/gsjgs.136.3.0269.

Shamir, G., Y. Eyal, and I. Bruner (2005), Localized versus distributed shear in transform plate boundary zones: The case of the Dead Sea Transform in the Jericho Valley, *Geochem. Geophys. Geosyst.*, *6*, Q05004, doi:10.1029/2004GC000751.

Shaw, J. E., J. A. Baker, M. A. Menzies, M. F. Thirlwall, and K. M. Ibrahim (2003), Petrogenesis of the largest intraplate volcanic field of the Arabian Plate (Jordan): A mixed lithosphere–asthenosphere source activated by lithospheric extension, *J. Petrol.*, *44*, 1657–1679, doi:10.1093/petrology/egg052.

Shtivelman, V., U. Frieslander, E. Zilberman, and R. Amit (1998), Mapping shallow faults at the Evrona playa site using high-resolution reflection method, *Geophysics*, *63*(4), 1257–1264, doi:10.1190/1.1444427.

Silver, P. G. (1996), Seismic anisotropy beneath the continents: Probing the depth of geology, *Annu. Rev. Earth Planet. Sci.*, *24*, 385–432, doi:10.1146/annurev.earth.24.1.385.

Sneh, A., K. Ibrahim, Y. Bartov, I. Rabb'a, T. Weissbrod, K. Tarawneh, and M. Rosensaft (1998), Geological map of the Dead Sea Rift along Wadi Araba, in *Compilation of Earth Science Data, Dead Sea–Wadi Araba*, scale 1:250,000, Geol. Surv. of Isr., Jerusalem, Israel.

Sobolev, S. V., A. Grésillaud, and M. Cara (1999), How robust is isotropic delay time tomography for anisotropic mantle?, *Geophys. Res. Lett.*, *26*(4), 509–512, doi:10.1029/1998GL900206.

Sobolev, S. V., A. Petrunin, Z. Garfunkel, A. Y. Babeyko, and the DESERT Group (2005), Thermo-mechanical model of the Dead Sea Transform, *Earth Planet. Sci. Lett.*, *238*, 78–95, doi:10.1016/j.epsl.2005.06.058.

Stein, M., Z. Garfunkel, and E. Jagoutz (1993), Chronothermometry of peridotitic and pyroxenitic xenoliths: Implications for the thermal evolution of the Arabian lithosphere, *Geochim. Cosmochim. Acta*, *57*, 1325–1337, doi:10.1016/0016-7037(93)90069-9.

Steinitz, G., and Y. Bartov (1991), Miocene-Pleistocene history of the Dead Sea segment of the Rift in the light of K-Ar ages of basalts, *Isr. J. Earth Sci.*, *40*, 199–208.

Stirling, M. W., S. G. Wesnousky, and K. Shimazaki (1996), Fault trace complexity, cumulative slip, and the shape of the magnitude-frequency distribution for strike-slip faults: A global survey, *Geophys. J. Int.*, *124*(3), 833–868, doi:10.1111/j.1365-246X.1996.tb05641.x.

Tarawneh, B. (1992), The geology of the Fifa area, *Map 3051*, Nat. Resour. Auth. of Jordan, Amman, Jordan.

Tašárová, Z., H. J. Götze, R. El-Kelani, J. Ebbing, and M. Hassouneh (2006), Small-scale gravity modeling of upper crustal structures in the Araba Valley along the Dead Sea Transform, *Geochem. Geophys. Geosyst.*, *7*, Q09012, doi:10.1029/2005GC001229.

ten Brink, U. S., and Z. Ben-Avraham (1989), The anatomy of a pull-apart basin: Seismic reflection observations of the Dead Sea Basin, *Tectonics*, *8*, 333–350, doi:10.1029/TC008i002p00333.

ten Brink, U. S., M. Rybakov, A. S. Al-Zoubi, M. Hassouneh, U. Frieslander, A. T. Batayneh, V. Goldschmidt, M. N. Daoud, Y. Rotstein, and J. K. Hall (1999a), Anatomy of the Dead Sea Transform: Does it reflect continuous changes in plate motion?, *Geology*, *27*, 887–890, doi:10.1130/0091-7613(1999)027<0887:AOTDST>2.3.CO;2.

ten Brink, U. S., N. Shimizu, and P. C. Molzer (1999b), Plate deformation at depth under northern California: Slab gap or stretched slab?, *Tectonics*, *18*, 1084–1098, doi:10.1029/1999TC900050.

ten Brink, U. S., M. Rybakov, A. S. Al-Zoubi, and Y. Rotstein (2007), Magnetic character of a large continental transform: An aeromagnetic survey of the Dead Sea Fault, *Geochem. Geophys. Geosyst.*, *8*, Q07005, doi:10.1029/2007GC001582.

Turcotte, D. L., and G. Schubert (2002), *Geodynamics*, Cambridge Univ. Press, Cambridge, U. K.

Unsworth, M. J., P. E. Malin, G. D. Egbert, and J. R. Booker (1997), Internal structure of the San Andreas Fault at Parkfield, *Calif. Geol.*, *25*, 359–362.

Unsworth, M. J., G. Egbert, and J. Booker (1999), High-resolution electromagnetic imaging of the San Andreas Fault in central California, *J. Geophys. Res.*, *104*, 1131–1150, doi:10.1029/98JB01755.

Unsworth, M. J., P. Bedrosian, M. Eisel, G. D. Egbert, and W. Siripunvaraporn (2000), Along strike variations in the electrical structure of the San Andreas Fault at Parkfield, California, *Geophys. Res. Lett.*, *27*, 3021–3024, doi:10.1029/2000GL011476.

van Eck, T., and A. Hofstetter (1989), Micro-earthquake activity in Dead Sea region, *Geophys. J. Int.*, *99*, 605–620, doi:10.1111/j.1365-246X.1989.tb02045.x.

Wdowinski, S., Y. Bock, G. Baer, L. Prawirodirdjo, N. Bechor, S. Naaman, R. Knafo, Y. Forrai, and Y. Melzer (2004), GPS measurements of current crustal movements along the Dead Sea Fault, *J. Geophys. Res.*, *109*, B05403, doi:10.1029/2003JB002640.

Weckmann, U., O. Ritter, A. Hoffmann-Rothe, A. Abueladas, and V. Haak (2003), The electrical image of the Dead Sea Transform on a regional scale, *Eos Trans. AGU*, *84*(46), Fall Meet. Suppl., Abstract GP11A-0251.

Wessel, P., and W. H. F. Smith (1998), New, improved version of the Generic Mapping Tool released, *Eos Trans. AGU*, *79*, 579, doi:10.1029/98EO00426.

Wiersberg, T., and J. Erzinger (2007), A helium isotope cross-section study through the San Andreas Fault at seismogenic depths, *Geochem. Geophys. Geosyst.*, *8*, Q01002, doi:10.1029/2006GC001388.

Wilson, D. S., P. A. McCrory, and R. G. Stanley (2005), Implications of volcanism in coastal California for the Neogene deformation history of western North America, *Tectonics*, *24*, TC3008, doi:10.1029/2003TC001621.

Wilson, T. (1965), A new class of faults and their bearing on continental drift, *Nature*, *207*, *4995*, 343–347, doi:10.1038/207343a0.

Zak, I. (1967), The geology of Mt. Sedom (in Hebrew with English abstract), Ph.D. thesis, Hebrew Univ., Jerusalem.

Zak, I., and R. Freund (1981), Asymmetry and basin migration in the Dead Sea Rift, *Tectonophysics*, *80*, 27–38, doi:10.1016/0040-1951(81)90140-2.

K. Abu-Ayyash, A. Abueladas, H. Al-Zubi, D. Jaser, R. Masarweh, A. Masri, I. Qabbani, and I. Rabba, Natural Resources Authority, P.O. Box 7, Amman 11118, Jordan.

A. Agnon and Z. Garfunkel, Institute of Earth Sciences, Hebrew University, Mount Scopus, Jerusalem 91905, Israel.

Z. Alasonati-Tašárová, H. J. Goetze, and S. Schmidt, Institute for Geosciences, University of Kiel, Christian-Albrechts-Platz 4, D-24118 Kiel, Germany.

A. Babeyko, K. Bauer, M. Becken, G. Bock, M. Bohnhoff, J. Bribach, P. Dulski, A. Förster, V. Haak, C. Haberland, K. H. Jäckel, C. Janssen, R. Kind, J. Mechie, N. Meqbel, A. Mohsen, P. Möller, A. Petrunin, B. Plessen, O. Ritter, R. L. Romer, T. Ryberg, J. Saul, A. Schulze, S. V. Sobolev, M. Stiller, D. Stromeyer, M. Weber, U. Weckmann, U. Wetzel, and K. Wylegalla, GeoForschungsZentrum, Telegrafenberg, D-14473 Potsdam, Germany. (mhw@gfz-potsdam.de)

Y. Bartov, National Ministry of Infrastructure, 216 Yaffo Street, P.O. Box 36148, Jerusalem 91360, Israel.

P. A. Bedrosian, U.S. Geological Survey, P.O. Box 25046, MS 150, Denver, CO 80225, USA.

Z. Ben-Avraham, Department of Geophysics and Planetary Sciences, Tel Aviv University, P.O. Box 39040, Tel Aviv 69978, Israel.

J. Ebbing, Geological Survey of Norway, N-7491 Trondheim, Norway.

R. El-Kelani, Earth Sciences and Seismic Engineering Center, An-Najah National University, P.O. Box 7, Nablus, Palestine.

H.-J. Förster, R. Oberhänsli, and F. Scherbaum, Department of Geosciences, University of Potsdam, Am Neuen Palais 10, D-14469 Potsdam, Germany.

U. Frieslander, A. Hofstetter, and M. Rybakov, Geophysical Institute of Israel, P.O. Box 182, Lod 71100, Israel.

M. Hassouneh, Ministry of Presidential Affairs, P.O. Box 4815, Abu Dhabi, United Arab Emirates.

S. Helwig and O. Koch, Institute of Geophysics and Meteorology, University of Cologne, Albertus-Magnus-Platz, D-50923 Cologne, Germany.

A. Hoffmann-Rothe, Bundesanstalt für Geowissenschaften und Rohstoffe, Geozentrum Hannover, Stilleweg 2, D-30655 Hannover, Germany.

D. Kesten, Landesamt für Geologie, Rohstoffe und Bergbau, Albertstrasse 5, D-79104 Freiburg, Germany.

M. Khatib and A. Matar, Geology Department, University of Aleppo, Aleppo, Syria.

I. Koulakov, Institute of Geology, SB, RAS, 3 Akademika Koptyuga Prosp, Novosibirsk 630090, Russia.

G. Laske, Scripps Institution of Oceanography, University of California, San Diego, 9500 Gilman Drive, La Jolla, CA 92093, USA.

N. Maercklin, Istituto Nazionale di Geofisica e Vulcanologia, Piazza Roma, 2, I-95125 Catania, Italy.

S. Oreshin, Institute of Earth Physics, B. Gruzinskaya Street, 10, Moscow 123995, Russia.

G. Rümpker, Institute of Geoscience, Goethe-Universität, Altenhöferallee 1, D-60438 Frankfurt, Germany.

K. Tarawneh, Faculty of Mining and Environment Engineering, Al-Hussein Bin Talal University, P.O. Box 358, Amman 11821, Jordan.

C. Trela, Bundesanstalt für Materialforschung und -prüfung, Unter den Eichen 87, D-12205 Berlin, Germany.